VLM optimization

Increasing efficiency through heating chamber optimization

G.J.A. Theodoulou

TU Delft

VLM optimization

Increasing efficiency through heating chamber optimization

by

G.J.A. Theodoulou

to obtain the degree of Master of Science
at the Delft University of Technology,
to be defended publicly on Thursday January 13th, 2022 at 13:00 PM.

Student number: 1507923
Project duration: February, 2020 – January 2022
Thesis committee: Prof. dr. E.K.A. Gill TU Delft, Chair of Space Systems Engineering
Ir. R. Noomen, TU Delft, Assistant Professor
Ir. B.T.C. Zandbergen, TU Delft, Thesis Supervisor

TU Delft

Preface

When I first travelled to TU Delft, to visit the open days at the age of seventeen, I did not yet know that the three-hour train delay would be a premonition for my time spend at the university. At the same time that I started studying, I also joined Delft Aerospace Rocket Engineering(DARE).

In my time at DARE I not only learned the practical side of aerospace engineering, but I also met some of my now best friends. In our projects together we did not only gain invaluable experience as engineers, but we also had a great time together in the workplace and on our launch campaigns. I want to thank all the people that crossed my path in DARE, Barry Strengholt in particular.

Halfway my studies I was convinced by Christ Akkermans, after a year-long campaign, to join Slopend. Just like DARE Slopend turned out to be a great opportunity to meet new people, who reignited my passion for sports and physical challenges. Together we also had great adventures, and on these adventure I also formed bonds with some of my now best friends. I especially want to thank Lianne de Vries, and not just for proof-reading my report.

I also want to thank the great teachers, tutors and professors at the TU Delft. It took me a long time to find joy and motivation for my studies, but this was not due to he lack of passionate and patient teachers. Most importantly, I want to thank my supervisor Barry Zandbergen for the guidance during the thesis, and for providing support to and showing interest in the projects of DARE.

I also want to thank the master students (from the master student room) for a great time, sharing ideas and keeping my long-winded train-of-thoughts on track: Aeilt-Jan, Angelos, Ares, Huib, Ilja, Julius, Kapeel, Kuldeep, and Thijs. A special thanks to Maurits and Rick for providing feedback during the midterm review.

Last but not least, I want to thank my parents, Annemiek & Costas. Despite their justified frustration with my long studies, their support never ceased. It took me a long time to figure out my life, and to start moving in the right direction. Without their patience and support it would not have been possible.

G.J.A. Theodoulou
Delft, December 2021

Abstract

In the space industry miniaturization has been a trend for decades, with satellite masses ranging from 0.1-10 kg for pico- and nano-satellites. Propulsion subsystems for these satellites have not kept up with this trend performance-wise. They are often limited by safety regulations requiring inert propellants and power budget constraints of the satellite.

Vaporizing Liquid Micro-thruster (VLM) are a type of resisto-jet considered for pico- and nano-satellites and are currently in development at Space Engineering (SE) department of the Technical University of Delft (TUD). VLM expel an electrically heated (inert) propellant, which is stored in the liquid phase.

Currently, VLM are inefficient and design tools are needed to find more optimal designs. In this research such a design tool is developed, and applied to thrusters with water as a propellant. A distinction with earlier research on VLM is that specific attention was paid to the field of micro-channel flow boiling, so that knowledge from this discipline could be applied in the heat transfer model of the VLM heating channels.

The design tool was successfully developed, and is extendible with novel heat transfer and pressure drop relations when required for future research. When applied to 1-5 mN thrust range, the outcome is that the chamber temperature can be increased without increasing the total power consumption significantly. Heating chamber design also tends to be more optimal if more and smaller channels are used than in earlier published VLM designs.

The optimal wall temperatures were about 40 K higher than the chamber temperature. The optimal channel width and wall thickness were constrained by structural limitations, at 20 and 50 micron, respectively. The optimal number of channels increased with thrust from 3-4 channels at 1 mN to 8-9 at 5 mN.

Contents

List of Figures

List of Tables

List of symbols

Symbol	Description	Units
A	Area	m^2
a	Local speed of sound	ms^{-1}
A_{chip}	Chip area	m^2
A_e	Nozzle exit area	m^2
$\frac{A_e}{A_t}$	Exit area ratio $\frac{A_e}{A_t}$	-
A_l	Area of largest channel	m^2
A_{mh}	Micro-heater area	m^2
A_p	Chamber/channel wall perimeter area	m^2
A_s	Area of smallest channel	m^2
A_t	Throat area	m^2
Bo	Bond number Bo $\equiv \frac{g(\rho_l-\rho_g)D^2}{\sigma}$	-
C_C	Contraction coefficient	-
C_d	Discharge factor $\left[C_d = \frac{A_{t_{effective}}}{A_{t_{ideal}}}\right]$	
C_{div}	Divergence loss	-
C_F	Thrust coefficient $C_F = \frac{F}{p_c A_t}$	-
C_F^0	Characteristic thrust coefficient	-
c_p	Specific heat capacity (under constant pressure)	$Jkg^{-1}K^{-1}$
C_{visc}	Viscous loss	-
d_c	Channel depth	m
D_h	Hydraulic diameter $D_h = \frac{4A}{P}$	m
$\left(\frac{dp}{dL}\right)$	Pressure drop per unit length	Pam^-1
F	Rocket thrust	N
f	Friction factor	-
F_K	Fluid constant for Kandlikar correlation (1.00 for water)	-
f_{tol}	Function tolerance (for optimization function)	-
G	Mass flux $G \equiv \frac{\dot{m}}{A}$	
g_0	Sea-level gravity ($9.81ms^{-2}$)	ms^{-2}
h	Specific enthalpy	Jkg^{-1}
h_{CBD}	Heat transfer coefficient for convective boiling	$Wm^{-2}K^{-1}$
h_{conv}	Convective heat transfer coefficient	$Wm^{-2}K^{-1}$
h_{le}	Heat transfer coefficient for entire flow as liquid	$Wm^{-2}K^{-1}$
h_{NBD}	Heat transfer coefficient for nucleate boiling	$Wm^{-2}K^{-1}$
I_{sp}	Specific Impulse	s
j	Safety factor	-
k	Thermal conductivity	$Wm^{-1}K^{-1}$
k_{si}	Thermal conducitivity of silicon chip	$Wm^{-1}K^{-1}$
l	Length of channel	m
l_c	Channel length	m
l_{chip}	Total chip length	m
$l_{convergent}$	Convergent nozzle length	m
$l_{divergent}$	Divergent nozzle length	m
l_{inlet}	Inlet manifold length	m
l_{nozzle}	Nozzle length	m
l_{outlet}	Outlet manifold length	m

Symbol	Description	Units
M	Mach number ($M \equiv \frac{u}{a}$)	-
m_0	Initial mass (of satellite/rocket)	
$\dot{m}$	Mass flow $\frac{dm}{dt}$	kgs^{-1}
M_e	Mach number ($M_e \equiv \frac{u_e}{a_e}$)	-
m_p	Propellant mass	kg
$m(t)$	Instantenous/variable rocket mass	kg
N	Amount of subdivisions in channel modelling	-
N_c	Number of parallel channels	-
Nu	Nusselt number Nu $\equiv \frac{h_{\text{conv}}\Delta x}{\kappa}$	-
P	Wetted perimeter	
p	Pressure	Pa
p_0	Total pressure	Pa
p_a	Ambient pressure	Pa
p_c	Chamber pressure (at the nozzle inlet/chamber exit)	Pa
p_e	Nozzle exit pressure	Pa
p_i	Inlet pressure (at feed system exit/chamber inlet), user1=Pa	
p_{in}	Chamber inlet pressure	Pa
P_{loss}	Power loss (all power not increasing enthalpy of propellant)	W
Pr	Prandtl number Pr $\equiv \frac{\mu/\rho}{\kappa/(c_p\rho)} = \frac{\mu c_p}{\kappa}$	-
P_{rad}	Radiative power loss	W
p_{sat}	Saturation pressure	Pa
P_t	Total power consumption	W
$P(\vec{x})$	Objective function (for optimization)	-
$P_{\Delta h}$	Power used to increase enthalpy of propellant	W
q_{cond}	Heat conduction	W
q_{conv}	Convective heat flux	Wm^{-2}
$\dot{Q}_f$	Heat transfer to propellant/fluid	W
R	Specific gas constant $\frac{R_A}{M}$	$Jkg^{-1}K^{-1}$
R	Radius	m
Re	Reynold's number Re $\equiv \frac{\rho u L}{\mu}$	-
Re_{le}	Reynold's number (entire flow considered as liquid) $\text{Re}_{le} \equiv \frac{GD}{\mu_l}$	
Re_{mod}	Modified Reynold's number $\left[\text{Re}_{\text{mod}} \equiv \text{Re}_t\sqrt{\frac{R^*}{R_t}}\right]$	
Re_t	Reynold's number at throat	-
R_t	Throat radius	m
R^*	Throat radius of curvature	m
s_c	Channel spacing(distance between parralel channels)	m
St	Stanton number St $\equiv \frac{h_{\text{conv}}}{\rho u c_p}$	-
T	Temperature	K
T_{bulk}	Bulk temperature $T_{\text{bulk}} \equiv \frac{T_{\text{in}}+T_{\text{out}}}{2}$	K
T_{bw}	Chamber/channel bottom wall temperature	K
T_c	Chamber temperature (assumed to be T_0 unless stated otherwise)	K
T_{ew}	Chamber/channel effective wall temperature	K
T_{exit}	Nozzle exit temperature	K
T_{fl}	(Average) fluid temperature	K
T_{in}	Chamber inlet temperature user1	
T_{out}	Chamber outlet temperature	K
t_{PCB}	Thickness PCB	m
T_{ref}	Reference temperature	K

Symbol	Description	Units
T_s	Surface temperature. user1	
T_{sat}	Saturation temperature	
$T_{\text{sw,eff}}$	Chamber/channel *effective* side wall temperature	K
T_{w}	Chamber/channel (top) wall temperature	K
T^*	Throat temperature at sonic throat	K
u	Velocity in x-direction (or local velocity in (quasi)-1D duct flow)	
u_e	Nozzle exit velocity	ms^{-1}
u_{eff}	Effective exit velocity	
u_s	Flow velocity in smallest pipe	ms^{-1}
v	Specific volume	$\text{m}^3\cdot\text{kg}^{-1}$
w_c	Channel width	m
w_{chip}	Total chip width	m
$w_{\text{nozzle exit}}$	Nozzle exit width	m
w_{inlet}	Inlet manifold width	m
$w_{\text{inlet,margin}}$	Inlet manifold margin	m
w_{margin}	Margin width around chip	m
w_{outlet}	Outlet manifold width	m
$w_{\text{outlet,margin}}$	Outlet manifold margin	m
w_{throat}	Throat width	m
x	Vapour quality	-
$x_{\text{dry-out}}$	Dry-out vapour quality	-
X_T	Hydrodynamic entrance length	m
α	Void fraction	-
$\alpha_{\text{convergent}}$	Half-angle at convergent inlet for 2D/3D conical nozzle	deg
$\alpha_{\text{divergent}}$	Half-angle at divergent exit for 2D/3D conical nozzle	deg
$\beta_{\text{inlet,margin}}$	Inlet manifold margin factor	-
β_{inlet}	Inlet manifold length factor	-
β_{outlet}	Inlet manifold length factor	-
$\Gamma(\gamma)$	Vandenkerckhove function $\Gamma(\gamma) = \sqrt{\gamma} = \left(\frac{2}{\gamma+1}\right)^{\left(\frac{\gamma+1}{2(\gamma-1)}\right)}$	-
γ	Specific Heat Ratio	-
ΔV	Delta V	ms^{-1}
Δh	Specific enthalpy change	Jkg^{-1}
Δl	Longitudinal resolution of simulated volumes	m
Δp	Pressure drop	Pa
Δp_{acc}	Acceleration pressure drop (across heating chamber)	Pa
Δp_{con}	Contraction pressure drop (across heating chamber)	Pa
Δp_{exp}	Expansion pressure drop (across heating chamber)	Pa
Δp_{fric}	Frictional pressure drop (across heating chamber)	Pa
Δp_{loss}	Total actual pressure loss	Pa
Δp_{total}	Total pressure drop (across heating chamber)	Pa
ΔT	Temperature increase in channel section	K
ΔV	Velocity change as provided by a thruster	ms^{-1}
ε	Emissivity	-
ζ_c	Pressure loss factor for sudden contraction	-
ζ_e	Pressure loss factor for sudden expansion	-
ζ_F	Correction factor for thrust coefficient $\left(\frac{C_{F,\text{real}}}{C_{F,\text{ideal}}}\right)$	-
$\zeta_{I_{sp}}$	Correction factor for specific impulse (motor quality) $\left(\frac{I_{\text{sp,real}}}{I_{\text{sp,ideal}}}\right)$	-
μ	Viscosity	Pas
$\mu_{I_{\text{sp}}}$	Specific impulse efficiency $\left(\frac{I_{\text{sp,real}}}{I_{\text{sp,ideal}}}\right)$	-
μ_{mh}	VLM heating efficiency	-
ρ_g	Gas density	kgm^{-3}
ρ_l	Liquid density	kgm^{-3}

Symbol	Description	Units
ρ	Density	kgm^{-3}
σ	Stefan-Boltzmann constant for black-body radiation ($5.670373 \cdot 10^{-8} WK^{-4}m^{-2}$)	$WK^{-4}m^{-2}$
σ_y	Yield strength	Pa
χ_s	Scaling factor (for optimization function)	-
$\chi_{\Delta P}$	Pressure drop 'punishment' (for objective fucntion)	-

Acronyms

AE Aerospace Engineering 9

CHF Critical Heat Flux 40

DIMES Delft Institute of Microelectronics and Submicron Technology 19

IRT Ideal Rocket Theory 11–18, 20, 22, 23, 26, 44, 45, 54, 55, 57, 61, 62, 64, 67, 69, 72, 75, 77, 81, 82, 85, 91, 92

MEMS Micro-Electro-Mechanical System 19

PCB Printed Circuit Board 51, 79

SE Space Engineering v, 4, 6, 9, 12, 14

TLR Top-Level Requirements 6, 7, 9, 10, 12, 21, 23, 56, 63, 81

TUD Technical University of Delft v, 6, 19

VHCM Vaporizing liquid micro-thruster Heating Chamber Model 92

VLM Vaporizing Liquid Micro-thruster v, xi, xiii, 2–6, 9, 11–15, 20, 22, 26, 29, 35, 37–40, 44, 46, 49–51, 54–56, 59, 61, 64, 69, 71, 75, 77–80, 82, 83, 85, 86

1 Introduction

1.1. Background: small satellites and micro-thrusters

In the space industry, miniaturization of satellites has been a trend for decades, with satellites masses ranging from 0.1-1.0 kg for **pico-satellites** and 1.0-10 kg for **nano-satellites**[1]. While the satellites became smaller and cheaper, the propulsion subsystems, that allow for ambitious missions on larger satellites, are a rare occurrence on small satellites[2].

Currently, **CubeSats** are the most common form factor for small satellites[1], with wide-spread supply of compatible components and availability of launch services[3]. Most subsystems in CubeSats have matured and commercial use is on the rise. **PocketQubes**[4] are even smaller, and this is where academia is currently pushing for further miniaturization. The Space Engineering (SE) department of the TU Delft is also researching the miniaturization of hardware for these satellite classes[5], and is actively contributing to The PocketQube Standard[4].

Thrusters are no exception to the miniaturization trend. Micro-thrusters can provide propulsion capabilities to CubeSats and PocketQubes with required thrust levels in the range of about 0.01 mN to 10 mN([6], Ch. 3) with power consumption in the range of 0.1 W tot 10 W for Micro-Electro-Mechanical Systems (**MEMS**)[7], but volume and power budget constraints indicate that the performance of these thrusters is holding back practical use[1].

With increased specific impulse I_{sp}, indicating a higher propellant efficiency[8], and lower power consumption through increased heating chamber efficiency $\mu \equiv \frac{P_{\Delta h}}{P_t}$ ($P_{\Delta h}$: enthalpy increase of fluid, P_t: total power consumption) of micro-thrusters, more ambitious missions can be performed, as the capabilities for formation flying and orbit transfers increase. In 2000 already Mueller foresaw that micro-thrusters are necessary for attitude control with sufficient precision(for cameras or other instruments)([6], Ch. 3). Last but not least, micro-thrusters can also be used to de-orbit satellites, to prevent the build-up of space debris[9].

Vaporizing Liquid Micro-thrusters (VLM) are among the type of micro-thrusters being considered for these applications. This class of micro-thruster is currently being investigated by the TU Delft[10, 11], and other academic institutions in the world[7]. VLM are essentially micro-thrusters, that use a resistive heater to heat a propellant stored in liquid phase, vaporise it, and expel the propellant in gas form through a nozzle at high velocities. This makes them a type of resisto-jet[8].

The main advantages of VLM, compared to low I_{sp} cold-gas thrusters, or toxic/energetic chemical mono- or bi-propellant thrusters[7, 12], are:

- Small, light-weight tanks due to low pressure and high density of the liquid propellant *(CubeSats struggle with volume constraints[1])*
- Allows for the use of inert and safe propellants *(regulations of energetic substances on CubeSats are strict[2])*
- Potentially higher I_{sp} than chemical thrusters if switched to hydrogen[8].

The main disadvantages are:

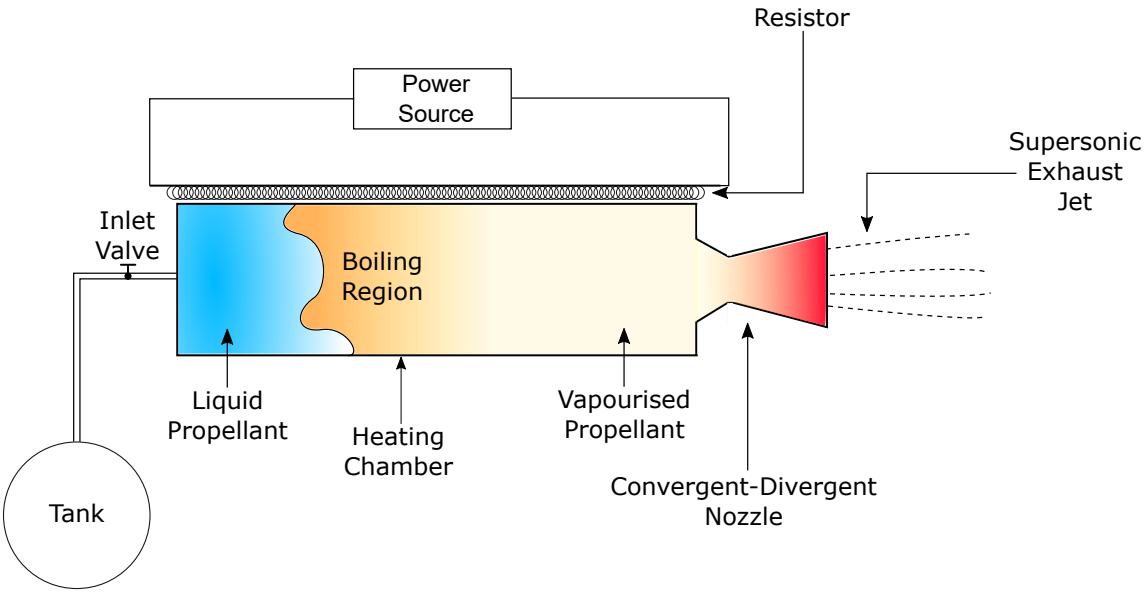

Figure 1.1: Simplified diagram of VLM under ideal operating conditions

- Inefficient use of already high electrical power consumption[7]
- Long start-up times[11, 13, 14]
- Instabilities[13]

The first problem is the main motivation behind this thesis research. Between 60-80% of the power supplied to the heating chamber is lost to the surroundings on current VLM designs[7]. The ultimate goal is to increase the applicability of micro-thrusters on small satellites, and solving this inefficiency of VLM is likely to achieve this. In remainder of this introduction, the reader will be guided through summaries what Vaporizing Liquid Micro-thruster (VLM) are in the next section, the most important performance parameters in Section 1.3, and the research design in Section 1.4. The research design section will show how this thesis is going to contribute to the solution of solving VLM inefficiencies. Finally, the structure of the entire report will be clarified in Section 1.5.

1.2. Vaporizing Liquid Micro-thrusters

VLM work by heating a non-reactive[1] propellant. The propellant is stored in liquid phase, and through resistive heating it is vapourised in a heating chamber. The vapour is then heated even further to make it more energetic, and is then accelerated through a convergent-divergent nozzle[2], so it can be expelled at supersonic speeds for maximum propellant efficiency. In essence, VLM are a type of **resisto-jet**[8]. This means that electrical power must be provided by the satellite, whereas for conventional chemical thrusters, the energy comes from the stored propellant itself.

For clarification of the operating principle, a *very* simplified diagram of a VLM is depicted in Figure 1.1. Real VLM look different, and deviate from the ideal case presented in this picture.

1.3. Performance

At a very high level, one is interested in the following characteristics of VLM:

- F: thrust
- I_{sp}: specific impulse/propellant efficiency

[1] Even though combustion is not an intended effect, chemical reactions, such as dissociation and recombination, can still take place.
[2] Also known as a “de Laval nozzle”.

- P_t: total power consumption

There are many more factors at play when considering a thruster for certain applications, such as the minimum impulse bit, total impulse, stability and start-up time. These and many other factors play a role in determining whether a thruster has any practical viability. However, to say something sensible about overall performance and efficiency of VLM, one must limit oneself to the most high-level parameters.

These high-level parameters are summarized here, and for more details on exact definitions, derivations and underlying assumptions the reader is referred to the works of Sutton[15], Anderson[16], and Zandbergen[8]. Naturally, whenever relevant import assumptions or definitions will be re-stated in this report, especially when it concerns the validity and applicability of the results.

1.3.1. Thrust

The thrust F is defined as the instantaneous mass $m(t)$ multiplied with instantaneous acceleration $\frac{dv}{dt}$. It is the sum of the momentum ejection rate of the jet coming from the nozzle $\dot{m}u_e$(mass flow times nozzle exit velocity), and the pressure force generated by the nozzle flow:

$$F \equiv m(t)\frac{dv}{dt} = \dot{m}u_e + (p_e - p_a)A_e \tag{1.1}$$

In this equation p_e is the nozzle exit pressure, and p_a is the ambient pressure, and A_e is the nozzle exit area. The pressure force $(p_e - p_a)A_e$ stated in Equation 1.1 is a simplification, because it assumes there is only a pressure differential with the atmosphere at the nozzle exit. The actual pressure thrust is the complete pressure differential caused by the thruster.

If one has a certain application in mind for a thruster, the thrust is often limited for practical reasons. If it is too high, accelerations could be too high or attitude control could become problematic due to, for example, thrust misalignment. If it is too low, manoeuvres would take too long.

In a recent review (2018), Silva et al. found that the average thrust of actual VLM is about 1 mN[17], which is in the desired thrust range of 0.01-10 mN for CubeSats and PocketQubes[6]. Improvements to specific impulse and power consumption will have less practical applications in nano-satellites or pico-satellites, if the modifications result in the thrust lying outside this desired range.

1.3.2. Specific impulse

A high specific impulse I_{sp} results in a high propellant efficiency. This means that for a given propellant mass the thrusters generate a higher total impulse, increasing the mission capabilities with these thrusters. Alternatively, one can decrease mass and volume requirements for the thruster, because less propellant needs to be stored on board.

Within a given thrust or thrust range, one ideally wants to have a specific impulse I_{sp} that is as high as possible. Specific impulse is determined with the following equation:

$$I_{sp} = \frac{u_{eff}}{g_0}, \tag{1.2}$$

$$\text{with:} \qquad u_{eff} \equiv u_e + \frac{(p_e - p_a)A_e}{\dot{m}} \tag{1.3}$$

In Equation 1.2 u_{eff} is the effective exit velocity that combines both the jet and pressure thrust term, and it is conventional to divide this velocity by sea-level gravity g_0[3].

Tsiolkovsky's Equation 1.4 of rocket motion reveals that an increase I_{sp} leads directly to a higher velocity increment ΔV for the same propellant consumption m_p, given an initial mass m_0.

$$\Delta V = I_{sp} g_0 \ln \frac{m_0}{m_0 - m_p} \tag{1.4}$$

The average specific impulse of actual produced and tested VLM is around $I_{sp} = 53$s[17].

[3]The sea-level gravity acceleration is of not of physical significance in Eq. 1.2 and 1.4. It is simply convention to divide by g_0, so that effective exit velocities can be compared in terms of a unit shared by the imperial and SI system.

1.3.3. Total power consumption

For a chemical thruster the energy is stored within the propellant, and the electrical power consumption is not used to energize the flow. However, a resisto-jet uses an electrical current to heat and/or vaporise the propellant. The total required power P_t is given by the power used to increase the propellant enthalpy $P_{\Delta h}$, and all the power lost to the environment P_{loss}(Eq. 1.5):

$$P_t \equiv P_{\Delta h} + P_{\text{loss}} \tag{1.5}$$

$$P_{\Delta h} = \dot{m}\Delta h \tag{1.6}$$

The enthalpy increase per second is given by the increase of specific enthalpy Δh of the mass flowing through the chamber $\dot{m}$. Power loss P_{loss} is in general caused by radiation to the environment and conduction through the surrounding structure. Contrary to intuition, in the ideal lossless case requiring higher I_{sp} does not necessarily increase the total power consumption. The power loss is, however, expected to increase with a higher I_{sp}.

In real applications I_{sp} and P_t require a trade-off due to power budget limitations. Actual tested VLM have an average power consumption of 3.6 W. Clearly, this puts a strain on the power budget of CubeSats and PocketQubes, which are limited in the power they produce on average (10 mW to 7W)[1]. Even though maximum power consumption can be temporarily higher to accommodate thruster power consumption, this still limits the functions that a VLM can perform. If the thrust and/or I_{sp} per Watt can be improved this unlocks more mission capabilities for CubeSats and PocketQubes. For example, a lower power consumption can make (longer) continuous thrusting possible, which in turn can allow for orbit transfers that require more energy.

1.4. Research design

In preparation of this thesis, a literature review has been conducted, and a research proposal has been developed. A short summary of the conclusions of the previous work will be given in the next section. For more detail, the reader is referred to the earlier literature study[18].

1.4.1. Conclusion of previous work

Much work has already been done on VLM, which has been summarized by Silva et al.[7]. These works were mostly practical in nature, demonstrating that VLM work, but are also inefficient. The related modelling approaches were usually either very basic or very detailed and slow. This made these models unsuitable for improving VLM heater chamber designs. Also, the related data was often too incomplete to validate models or to fully characterize the performance of VLM in a meaningful way.

Therefore, there is a need for a more advanced model, to understand and predict what heating chamber designs will improve the efficiency of VLM. Although the found data was never complete, each set of data may prove to be sufficient to validate some to almost all outputs from such a model. And, together, the data sets may cover all aspects of the model. Full validation may become possible if more data becomes available, as the work at the TU Delft continues, and other master students are doing experiments on VLM.

While no models were directly applicable, some starting points have been identified. The work of Hanselaar[19] has a useful 2D-model for modelling heat flow through heating chambers, but both his own results, as well as other results from the field of micro-channel research, suggest that a critical evaluation of the assumptions is necessary to improve the predictions. In addition, the field of micro-channel flow may provide useful models for the channel wall/fluid interface in the heating chamber, despite the fact a lot of work is not directly applicable to the flow regimes in VLM heating chambers.

It is expected that correcting the assumptions will result in a model that better predicts experimental data. The models, when properly embedded in a design tool, should therefore make it easier to step away from the trial-and-error approach that dominate the field of VLM research. In the next section, the resulting research design from the earlier developed thesis proposal, will reveal the strategy for filling this gap in literature.

The gap in literature was combined with the need of the Space Engineering (SE) department for preliminary design tools for VLM. With such tools, it will become possible to discern more viable designs, without going through the complete cycle of design, production and testing. This will reduce time and

money spent on less feasible designs, allowing researchers and students to focus on building VLM with more potential.

For the nozzle, a great start has already been made by the graduate Makhan who modelled and characterized the performance of VLM nozzles, and tested the models with cold nitrogen tests[20]. This thesis will complement this by looking at the heating chamber before the nozzle. Together, it could result in a model for overall VLM performance, which in turn may help to optimize designs before going into a costly production and testing phase.

1.4.2. Research objective

This previous work has resulted in the formulation of the following research objective:

> "To develop a practical and accurate preliminary design tool to aid in designing efficient VLM heating chambers, by establishing which combined thermal/multi-phase flow model approach accurately predicts heating chamber performance."

This objective can be unpacked into the following sub-goals:

- Establish the requirements for a practical and accurate preliminary design tool
- Establish which multi-phase flow model is correct and sufficiently accurate for preliminary design purposes
- Establish which physical phenomena play a significant role in predicting heating chamber performance
- *Auxiliary goal: Present design recommendations for the improvement of future VLM*

The last *optional* goal does not directly contribute to the research objective, but accomplishing the other goals should naturally yield insight into what makes for a better performing VLM. It makes sense to share these insights as well.

1.4.3. Research questions

To achieve these goals, the following research questions were established in the thesis proposal:

RQ0 What are the Top-Level Requirements(TLR) for the preliminary design tool?

- What are the requirements for accuracy?
- What are the requirements on practicality?
- Which VLM designs must the tool be able to deal with?
- What other requirements are vital to achieve the research objective?

RQ1 Which multi-phase heat transfer model is most suited for preliminary design purposes?

- What are the criteria for selecting the most suitable model?
- How sensitive are the outputs of the models to the inputs?

RQ2 Which assumptions are allowable for preliminary design purposes, and which must be discarded?

- What are the criteria for including/excluding assumptions?
- Which assumptions should be evaluated?
- How sensitive is the outcome to the inclusion/exlcusion of the assumptions?

RQ3 *What design recommendations can be established based on the results of the design tool?*

- *What are the characteristics of an optimal design?*
- *In what area can significant improvements in VLM performance be expected?*

The research objective paints a general picture of what the product is meant to do, but leaves room for interpretation. By answering the first research question **RQ0** the ambiguity of what *"a **practical** and **accurate preliminary** design tool"* is, can be removed. The precise definition of "practical", "accurate", and "preliminary" shall be established together with the stake-holders. In this case the stake-holders are mostly the staff and students from the SE department, as they are envisioned to use the tool in the future.

These TLR are not only pivotal when it comes to integrating the sub-goals to create one consistent design tool, but also help to establish the criteria in **RQ1-RQ2**. This approach will provide guidelines when the goals are worked on separately.

When the research proposal was established, it was expected that the model has three main "sub-models" which interface with one another:

- The multi-phase heat transfer model, concerning the heat flow from the heated wall to the fluid.
- The nozzle model, concerning the conditions that must be delivered at the end of the heated flow
- The "wall model" that determines how heat is lost from the chip, as well as the temperature profile of the channel wall.

RQ1 focuses on heat transfer model, which must be taken from literature. These models tend to be empirical and 1-dimensional in practice. The only interface with other parts of the model are at the inlet/outlet of the heating chamber, and the channel walls.

RQ2 focuses on the assumptions within the other two models, as well as other models that turn out to be necessary during the course of the research. There are many physical phenomena that could play a role in these models, and assumptions about which phenomena to include and how must be made.

Together, with the Top-Level Requirements (TLR) from **RQ0**, answering these questions **RQ1 & RQ2** should lead to the desired design tool.

The last research question ***RQ3*** focuses on the auxiliary goal. It is a broad question that captures all insights gained during the research, with the purpose of conveying these insights to future VLM researchers and designers.

1.4.4. Scope of the research

Many varieties of VLM exist, but to stay within the time limitation of the research, the scope must be limited. The choice has been made to focus on a type of VLM that is commonly produced at the SE department of the Technical University of Delft (TUD). This type of VLM is:

- produced out of silicon wafers and cut out in rectangular form,
- has a 2D-conical nozzle with constant channel depth,
- has one-sided electrical heating
- has channel geometries with a constant depth but arbitrary profile.
- has water as a propellant.

The modelling will limit itself to 1D- and/or 2D-models, and exclude 3D-models. 3D-models are usually easier to implement, as many phenomena are implemented based on fundamental equations (e.g.: conduction through the silicon in 3 dimensions). This simplicity comes with larger accuracy but also with large computational costs.

Many thousands or ten thousand iterations over the model are expected, in order to establish even a partial solution space of the performance parameters discussed in Section 1.3. This is even if just one thrust value is evaluated. Running just one 3D-simulation can however take tens of minutes to hours. This makes a 3D-model not feasible for *preliminary* design purposes.

On the other hand, 1D- and 2D-model are usually much faster, but require the introduction of assumptions. Part of the objective of this research is to determine if and how certain assumptions must be introduced, in order to strike a balance between computational speed and accuracy.

Lastly, the research limits itself to modelling steady-state flow.

1.5. Structure of the report

After this introduction the report continues with System Engineering and Software Design in Chapter 2. This chapter first focuses on establishing the TLR from research question **RQ0**. The TLR are converted into a design space, additional requirements, and the software design for the design tool.

At the heart of the design tool are many physical models, such as the heat transfer model. These models are all described in Chapter 3. In Chapter 4 the verification and validation of these models are discussed.

In Chapter 5 the design tool will be used to generate results. The combined behaviour of the model and the optimization algorithm will be investigated in three case studies, and the desired output of the model will be presented.

The research will be wrapped up with with conclusions and recommendations in Chapters 6 and 7, respectively.

2

System Engineering and Software Design

The bachelor of Aerospace Engineering (AE) and the master tracks of Space Engineering (SE) always contained a healthy blend of academia and practice. Ultimately, practical solutions to new problems are desirable, but the path towards the solution is academic in nature. A system engineering effort is required to ensure that thesis work does not stray away from its practical goal, and to prevent it from being entirely academic in nature.

In Section 2.1, Top-Level Requirements (TLR) are established, taking the needs of the stakeholders, and the mission of the SE department in consideration. These needs are already implicitly enshrined in the research objective and questions, but in this chapter these needs will be translated to explicit goals to hit. In the end, achieving the TLR should provide a benchmark for how successful the work was in furthering the mission of the department, and meeting the needs of the stakeholders.

In Section 2.2 additional (literature) research is presented, which is used as foundation for establishing the design space(Section 2.3) and software design in Section 2.4. Chapter 3 will then continue with the heating channel model that is incorporated into the design tool.

2.1. Top-Level Requirements

The TLR have been established in cooperation and in conversation with the following stakeholders:

- Supervisor (Barry Zandbergen)
- Master students working on Vaporizing Liquid Micro-thruster (VLM)
- The author

The supervisor is representing the needs of the department, and provided the assignment to develop a design tool for VLM heating chambers. Thus, he can be seen as the *customer*. The master students are major stakeholders, because they are the envisioned *users* of the tool. If the latter do not see the value in the tool, then apparently the tool is not “practical” enough, or not solving the problems these students face. Without future use of the tool, the needs of the supervisor can thus not be met.

Also, both the author and the supervisor will not be satisfied with just the tool as an end-product. The thesis must also fall in line with the academic and educational needs of the university. This thesis report is the end product that covers these academic needs, and will detail what novel approaches to VLM heating chamber modelling have been attempted, and what their success is. This academic effort cannot be seen separate from the development of the tool, as novel modelling methods must be applied and validated. This ensures that the tool provides VLM designers valuable and novel insights about how to design VLM heating chambers.

Other minor stakeholders indirectly benefit from the development of the tool and the new models. These are mostly researchers and students at other universities. The space industry as a whole could also benefit from this work, by using it to make their VLM more efficient. In that manner it will hopefully make the ambitious space missions mentioned in the introduction possible.

The full list of TLR resulting from the system engineering effort is presented in Table 2.1 on page 11. Take note that the TLR are very focused on high-level performance, and does not go into the details of the underlying heating model. Whilst the largest effort will be put into developing the underlying model, the TLR are specifically written to guide that development towards a practical goal.

Table 2.1: Top-Level Requirements for the design tool

Id.	Requirement	Rationale / clarification
TLR-01	*The design tool shall find the optimal design resulting in a minimal calculated power loss (+/- 1%) for a fixed thrust F and specific impulse I_{sp}.*	The thrust and I_{sp} should not vary as otherwise the comparison between thrusters is not valid.
TLR-02	*The design tool shall be able to provide the highest possible I_{sp} given a thrust F and a total power constraint P_t.*	It is expected that **TLR-01** is a more practical requirement to design for, as it allows optimization whilst keeping the chamber(as per Ideal Rocket Theory (IRT)) (almost) constant. But from the point-of-view from a satellite mission designer P_t, F and mass budget are given. The highest possible ΔV comes with the highest I_{sp}
TLR-03	*The design tool shall work with a thrust F range from 0.01 mN to 10 mN.*	The desired thrust for CubeSats and PocketQubes, as determined in the introduction.
TLR-04	*The design tool shall work with chamber temperatures T_c up to 1000 K.*	Arbitrary upper limit to show capabilities of VLM at temperatures higher than current lower temperatures.
TLR-05	*The calculated total power consumption P_t shall be accurate within 20%.*	Adequate for preliminary design purposes
TLR-06	*The design tool shall work with at least the following geometries: "single rectangular channel", "parallel rectangular channels", "snake channels", "metal mesh"*	Snake channels like in [11]; metal mesh like in [21]
TLR-07	*The main output shall consist of at least a complete geometric description of the design from the inlet manifold to nozzle exit, together with the top wall temperature T_w and the total power consumption P_t.*	Just the inputs and performance are not enough to know the optimal geometry. The entire design should be described for further design purposes/modelling.
TLR-08	*The auxiliary output shall be sufficient to provide insight into the characteristics of an optimal design, to establish the validity of the design tool, and to make recommendations for future VLM design.*	Knowing the chip design is not sufficient to answer all research questions. Whenever data underlying the design is necessary for research purposes, it should be added to the output.
TLR-09	*The design tool shall be compatible with nozzle models like IRT and conventional extensions of IRT using quality factors.*	IRT is the bare minimum required to established heating channel output conditions. (Emperical) quality factors are commonly used to improve on IRT in the preliminary design phase.
TLR-10	*The design tool shall be compatible with arbitrary empirical relations for heat transfer and pressure drop*	It is not certain to which flow regime the optimization will steer the channel design. New research could improve on existing relations. So flexibility is required.
TLR-11	*The design tool shall be compatible with arbitrary liquid mono-propellant*	Despite scope, design tool should be applicable to more propellants
TLR-12	*The design tool shall be open-source.*	Required for thesis research.
TLR-13	*The design tool shall provide the optimal design within 1 hour, on a 2018-issued TU laptop.*	Computational speed, as well as the computer, shall be suited for preliminary design purposes. The author-owned student laptop, available to other students, is deemed a good tool to benchmark the computational time in this setting.

2.2. Further considerations and used models

The TLR could largely be derived from the needs of the SE department and the literature study. However, for successful model development further literature research on heating channels and nozzles was required still. The research in this section was used to form and refine the following aspects in software and model development:

- The design space in Section 2.3
- Model requirements in Section 2.4
- Design tool and model design in Section 2.4.2

Since some research on one aspect often uncovered multiple more relevant findings on many phenomena in VLM, it was not doable to neatly separate the findings into the categories above. Instead, the findings of often one paper, author, or research group are summarized in one subsection below. Below each section the relevant conclusions for the points listed above are summarized.

This section is used to restate IRT equations fully, although these are expected to be well-known by the reader. A few conclusions from the earlier literature research[18] were restated here for clarity.

2.2.1. Ideal Rocket Theory (IRT)

IRT is the model that is used to calculate the required chamber conditions and to inform the design space in Section 2.3. The heating channels must deliver these conditions at the channel exit. The equations below can be found in various sources[8, 15, 16]. Nothing new is introduced in this section, but it useful for the reader to acquaint oneself with the symbols that will be extensively used throughout this report.

The symbols in the equations below are:

- F: Thrust [N]
- $\dot{m}$: Mass flow [kg·s^{-1}]
- I_{sp}: Specific impulse [s] ($g_0 = 9.80665$ [m·s^{-2}] sea-level-gravity)
- p_c: Chamber pressure [Pa] (Total/stagnation pressure at heating channel outlet/nozzle inlet)
- p_e: Exit pressure [Pa]
- A_t: Throat area [m^2]
- A_e: Nozzle exit area [m^2]
- $\frac{A_e}{A_t}$: (Exit) Area ratio [-]
- p_a: Back pressure [Pa]
- γ: Specific heat ratio (1.25-1.34 at 5 bar, depending on temperature) [-] (See Figure D.3 for values for water)
- $\Gamma(\gamma)$: Vanderkerckhove function
- R: Specific gas constant (461.52 for water) [·kg^{-1}K^{-1}]
- M_e: Nozzle exit Mach number [-]

The equations for thrust F, mass flow $\dot{m}$, specific impulse I_{sp}, effective exit velocity u_{eff} are:

$$F = \dot{m}u_e + (p_e - p_a)A_e \tag{2.1}$$

$$\dot{m} = \frac{\Gamma(\gamma)p_cA_t}{\sqrt{RT_c}} \propto \frac{1}{\sqrt{T_c}} \tag{2.2}$$

$$I_{sp} = \frac{u_{eff}}{g_0}, \tag{2.3}$$

$$\text{with:} \quad u_{eff} \equiv u_e + \frac{(p_e - p_a)A_e}{\dot{m}} \tag{2.4}$$

The Vandenkerckhove function $\Gamma(\gamma)$ is a constant based on the specific heat ratio γ. The exit velocity u_e depends on propellant properties, such as the molar mass R and γ, and on the chamber temperature T_c and exit pressure ratio $\frac{p_e}{p_c}$.

When T_c is increased, the specific impulse is expected to increase, resulting in higher propellant efficiency. The exit pressure ratio is determined by the nozzle design, specifically the exit area ratio $\frac{A_e}{A_t}$. The exit area ratio determines the Mach number at the exit M_e.

$$\Gamma(\gamma) = \sqrt{\gamma}\left[\frac{2}{\gamma+1}\right]^{\left(\frac{\gamma+1}{2(\gamma-1)}\right)} \tag{2.5}$$

$$u_e = \sqrt{2\frac{R\gamma}{\gamma-1}T_c\left[1-\left[\frac{p_e}{p_c}\right]^{\left(\frac{\gamma-1}{\gamma}\right)}\right]} \tag{2.6}$$

$$\frac{A_e}{A_t} = \frac{1}{M_e}\left[\frac{2}{\gamma+1}\left(1+\frac{\gamma-1}{2}M_e^2\right)\right]^{\frac{\gamma+1}{2(\gamma-1)}} ; \qquad M_e > 1 \tag{2.7}$$

$$\frac{p_c}{p_e} = \left[1+\frac{\gamma-1}{2}M_e^2\right]^{\frac{\gamma}{\gamma-1}} \tag{2.8}$$

$$\frac{T_c}{T_e} = 1+\frac{\gamma-1}{2}{M_e}^2 \tag{2.9}$$

The experimental performance of thrusters is often expressed in quality and correction factors. These factors relate the experimental performance to the ideal performance, as calculated by IRT.

$$C_d = \frac{\dot{m}_{\text{exp}}}{\dot{m}_{\text{ideal}}} \tag{2.10}$$

$$\zeta_{I_{sp}} = \frac{{I_{sp}}_{\text{exp}}}{{I_{sp}}_{\text{ideal}}} \tag{2.11}$$

$$\zeta_F = \frac{F_{\text{exp}}}{F_{\text{ideal}}} = \zeta_{I_{sp}} C_d \tag{2.12}$$

The discharge factor C_d relates the experimental mass flow $\dot{m}_{\text{exp}}$ to the ideal mass flow $\dot{m}_{\text{ideal}}$. Similarly, $\zeta_{I_{sp}}$ is the correction factor on the specific impulse I_{sp}, and ζ_F is the correction factor on the thrust F.

2.2.2. Condensation in the nozzle

The VLM presented in literature operate closely to the saturation curve of their propellant water. In fact, the phase of the propellant is sometimes technically unknown, due to the uncertainty of some temperature and pressure measurements. One thruster operates so closely to the saturation temperature, that the reported data actually predicts liquid water at the nozzle inlet (e.g.:$p_c = 4.8(4.7-4.9)$ bar; $T_c = 423.03(419.03-423.03)$ K for thruster # 5 in [11]). An investigation into whether a minimum chamber temperature is necessary to prevent condensation, or how much condensation would affect nozzle performance, is required.

First, the nozzle exit conditions, according to IRT, are used to predict below which chamber temperature T_c condensations occurs in the nozzle. In Equation 2.13 T_{sat} is the saturation temperature, as a function of exit pressure p_e (see Figure D.2). The result is plotted in Figure 2.1 over a large range of area ratios, with various specific heat ratios[1] γ. Even at low area ratios $\frac{A_e}{A_t}$ of 10, the minimum chamber temperature can be quite substantial already. However, the sensitivity to γ is so large, that it must be concluded that IRT is not suitable to predict condensation in the nozzle.

[1] The specific heat ratio of water is varied based on the chamber temperature, as the result is very sensitive to it. One can see that γ and T_c are inconsistent in this basic approach.

$$T_{c\,\text{min}} = \left[\frac{T_c}{T_{\text{exit}}}\right] T_{\text{sat}}(p_e); \qquad p_e = \left[\frac{p_e}{p_c}\right] p_c \tag{2.13}$$

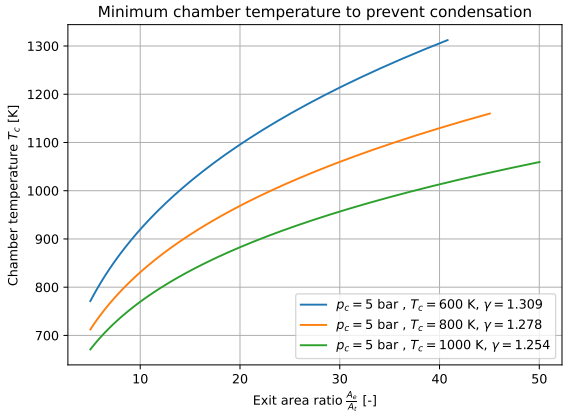

Figure 2.1: Minimum chamber temperature T_c to prevent condensation (vs. $\frac{A_e}{A_t}$)

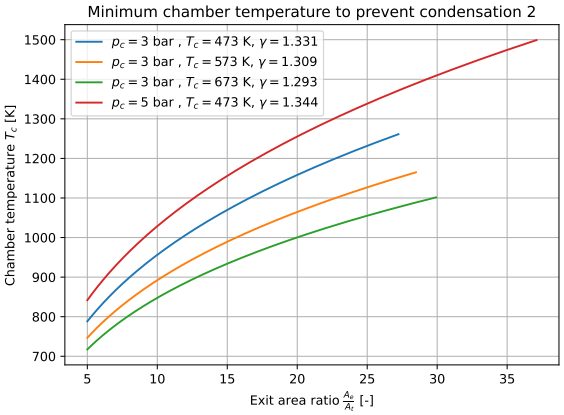

Figure 2.2: Minimum chamber temperature T_c to prevent condensation (vs. $\frac{A_e}{A_t}$) 2

To resolve this issue, a close look is taken at the work of Karagiannis, who performed his thesis on nozzle condensation at the SE department. In his work he performed a numerical study by modifying an existing solver for compressible flow to take into account real-gas behaviour and the nucleation/growth of water droplets in micro-nozzle flow.

The design parameters under his consideration were: $p_c = [1, \mathbf{3}, 5]$ bar, $T_c = [\mathbf{473}, 573, 673]$ K, $\alpha_{\text{divergent}} = [15, \mathbf{30}, 45]$ degrees. The nozzle depth was $d_c = [\mathbf{100}, 200]$ μm. The bold numbers are the baseline value. The effect of a variable was determined by varying a single parameter around the baseline. Other nozzle parameters were: half-angle of the convergent part of the nozzle $\alpha_{\text{convergent}} = 45$ deg, inlet width(also, heating channel width) $w_c = 3$ mm, a throat width of $w_{\text{throat}} = 45$ μm, back pressure of $p_a = 30$ Pa and an area ratio of $\frac{A_e}{A_t} \approx 17$. The propellant is pure water. Furthermore, the assumption is that the wall adds heat to the flow, and that their temperature is equal to T_c[22]. This is a realistic assumption, as most VLM heaters are attached to a single piece of silicon, which is highly conductive, out of which both the channels and nozzles are made.

From the baseline cases, it is immediately clear that the temperatures under consideration are much lower than those calculated in Figure 2.1. At temperatures of 473 K and 573 K only some condensation occurs, but the thrust remains equal at 1.72 mN and 1.67 mN respectively, and the I_{sp} changes slightly for 493 K from 105.90 s to 105.22 s[2], and remains 114.28 s at 573 K. At 673 K (and 3 bar), no condensation occurs already.

Compare this to what IRT and saturation curves predict at 3 bar (with γ set for the respective stagnation temperatures) in Figure 2.2. Clearly, this basic prediction is very conservative, which Karagiannis explains partly by the supersaturation phenomenon, in which the vapour can be cooled beyond the saturation temperature without condensation occurring. For the lower temperatures, it is explained that condensation has occurred (although the droplets sometimes barely consists of more than a few water molecules), but the effect is small. Consequently, this means that IRT can still be used to predict ideal nozzle performance, and further applied quality factors to it need not to deal with condensation issues, at least for area ratios below 17.

The 5 bar case is, however, of even more interest for this study. Karagiannis simulates that the degree of supersaturation is so high, that nucleation occurs through-out the flow almost instantly, creating droplets of 3-4 water molecules at most. He states that it is expected that a sudden increase in temperature and pressure should slow the process of expansion. But apparently this detrimental effect is offset by the increase of pressure thrust. Overall the thrust increases by about 1.5%. The I_{sp}

[2]The effect of condensation is determined by looking at the difference in results between single-phase and two-phase modelling.

also rises slightly, as the increased stagnation pressure results in a thinner boundary layer[22]. These findings suggest that the pressure should preferably be 5 bar.

In conclusion:

- IRT is still alllowable for calculating mass flow $\dot{m}$, I_{sp} and the thrust F (at least for area ratios $\frac{A_e}{A_t}$ below 17.)
- The $\frac{A_e}{A_t}$ is preferably below 17, and the chamber temperature T_c above 473 K.
- The pressure is preferably 5 bar instead of lower

2.2.3. Nozzle geometry

For conventional nozzles of large-scale thrusters many different nozzle geometries, such as bell nozzles, are employed to strike a balance between performance and manufacturability[15]. For micro-nozzles manufacturing limitations have restricted most practical designs to the 2D-conical[3] nozzles, and the only parameter that can be varied is the nozzle exit half-angle $\alpha_{\text{divergent}}$ for the divergent part and the inlet half-angle $\alpha_{\text{convergent}}$ for the convergent part. Additionally, the low mass flow and small dimensions result in much lower Reynold's numbers Re_t in the throat. Based on IRT, Re_t is expected to be below 2000 for low chamber temperatures ($T_c = 500$ K) and the thrusts given in the design space (Table 2.5), and below 1000 for high chamber temperatures ($T_c = 1000$ K).

Both $\alpha_{\text{divergent}}$ and Re_t can be expected to influence the efficiency of the nozzle. The used metric is usually specific impulse efficiency, describing whether the propellant consumption is really as effective as can be expected from IRT:

$$\mu_{I_{\text{sp}}} \equiv \left(\frac{I_{\text{sp,real}}}{I_{\text{sp,ideal}}} \right) \tag{2.14}$$

Louisos and Hitt have performed both 2D and 3D numerical studies of effects of $\alpha_{\text{divergent}}$ and Re_t on conical micro-nozzles. In their 2D-study they conclude that a 30 degree half-angle strikes the best balance between viscous losses and divergence losses, although it is a "weak" optimum[23]. In their 3D-study they found that the 30 degree half-angle was also optimal, for nozzle depths between 100 μm and 400 μm[24]. Karagiannis found the 30 degree angle also to be the optimum, despite using a different propellant, but only evaluated $\alpha_{\text{divergent}} = [15, 30, 45]$ degrees[22].

Louisos and Hitt also found that when 3D simulations were performed, both the nozzle depth and the throat Reynold's number Re_t played huge factors in performance. The viscous effects played a relatively large role at low nozzle depths, and increasing Re_t served to reduce this effect, by reducing the boundary layer thickness. The increase in Re_t was obtained by increasing the pressure. Again an indication that pressure must be as high as possible. The effect on performance is shown in Figure 2.3, which is reproduced from their work[23, 24].

Their work was limited to H2O2 as a propellant, but similar behaviour can be expected from water. 85% pure decomposed H202 at 886K will, according to NASA CEA, mostly consist of 60% H20, and 40% O2[4]. Since the Prandtl number and viscosity of gaseous O2 and H20 do not differ in order of magnitude, the flow can be expected to behave similar to a flow with 100% H2O. Based on Figure 2.3 it therefore seems wise to not explore nozzle depths lower than 100 μm.

In his work, Karagiannis also noted the effect of the stagnation temperature on the boundary layer thickness. Its effect is notable as heat is added to the flow through the nozzle walls (which were assumed to be equal to the stagnation temperature)[22], which is a fair assumption for VLM machined out of silicon.

In conclusion:

- Nozzle depth/channel depth d_c should not be lower than 100 micron.
- Divergent half angle of nozzle $\alpha_{\text{divergent}}$ is preferably 30 degrees.

[3] From now on, when conical nozzles are mentioned, the 2D-conical nozzle is always implied, unless stated otherwise.

[4] `https://cearun.grc.nasa.gov/cgi-bin/CEARUN/setProblemType.cgi`

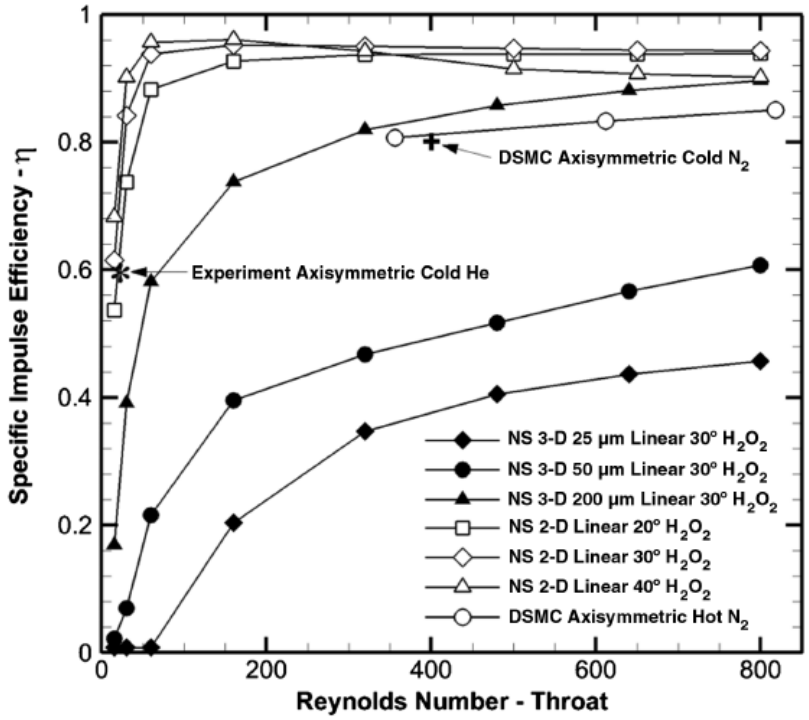

Figure 2.3: Effect of micro-nozzle depth and throat Reynold's number on specific impulse. Figure 11, reproduced from Louisos and Hitt[24]

2.2.4. Pressure drop

Whether and how a pressure drop Δp must be implemented in the model underlying the design tool is one of the most critical decisions affecting the design of the model and the software. There are roughly three options to implement:

- Constant pressure p in channel; chamber pressure p_c unaffected
- Constant pressure in channel; pressure drop Δp affects chamber pressure p_c and nozzle sizing/performance
- Pressure drop in channel, affecting heat transfer; pressure drop affects chamber pressure p_c and nozzle sizing/performance

The first option is preferred in terms of simplicity and computational speed. If the pressure drop is indeed low enough to barely affect the nozzle and the heat transfer in the channel, this would be the best option.

The second option is when the pressure drop is calculated over the entire channel, without allowing the pressure to vary in the channel itself. The pressure drop then affects the nozzle performance according to IRT (Eq. 2.2). This must be corrected for, as it would result in the inconsistencies between the mass flow in the heating channels and the nozzle. Furthermore the correction must result in the same thrust F and I_{sp}, otherwise the power loss required from **TLR-01** would be compared between thrusters with difference performances. This comparison would be meaningless.

The third option would be necessary if the effect of the pressure drop on heat transfer is significant enough to affect the power loss results. In addition to the correction required in the second option, the heat transfer model must be refined to let the thermodynamic parameters(such as density ρ) be affected by the pressure change.

Initially, the choice fell on option one, based on the expectation that the pressure drop Δp would be *at most* 0.31 bar (6.2% on a 5 bar-thruster, 0.28 bar of which was frictional). This was based on an example case that was deliberately constructed to find a a high pressure drop(see Table 2.2 based on the equations in Section 3.5).

The justification for the values in Table 2.2 below is thus that the highest *theoretically* possible mass flow has been selected, the smallest amount of channels used before in literature, with roughly the smallest diameter too, and a higher length/diameter-ratio $\frac{l_c}{D_h}$ to accommodate the increased mass flow $\dot{m}$.

This results in a frictional pressure drop of 0.28 bar (5.6%) *if the entire channel flow is assumed to be gaseous*, which it is not.There is also a pressure drop due to flow acceleration and sudden expansion.

Table 2.2: 5-channel with highest mass flow

Parameter	Value	
Inputs		
Mass flow $\dot{m}$	3.6	[mg·s^{-1}]
Chamber temperature T_c	450	[K]
Chamber pressure p	5	[bar]
Channel width w_c	100	[μm]
Channel depth d_c	100	[μm]
Channel length l_c	20	[mm]
Number of channels N_c	5	[-]
Outputs		
Gas density ρ_g	2.491	[kg·m^{-3}]
Gas velocity u_g	27.8	[ms^{-1}]
Reynolds Re	477	[-]
Friction factor f	0.1341	[-]
Frictional pressure drop Δp_f	0.28	[bar]
Accelerative pressure drop Δp_a	0.02	[bar]
Pressure drop (sudden expansion) Δp_e	0.01	[bar]
Total pressure drop Δp	0.31 (6.2%)	[bar]

However, as the model was developed and early results[5] were produced, it became clear that optimal solutions were associated with higher pressure drops than reported in literature(0.3 bar; see Section 2.2.6 on existing thrusters) or the calculated 0.31 bar. These results showed that the effect of the pressure drop on the nozzle had to be accounted for. The nozzle size had to be increased after the pressure drop, to maintain the desired specific impulse I_{sp} and thrust F. Without this **TLR-01** would be violated, as power losses between different thrusters would be compared. Naturally, the increased nozzle size increased power losses. So, preferably the inlet pressure p_{in} is as high as possible to reduce both the absolute and relative pressure drop (increased density through increased pressure, reduces kinetic energy term $\frac{1}{2}\rho u^2$ in friction losses).

The expected complication in this case was that a more complex nozzle model than IRT was no longer feasible, as changing the nozzle would alter the correction and quality factors. This would either have required another iteration in the model, which was thought to be infeasible at the time. So the choice was made to only use IRT. *See Section 3.5.4 on how the nozzle was adapted based on the pressure drop. An important note is that the back pressure p_a must be zero for the method presented in that section. This is the case as only vacuum conditions are considered (see the scope in Section 1.4.4).*

With the benefit of hindsight, this line of thought was not correct. One of the unexpected results was that despite the substantial reshaping of the nozzle, the Reynold's number in the throat Re_t was quite insensitive to changes in the nozzle (see Section 4.2.5). This means that the correction and quality factors would barely have changed either. Implementing quality and correction factors would therefore have been possible, and in fact desirable to more accurately predict the actual performance.

The third option mentioned above, was not further investigated as a great part of the model design was already committed to first option, with the possibility of switching to option two. Within the time-constraints of this research it was not feasible to investigate whether this option was necessary.

[5]See Section 5.2.3 for the final results on pressure drop confirming the early results.

Lastly, the conclusions for the model design are summarized here:

- The inlet pressure p_{in} should be as high as possible (5 bar)
- The pressure drop must be implemented, so that the nozzle can be resized to keep thrust F and specific impulse I_{sp} constant
- The back pressure p_a shall be 0.
- IRT can be extended with quality factors, despite the resized nozzle (*not implemented*)

2.2.5. Structural limitations of silicon wafers

To avoid the chip fracturing under the internal pressure of 5 bar a structural margin is required. This margin, if chosen too conservatively, will have a major impact on heat losses, as it increases the area from which heat can be radiated away.

Calculating the required margin is, however, a difficult task. First of all, silicon wafers are brittle, which means that they do not simply have one clear yield strength. Instead the yield strength is a Weibull distribution that depends amongst other things: on the dimension of the wafer, manufacturing processes leaving residual stresses, loading conditions and temperature[25].

Even if the yield strength was to be perfectly known, calculating the conditions under which pressurized rectangular open-ended channels fail, is probably best done by Finite Element Analysis. This is because stress concentrations can be expected at the corners. It is therefore infeasible to calculate a good value within the scope of this research. For future work it is recommended to closely work together with the manufacturer[6] to make the margin as small as allowable.

Instead, the found yield strength of pure silicon in Granta Edupack is taken "as is" at about $\sigma_y = 160$ MPa. Also, it assumed that the outer channel walls fail like cylindrical pressure vessel, according to the Equation below:

$$\sigma_y = j\frac{pR}{t}. \tag{2.15}$$

With a safety factor of $j = 10$, radius R of 100μm, the required thickness becomes $t \approx 3\mu$m. Intuitively, this seems too low and unrealistic, as nobody manufactures micro-channel chips with these small margins.

Therefore instead, an attempt was made to take the required margin from the existing TUD design by Silva et al. Their total chip width is 7mm(Figure 3), and from this can be deduced that the margin around the inlet manifold in Figure 9 is about 650 μm. So, probably this margin is more than enough to contain 5 bars of pressure in the inlet manifold (which is a relatively wide and long flat plate under pressure). For simplicity, it will be assumed that 500 micron will be enough for the side walls, as the side walls are in effect much narrower plates, and therefore likely to withstand more pressure.

Another sanity check on this value is to look at the top wall thickness of 200μm. The chip manufactured by Silva et al. was made out of a 300μm thick silicon wafer, out of which 100μm etched to make the chamber. The remaining 200 micron on top, then clearly is enough to contain the pressure at 5 bar in the manifold as well.

For the other diameters, micro-channel literature has been checked for the smallest produced features. For the minimum channel width w_c this is 20 micron[26]. For the minimum channel spacing s_c this is 50 micron[13]. The effect of choosing these values is investigated later in the report in Section 5.3, with a sensitivity analysis on both values.

In conclusion:

- Minimum channel widths and wall thickness values cannot be estimated with first-order equations
- The minimum channel width w_c is best to 20 micron.
- The minimum channel spacing/wall thickness s_c is best set to 50 micron.
- The structural margin around the channels/nozzle/inlet manifold is best set to 500 micron.

2.2.6. Existing thrusters

Many tests have been performed by Cen and Xu[13]. Their work deserves some extra attention as, at the time of writing, this was the only research on a functioning thruster with actual thrust measurements. For this work, only the data of the thruster which achieved full vaporization at the highest wall temperature $T_w = 573.15$ K $= 300$ °C is used.

Wherever possible, data was taken from the tables in their paper, but some had to be read from the plots[7]. Several performance plots are reproduced and collated in Figure E.1. Take note that only the

[6] Delft Institute of Microelectronics and Submicron Technology (DIMES) in the case of Technical University of Delft (TUD) Micro-Electro-Mechanical System (MEMS) micro-thrusters

[7] This was done in image-editing software with to read off coordinates with as little error as possible

line for $T_w = 300$ °C is used. The experiments were done with mass flow increments of 0.67 mg·s^{-1}. The pressure is measured at heating channel inlet, and it was averaged to filter out oscillations. In Figure E.2 the measured pressure was plotted, with a comparison to the ideal pressure according to IRT. Since the pressure was measured at the inlet, the difference is an indication of the pressure drop over the chamber. In the worst case it was 0.3 bar, and it decreases absolutely and relatively with increased mass flow rate/inlet pressure. From the reported pressure drops in VLM this was the highest one (this worst-case pressure drop was used in the argumentation concerning the effect of pressure drops in Section 2.2.4).

The relevant data for this work are tabulated below in Table 2.3(with some values taken from Figure E.2):

Table 2.3: Geometry and operating conditions of Cen and Xu's thruster design

General			**Geometry**		
Propellant	Water		Channel amount N_c	9	[-]
Wall temperature T_w	573.15	[K]	Channel/throat depth/height d_c	120	[μm]
Inlet temperature T_{in}	300	[K]	Channel width w_c	80	[μm]
Back pressure p_a	0	[bar]	Channel length l_c	6	[mm]
			Channel spacing s_c	50	[μm]
			Throat width w_{throat}	150	[μm]
			Nozzle exit width $w_{nozzle\ exit}$	1758	[μm]
			Area ratio $\frac{A_e}{A_t}$	11.72	[-]
			Divergent half-angle $\alpha_{divergent}$	15	[deg]

In addition, Cen and Xu found that an increased pressure increases stability(i.e.: less thrust fluctuations) by reducing the density ratio of the liquid and and gas phase $\frac{\rho_l}{\rho_g}$.

Other research includes the thrusters produced and tested by Silva et al.[11]. In the literature research two issues with the data and calculations were identified: the pressure and temperature measurement in the chamber implied liquid flow, yet vapour was reported (visual inspection). The other was that no thrust measurements were performed, and that VLM performance was based on IRT calculations. This was, however, erroneous as calculations showed that a shock must have occurred in the nozzle. When the work of another research group was studied, the nozzle throat was even shown to be subsonic(i.e.: not a rocket engine)[18]. Clearly, even when the focus lies on the heating chamber, it is required to pay attention that the nozzle conditions are verified.

Lastly, from the research from Silva et al.[11] and Cen and Xu[13] two thrusters are selected to determine which flow conditions can be expected. These values are necessary to select the applicable pressure drop and heat transfer relations from literature. The hydraulic diameter D_h is often used to distinguish between micro- and mini-channels[27], and the Reynold's and Prandtl number are often given to tell in which range these parameters have been established and/or validated[8]. More on the used heat transfer relations in Section 3.2. The exact values are at this stage not of interest for the actual software and model design, because the design tool will be compatible with arbitrary functions as per **TLR-10**. See Table 2.4 for the calculated flow similary parameters.

- Increased pressure reults in stability (5 bar).
- Nozzle flow must be checked for sonic throats and the absence of shocks in the nozzle.

2.2.7. Summary

The individual points made in this section are summarized below:

- The inlet pressure p_{in} should be as high as possible (5 bar)
- The channel depth d_c should not be lower than 100 micron.
- The channel width w_c should not be lower than 20 micron.
- The channel spacing/wall thickness s_c should not be lower than 50 micron.

Table 2.4: Flow conditions of existing thrusters

Parameter	Cen and Xu[13]	Silva et al.[11] #5	
Channel depth - d_c	120	100	[μm]
Channel width - w_c	80	40	[μm]
Hydraulic diameter - D_h	96	136	[μm]
Mass flow - $\dot{m}$	5.66	0.55	[mg·s^{-1}]
Inlet pressure - p_{in}	2.52	4.8	[bar]
Chamber temperature - T_c	573.15*	424.04$^+$	[K]
Number of channels - N_c	9	5	[-]
Resultant flow similarity parameters			
Mass flux - G	65	5.2	[kg·m^{-2}s^{-1}]
Reynold's number (inlet/liquid) - Re$_l$	7	1	[-]
Prandtl (inlet/liquid) - Pr$_l$	5.9	5.9	[-]
Reynold's number (outlet/gas) - Re$_g$	310	50	[-]
Prandtl (outlet/gas) - Pr$_g$	0.94	1.1	[-]

Values based on assumed room temperature inlet of $T_{\text{in}} = 300$ K;
$*$ Assumed chamber temperature equal to wall temperature;$+$ (raised by 1 degree to switch from liquid to vapour)

- The structural margin w_{margin} around the nozzle/channels/manifolds, should be 500 micron.
- Condensation in the nozzle is no concern, if the minimum chamber temperature T_c is 473K, and the area ratio $\frac{A_e}{A_t}$ below 17.
- The divergent half-angle $\alpha_{\text{divergent}}$ of the nozzle should be set to 30 degrees
- Nozzle flow must be verified to produce supersonic exhaust flow (i.e.: sonic throat, and no shocks in nozzle)

2.3. Design Space

The design space serves the following purpose in this research:

- It establishes the range of input parameters in the optimization algorithm of the design tool
- Flow similarity parameters like the Reynold's number Re can be established, which helps to identify applicable heat transfer relations and pressure drop relations.
- Determining design parameters which are necessary to know, but whose precise values are outside the scope of the research.

The TLR in Section 2.1 and the scope established in Section 1.4.4 implicitly limit the design space, the range in which viable designs can lie. Together with the points, summarized in previous Section 2.2.7, this design space can be made explicit in Table 2.5.

Table 2.5: Design space and flow similarity parameters

Parameter	Values	Rationale/source
	High-level performance	
Thrust (desired) F [mN]	$[1; 2; 3; 4; 5]$	Desirable range for nanosats, limited to 5 mN due to power constraints
Power consumption (feasible) P_t [W]	$[0 - 10]$	Feasible range for nanosats
Specific impulse (ideal) $I_{sp_{\text{ideal}}}$ [s]	$[120 - 190]$	From IRT
Propellant	Water	Scope of research
Back pressure p_a [bar]	0	VLM operate in a vacuum. Required for nozzle correction (see Section 3.5.4)
	Channel inlet & channel outlet/nozzle inlet (single channel)	
Inlet temperature T_{in} [K]	$[300]$	Room temperature
Chamber temperature T_c [K]	$[500 - 1100]$	min.: required to prevent condensation; max.: material limitations + arbitrary margin to show potential of material advancements. Higher temperatures result in higher I_{sp}
Chamber pressure p_c [bar]	$[5]$	5 bar is the material limitation. Higher stability expected with higher pressure.
Mass flow $\dot{m}$ [mg/s]	$[0.1 - 3.6]$	min.: From IRT, based on pressure, assumed channel depth and throat widths, max.: highest mass flow possible for feasible P_t
Channel depths d_c [μm]	$[100; 200; ...]$	Actual thrusters usually have 100μm depth, or multiple of this value. Severe performance loss expected below 100 μm
Channel width w_c [μm]	$[20 - 5000]$	Min.: Smallest *empty* feature found in literature [26]. Max.: arbitrary. Finite limit required for optimization. High enough to contain optimum.
Channel spacing w_c [μm]	$[50 - 500]$	Min.: Smallest *solid* feature found in literature [13]. Max.: arbitrary. Finite limit required for optimization. High enough to contain optimum.
Chip width margin w_{margin} [mm]	$[0.5]$	See Section 2.2.5
	Nozzle throat and exit (assumed $d_c = 100\mu m$)	
Exit area ratio $\frac{A_e}{A_t}$ [-]	$[5 - 17]$	Usually around $5 - 20$ for VLM, added margins for optimization purposes. Below 17 desired to prevent condensation.
Nozzle exit half-angle $\alpha_{\text{divergent}}$ [deg]	$[30]$	Several studies indicate that this angle strikes a good balance between viscous and divergent losses.
Throat area A_t [μm^2]	$[250 - 125000]$	From IRT: min.: ($F = 0.5$mN,$T_c = 2000$K,$p = 10$bar,$\frac{A_e}{A_t} = 100$); max.: ($F = 10$mN, $T_c = 450$K,$p_c = 5$bar,$\frac{A_e}{A_t} = 5$)
Throat widths w_{throat} [μm]	$[2.5 - 125]$	Follows from assumed channel depth, and throat area

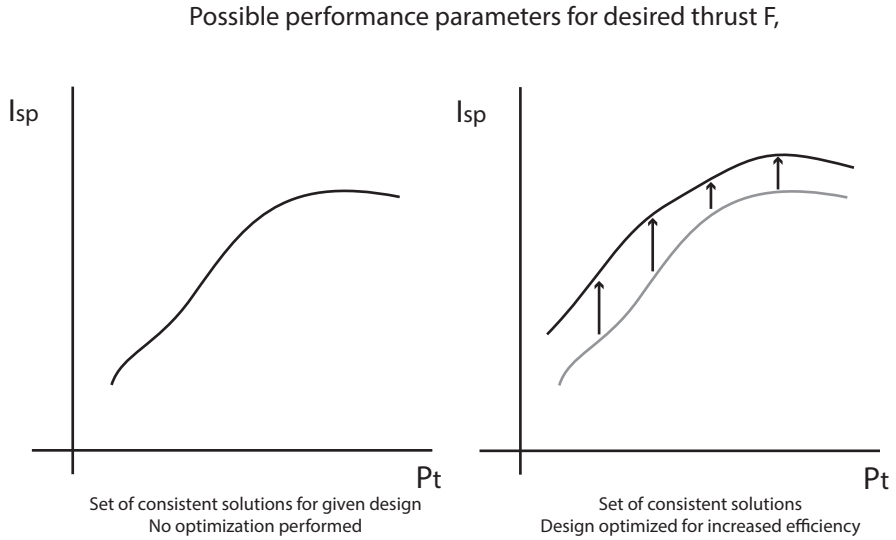

Figure 2.4: Example solution space consistent with arbitrary thrust F, without (left) and with (right) optimization

2.4. Software design

Based on the TLR and the additional research summarized in Section 2.2.7 a few further requirements on the software can be established. These requirements are given in Table 2.6.

2.4.1. Program flow

In this section, the final software design is presented schematically in Figure 2.5. The starting point is that the desired thrust is selected in the green block (top left). The blue blocks represent the design tool/optimization algorithm around the underlying heat transfer model. This part of the code iterates over the range of chamber temperatures to find optimal solutions and power consumptions for a range of specific impulses.

The optimization algorithm within this blue block code runs the underlying model (yellow blocks) multiple times, each time varying the input. This type of design satisfies **TLR-01** to **TLR-04** (optimization purpose, range of thrusts and temperatures), The desired accuracy(**TLR-05**) within these desired ranges must of course be validated (see Chapter 4).

To clarify the end result, the output is envisioned to look like Figure 2.4. The plot will consist of a line on which each point is an optimal solution. The right side of the Figure visually represents the goal of this thesis, and how this will met by the design tool. The optimization algorithm raises the I_{sp} that can be obtained at a given total power consumption P_t, by finding the design parameters that minimize power losses/increase efficiency.

The nozzle model requirement **TLR-09** is only partially satisfied, as it has been implemented only with basic IRT. One result of this research is that this requirement could have been fully satisfied due to the near-invariance of the throat Reynold's number Re_t after nozzle corrections in the model.

The orange blocks are the overall model tool and design settings. In Fixed Design Parameters values such as the chosen propellant(water) reside, as well as fixed values like the divergent half angle $\alpha_{\text{divergent}}$ of the nozzle. The Nusselt and pressure drop relations block contain code that can be interchanged, and take arbitrary arguments from the model in the yellow block (satisfying **TLR-10**).

The last red output block and the two blocks before it, make sure that the optimal geometry and performance are outputted as per **TLR-07**. Sufficient auxiliary data is stored (**TLR-08**) to analyse the results as has been done in Chapter 5.

2.4.2. Design tool

The next chapter will go into the depth of the model, but the model on its own is not useful. It needs to be part of a design tool, whose purpose it is to find the optimal design given some high-level design parameters and constraints. In short: the model takes 4 variables, and returns a total power consumption

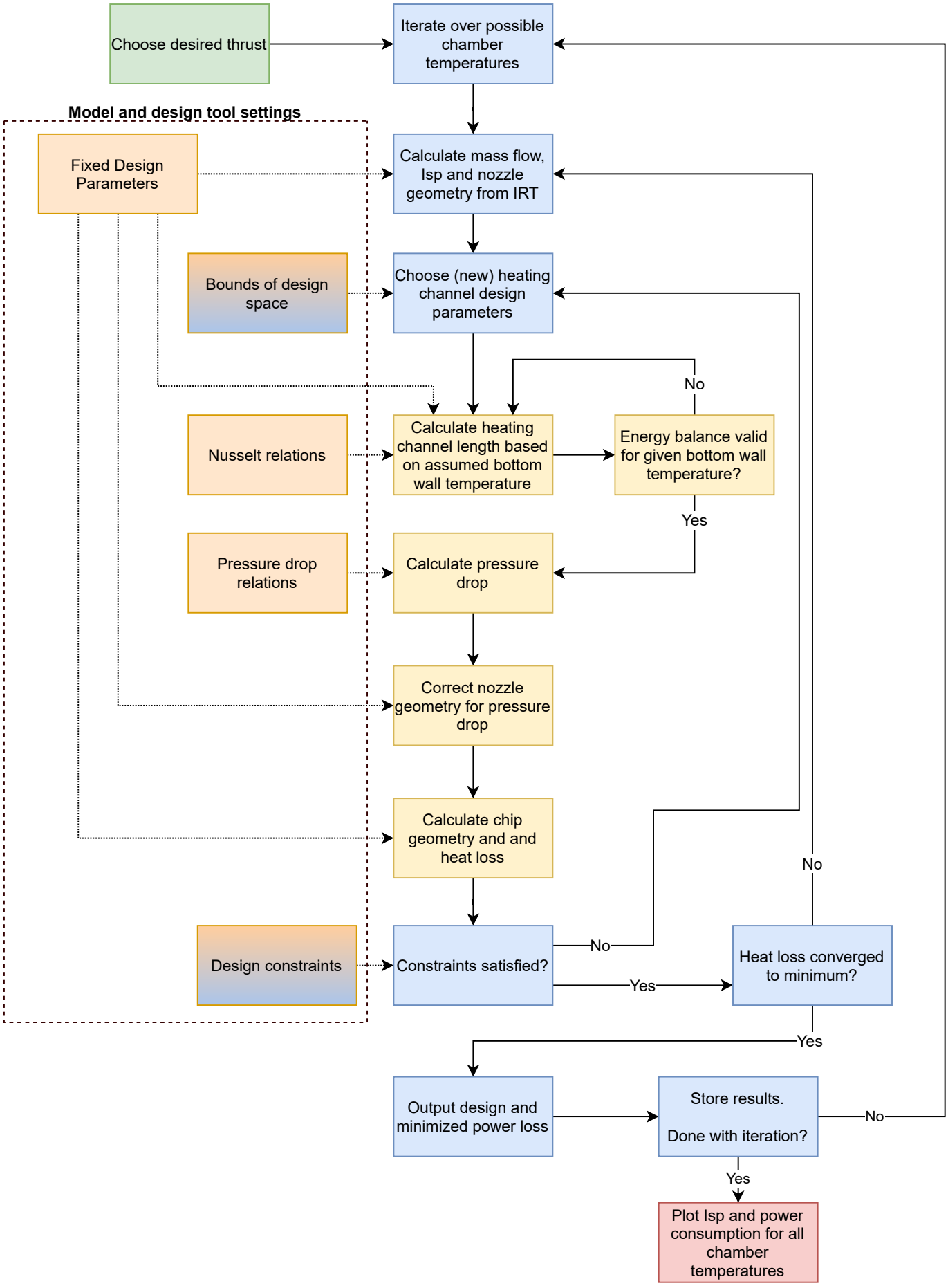

Figure 2.5: Program flow of model underlying design tool

P_t, consistent with the predetermined performance requirements (F & I_{sp}). The four variables are:

- Number of channels - N_c
- Channel width - w_c
- Channel spacing - s_c
- Top wall temperature - T_{w}

The job of the design tool is to determine the highest I_{sp} that can be achieved given a total power consumption constraint P_t. This is accomplished by iterating of a range of chamber temperatures T_c. Each iteration the design is optimized to minimize the power consumption. This results in the required I_{sp} vs. P_t plot, as envisioned in Figure 2.4. Each point on the plot has an associated set of design parameters $(N_c, w_c, s_c, T_{\text{w}})$. The next section will explain how these parameters are determined.

Table 2.6: Additional software and model requirements

Id.	Requirement	Rationale / clarification
REQ-01	*The mass flow $\dot{m}$ between the heating chamber model and the nozzle model shall be consistent within 0.01%*	The resulting overall design must be physically possible.
REQ-02	*The heating channel model shall output the chamber temperature T_c*	Required for IRT
REQ-03	*The heating channel model shall output the chamber pressure p_c*	Required for nozzle correction/IRT
REQ-04	*Radiation and conduction losses shall be incorporated in the heat loss model*	VLM operates in vacuum, back pressure by necessity 0.
REQ-05	*The flow shall be fully vapourised at the end of the channel*	Earlier research produced ambiguous chamber conditions.
REQ-06	*Resultant chamber conditions shall be verified to produce a supersonic exhaust velocity*	Earlier thrusters were determined to not have properly functioning nozzles.
REQ-07	*The effect of channel spacing shall on heat transfer shall be incorporated in the model*	Without this, the channel spacing cannot effect the optimal outcome except by simply making the chip smaller. (see Section 3.4.5)

2.4.3. Optimization Algorithm

For the purpose of this research, it is best to use an already implemented algorithm that suits the job. The entire model was programmed with the open-source Python programming language, and the NumPy package. SciPy is a package that builds upon on NumPy and provides many additional tools for scientific computing. It is specifically designed to work with NumPy. From this package the default algorithm for multivariate, bounded optimization was chosen. This is the 'L-BFGS-B' algorithm, which is short for "Limited Memory Broyden–Fletcher–Goldfarb–Shanno (Bounded)". The SciPy documentation is found here: `https://docs.scipy.org/doc/scipy/reference/optimize.minimize-lbfgsb.html`.

The details of the algorithm are not of specific interest for this research, but a short description is given. 'L-BFGS-B' is a variant of the multivariate Newton's method for minimization, with reduced computational complexity. It is thus a gradient descent method for continuous functions. The details are complex, but can be found in the original work of Byrd et al.[28]. The main result of the work was used as-is with the intention to carefully validate if the algorithm is robust and reliably finds the correct optimum. This validation is in Section 4.2.6.

Most optimization algorithms do not work "out-of-the-box" and have various settings that can be altered to make it work. This is simply a process of trial-and-error, in which one tries to understand why the algorithm fails, or terminates prematurely.

The algorithm does not work with discrete values. It can thus not handle the number of channels N_c as a variable. This is solved by simply splitting the optimization in multiple optimization efforts, one for each integer N_c in the design space. Each N_c is thus associated with a separate power loss and design. From all designs, the one with the lowest power loss is selected.

This means that the 'L-BFGS-B' really only acts on the variables (w_c, s_c, T_w). Turning these variables into a power loss is not trivial, as there are solutions violating constraints within the design space. The algorithm has no way of dealing with this, as the power loss function returns 'nan'[8]. This only happens when the calculated pressure drop Δp(Section 3.5) is lower than the inlet pressure p_{in}. This is possible because the pressure is assumed to be constant in the heating channels, and only calculated afterwards.

A conventional way to deal with such an issue is to introduce an objective function $P(\vec{x})$, which is equal to the total power consumption P_t, when the solution is valid, but numerically 'punishes' the algorithm by returning a much higher value when the solution is invalid. The punishment can, however, not simply be a high constant, as the gradient around invalid solutions would be zero. This would cause the algorithm to terminate, as it assumes it has found an optimum. The introduced objective function preferably has a gradient that points back towards correct designs, but also has a value that is high enough to be definitely higher than correct designs.

This is achieved by introducing a "pressure drop punishment" $\chi_{\Delta P}$, that increases as the calculated pressure drop goes beyond p_{in}. The arbitrary factor of 2 in the 'punishing' objective function makes sure that the returned value is always higher than the valid solution. After all, the optimized power consumption likely satisfies this inequality: $P_{\Delta h} + P_{loss} \leq 2P_{\Delta h}$.

$$P(\vec{x}) = \begin{cases} (P_{\Delta h} + P_{loss})\chi_s & \text{(if: } \Delta p \leq p_{in}) \\ 2P_{\Delta h}\chi_s(1 + \chi_{\Delta P}) & \text{(if: } \Delta p \geq p_{in}) \end{cases} \tag{2.16}$$

$$\chi_{\Delta P} = \Delta p - p_{in} \tag{2.17}$$

A function scaling factor χ_s is also introduced in Equation 2.16. The purpose of this factor is artificially increase the gradient of the objective function. One of the termination criteria for the 'L-BFGS-B' algorithm is a small gradient, as further changes to the parameters would then hardly improve the calculated power loss. This criterion is necessary, as there must be a point to decide to stop optimizing.

The default gradient setting for termination, however, causes an issue with subsequent optimization runs for the different channel numbers N_c. It causes the difference between solutions of different channel numbers to be less gradual and smooth. Whilst the impact on the power loss is small between iterations, it makes analysis of the results difficult. The scaling was increased to $\chi_s = 1 \cdot 10^{10}$ to resolve this type of premature termination.

[8] 'not a number'

Two other settings also had to be altered to make the optimization algorithm robust. Without changes the algorithm would get stuck in 'false' optima and terminate prematurely. One setting is the refinement of the temperature mesh used in the model simulation, i.e.: the number of subdivisions N of the channel temperature ranges for each phase(see Section 3.1.1: Eq. 3.2). Insufficient resolution results in less accuracy and discontinuous behaviour of the model. These inaccurate results cause small fluctuations on the objective function, creating many apparent optima. The resolution of the model had to be increased beyond the point of desired accuracy to resolve this problem. It, however, worked best when the 'function tolerance' f_{tol} of the algorithm was decreased in conjunction. The function tolerance is the setting for another termination criterion: the optimization terminates if the relative improvement of the objective function falls below the tolerance. This type of premature termination was eliminated by setting $N_l = N_{tp} = N_g = 1000$, and the function tolerance[9] $f_{\text{tol}} = 2.220446049250313 \cdot 10^{-20}$.

The last remaining setting is the initial guess $(w_{c0}, s_{c0}, T_{\text{w}0})$ put into the algorithm. A good initial guess mostly helps to speed up the algorithm, as it meets the termination conditions earlier. The initial guess for each optimization run with channel count $N_c = i$, was set the solution found for $N_c = i-1$. For the first optimization run with $N_c = 1$ the initial guess is the upper bound of each of the three variables (see Table 2.5).

All optimization settings are summarized in Table 2.7 below. Whether these settings result in the correct global optimum, is validated in Section 4.2.6.

Table 2.7: Optimization setting of 'L-BFGS-B' and 1D-model

Setting	Value
Scaling factor - χ_s	$1 \cdot 10^{10}$
Subdivisions of temperature mesh - N	1000
Function tolerance - f_{tol}	$2.220446049250313 \cdot 10^{-20}$

[9] The relatively arbitrary value comes from the default setting, which is $2.220446049250313 \cdot 10^{-9}$

3

Modelling micro-channel flow

In Chapter 2 requirements were set for what the model at the heart of the optimization must accomplish to become a valuable design tool for Vaporizing Liquid Micro-thruster (VLM) heating chambers. To briefly recap: for a desired thrust F and specific impulse/mass flow combination $(I_{sp}, \dot{m})$ the model must help the designer to find the lowest possible power consumption P_t.

This chapter mainly deals with the yellow blocks in Figure 2.5, which described the program flow of the design tool. Section 3.1 deals with the first block, where the overall channel length is calculated. This is done based on bottom wall temperature, which must be iterated towards. This is explained in Section 3.4.5.

This first block of code, also requires Nusselt relations for the three subsequent phases in the channel (liquid, two-phase, and gaseous phase). These are all discussed in Section 3.2 to 3.4.

After the channel length is established, the required pressure drop calculations are explained in Section 3.5. Based on the pressure drop, the nozzle correction is applied, after which the full chip geometry can be calculated in Section 3.6. When the full geometry and the top and bottom wall temperatures are known, the heat losses can be calculated. This is described in Section 3.7.

When the heat loss P_{loss} is known, the total power consumption P_t can be calculated, with the ideal power consumption $P_{\Delta h}$ (Eq.: 1.6). Keep in mind that this power consumption is not the minimum power consumption as required by **TLR-01**. Instead, the design tool and optimization algorithm, as described in Section 2.4.2 and 2.4.3, do use the output to iterate towards the desired minimum. These minima are presented in Chapter 5 on Results.

3.1. Fundamental 1D-channel model

An entire model for VLM heating chambers consists not only of partial mesh generation, thermodynamic properties, and modelling of two-phase flow properties. Still, those aspects of the model will be treated as the “fundamental model”, as numerically and code-wise they are separated neatly from implemented empirical relations such as heat transfer and pressure drop models(**TLR-10**). A single exception was made for the two-phase flow properties, which must rely on modelled assumptions about flow behaviour.

A heating chamber often has multiple channels, and the assumption is made that the flow through these channels is **steady** and **completely similar**. The change of flow properties, and heat transfer to the flow is modelled for just a single channel, which has a mass flow that is $\frac{1}{N_c}$ of the required total mass flow. A single channel calculation happens in two steps, and is repeated three times in roughly the same fashion for the three phases:

- Fully liquid flow *(Vapour quality: $x = 0$; Temperature: $T_{in} < T < T_{sat}$)*
- Two-phase flow *(Vapour quality: $0 < x < 1$; Temperature: $T = T_{sat}$)*
- Fully gaseous flow *(Vapour quality: $x = 1$; Temperature: $T_{sat} < T < T_c$)*

The above steps are not interdependent. The model ensures that their boundaries seamlessly join together at the saturation temperature T_{sat}. During post-processing, the three separate flow calculations

can simply be combined into full channel flow of the three consecutive sections. This is simply done by joining the values together[1].

The final result is the channel length l_c, given in Equation 3.1. In this equation the l_N refers to the last element of the cumulative channel length equations of the respective phases in Equation 3.5.

$$l_c = l_{N_\mathrm{l}} + l_{N_\mathrm{tp}} + l_{N_\mathrm{g}} \tag{3.1}$$

The fully liquid and gaseous phase are numerically the same, but with differing boundary conditions, flow properties, and attached heat transfer relations. They only differ in the enforced boundary conditions and the attached Nusselt Nu relation. Both the models are therefore referred to as "**fundamental single-phase model**", and go through the following procedure:

A *Once per full optimization run:* generate a mesh with **temperature steps** ΔT. **"Pre-calculate"** all *channel-geometry-independent* thermodynamic and flow similarity parameters properties in each section. (see Section 3.1.1 on the use of ΔT.)

B Calculate required length $l_{N_\mathrm{l}}/l_{N_\mathrm{g}}$ for liquid/gas section:

- *B1* - Use channel geometry to calculate remaining flow similarity parameters (such as Re from D_h)
- *B2* - Pass all required parameters to *arbitrary* attached Nusselt relation[2]
- *B3* - Use the resulting Nusselt number to determine the channel section length Δl

The procedure is very similar in the **fundamental two-phase flow model**. This part has as major difference that instead of temperature, the vapour quality x varies. Also the assumed homogeneous two-phase flow regime about must be imposed, to determine the void fraction α. More details on this in Section 3.1.2:

A *Once per full optimization run:* generate a mesh with **vapour quality steps** Δx, and **"Pre-calculate"** all *channel-geometry-independent* properties in each section.

- *A1* - Calculate void fraction α, to determine mixture density ρ.
- *A2* - Calculate all well-defined mixture thermodynamic properties and flow similarity parameters
- *A3* - Calculate saturated liquid and gas properties
- *A4* - Calculate "mean" two-phase thermodynamic properties and flow similarity parameters for ill-defined but necessary values

B Calculate required length l_{N_tp} for two-phase section:

- *B1* - Use channel geometry to calculate remaining flow similarity parameters (such as Re from D_h)
- *B2* - Pass all required parameters to *arbitrary* attached Nusselt relation[3]
- *B3* - Use the resulting Nusselt number to determine the channel section length Δl

Step **A1** is where the homogeneous flow assumption is imposed, which determines mixture density, separate gas and liquid velocities. Step **A2** determines values such as enthalpy of the two-phase flow, which is a clear function of how much fluid already has evaporated. Step **A3** calculates saturation values, separately, as they are often used as reference for two-phase Nusselt relations. In step **A4** an assumption is made about how certain properties like viscosity μ and thermal conductivity k change between the saturation properties. Technically, these properties do not make sense as two-phase

[1] And ensuring the cumulative length takes the previous section length into account.

[2] The fundamental model has no knowledge of which parameters are required, and simply passes all parameters required by any of the Nusselt relations considered in this thesis. For future work it is trivial to extend the code to pass even more parameters, and make use of new relations found in literature. Instructions are in Chapter A

[3] The fundamental model has no knowledge of which parameters are required, and simply passes all parameters required by any of the Nusselt relations considered in this thesis. For future work it is trivial to extend the code to pass even more parameters, and make use of new relations found in literature. Instructions are in Chapter A

flow parameters, and there are multiple way to calculate them[29]. However, in some cases Nusselt relations rely on those values.

Steps **A** and **B** are described in Section 3.1.1 for both the liquid and gas phase, and in Section 3.1.2 for two-phase flow. Step **B2** is described in Section 3.2. After these steps are performed for each phase, the results can be used to determine the total power consumption of the thruster in step **C**.

C Calculate total power consumption P_t

- **C1** Calculate pressure drop Δp with any arbitrarily provided function.
- **C2** Adjust throat width w_{throat} to maintain desired nozzle performance (F, I_{sp}, $\dot{m}$)
- **C3** Calculate final chip geometry
- **C4** Calculate heat loss

D Check constraints and validity of solutions

E Post-process results

In step **C1** the pressure drop is calculated to the required nozzle correction in step **C2** (**REQ-01;REQ-03**). With the nozzle geometry known, the entire chip geometry can be determined in step **C3**. After this the heat losses P_{loss} can be calculated in step **C4**. Together with the ideal power consumption $P_{\Delta h}$, this results in the total power consumption P_t.

In step **D** the nozzle flow is checked as required by **REQ-06**(no shocks in nozzle and supersonic exhaust velocity). In addition, the Mach number M at the channel exit was checked to see if no impossible solutions were generated, such as (super)sonic channel flow. In the end this constraint check was ignored by the optimization algorithm, as the actual optimal results always were well within the posed constraints.

Step **E** takes the results and presents the optimal geometry together with the minimized power loss to satisfy **TLR-07**. Additional data is stored, as required by **TLR-08**, so that the behaviour of the model and optimization algorithm can be investigated in the results.

In the next section an explanation will be given as to why temperature steps were chosen, and the complete mathematics will be laid out for the single-phase flow. It is followed by a similar section for the two-phase flow.

3.1.1. Single-phase model

When modelling physical problems, it is tempting to immediately jump to dividing the mesh into control volumes of the same dimensions. It is often the simplest and the best solution, because other ways of parametrizing the domain should yield the same results in the limit. However, the benefits of choosing a different parameter could be: more physical insight due to a more intuitive mathematical representation, or reduced computational complexity/increased computation speed. Since this thesis contains an optimization effort, reducing computation speed will be really helpful in the long run.

While it is often unwise to prematurely optimize a program, using ΔT steps instead of Δl(length of a subdivided channel section) to subdivide the mesh is rather trivial and comes with the following immediate benefits:

- Many thermodynamic state variables remain unchanged even if the geometry or flow velocity changes, and need to be calculated just once.
- The accuracy of the solution is higher for the same amount of channel subdivisions N, as the accuracy of calculated channel length/temperature change depends on the accuracy of thermodynamic parameters. These parameters vary with T, so making small ΔT steps keeps them accurate over the smal channel section length Δl associated with this temperature step ΔT.
- The velocity u in the channel section mostly changes with the density ρ. Heat transfer greatly depends on this velocity. Again, the temperature-step approach makes sure that the velocity does not change suddenly over the temperature step. This increases accuracy even if the same amount of subdivisions N are used.

- By fixing the temperatures, they can be set equal to the saturation temperatures in precisely known positions. The saturation state is usually ambiguous, unless the program is told whether it is gaseous/liquid or in between. This approach allows for removing this ambiguity in a very simple way, reducing errors.
- The total length of the NumPy arrays storing the (intermediate) results is fixed, and know a-priori. Keeping array sizes fixed through calculation prevents the computational cost of changing the array sizes, which is quite large. This penalty could be reduced but not eliminated, and this would require additional code complexity. This complexity is avoided.
- It is easier to implement in the program[4]

To best way to demonstrate the points above, is to simply lay out the mathematics of the model. The mathematical description of this approach is as given below.

The input is an array of monotonically increasing temperature, given in Equation 3.3, which can be used to compute the array of length steps in Equation 3.4. And the desired output of the position l_{N-1} at which temperature T_{N-1} occurs is computed by cumulatively summing all terms of the length-step array with Equation 3.5.

$$n = 0 \quad \dots \quad N-1 \tag{3.2}$$

$$T_{0\to N-1} = [T_0 \quad T_1 \quad \dots \quad T_{N-2} \quad T_{N-1}]; \qquad \text{with: } \Delta T = T_i - T_{i-1} = \text{const.} \tag{3.3}$$

$$\Delta l_{0\to N-1} = [0 \quad \Delta l_1 \quad \dots \quad \Delta l_{N-2} \quad \Delta l_{N-1}]; \tag{3.4}$$

$$l_{0\to N-1} = [l_0 \quad l_1 \quad \dots \quad l_{N-2} \quad l_{N-1}]; \qquad \text{with: } l_i = \sum_0^n \Delta l_i \tag{3.5}$$

All Δl_i in Equation 3.4 for $\Delta l_{1\to N-1}$ must thus be found to obtain the result, which is done in roughly three overall steps:

1. Use the temperature and pressure to determine the remaining thermodynamic state at each section in n, and non-geometric dependent flow parameters (such as: density ρ & Prandtl number Pr).
2. Use the geometry of the channel (area A & wetted perimeter P) to solve geometry-dependent parameters (such as: velocity u & the Reynold's number Re).
3. Calculate the Nusselt number Nu, and the required length Δl to raise the enthalpy/deliver power required to achieve a temperature increase of ΔT.

It is the first step of this list where the main benefit is obtained, as it needs to be done only once, regardless of geometry. For these calculations the following variables are also known: mass flow $\dot{m}$, pressure p, which is assumed to be equal to the inlet pressure p_i. The first temperature T_0 or the last temperature T_{N-1} is set equal to the saturation temperature T_{sat}, for respectively the start of the gas phase, or the end of the liquid phase. Then, the correct phase is forced on each first/last element of the array. E.g.: if the temperatures ranges through the gas phase ρ_0 is forced to be the gas density at the saturation point: $\rho_{g_{\text{sat}}}$.

Of course, $T_0 = T_{\text{in}}$ for the liquid section of the channel, and $T_{N-1} = T_c$ is the chamber temperature of the thruster, as that is the desired outlet temperature. These elements in the array require no special attention. In addition, the mass flow $\dot{m}$, which aids in calculating the required heating power $P_{\Delta h}$ per channel section, regardless of geometry.

This entire first step **A** shall be referred to as the "**pre-calculation**" step, and the thermodynamic state variables in Equations 3.6 to 3.10 are determined. This step is the main reason why temperature steps are chosen, as they require solving complex/large equations (sometimes iteratively). These calculations are relegated to the CoolProp library[30]. With length-steps, the temperature would constantly

[4] This is, of course, subjective, but also a simple consequence from the fact that many things need to be calculated just once with this approach. One simply has to go through all parameters that can be pre-calculated if they are geometry- and velocity-*independent*. No additional care is needed to make this approach work.

change in each channel section, and this would have to be done again *every* time a new geometry is considered for optimization.

$$\rho_{0\to N-1} = [\ \rho_0\ \ \rho_1\ \ \dots\ \ \rho_{N-2}\ \ \rho_{N-1}\ ] \tag{3.6}$$
$$h_{0\to N-1} = [\ h_0\ \ h_1\ \ \dots\ \ h_{N-2}\ \ h_{N-1}\ ] \tag{3.7}$$
$$c_{p_{0\to N-1}} = [\ c_{p_0}\ \ c_{p_1}\ \ \dots\ \ c_{p_{N-2}}\ \ c_{p_{N-1}}\ ] \tag{3.8}$$
$$k_{0\to N-1} = [\ k_0\ \ k_1\ \ \dots\ \ k_{N-2}\ \ k_{N-1}\ ] \tag{3.9}$$
$$\mu_{0\to N-1} = [\ \mu_0\ \ \mu_1\ \ \dots\ \ \mu_{N-2}\ \ \mu_{N-1}\ ] \tag{3.10}$$

In this list ρ is the density, h is the specific enthalpy, c_p is the specific heat at constant pressure, k is the thermal conductivity, and μ is the viscosity. From these values, some other variables can be pre-calculated, with the following equations[5]:

$$\dot{Q}_{\Delta h,0\to N-1} = \dot{m} \cdot [0 \quad (h_{1\to N-1} - h_{0\to N-2}) \quad] \tag{3.11}$$
$$\mathrm{Pr}_i = \frac{c_{p_i}\mu_i}{k_i} \tag{3.12}$$

In Equation 3.11 the required power to raise the enthalpy in each channel section, is calculated by multiplying it with the mass flow $\dot{m}$ with $\Delta h = h_i - h_{i-1}$. The first element is set to 0, as it is already at the defined enthalpy at the inlet (although it is arbitrary whether this 0 is added to the front or back of the array, as long as one is consistent). The Prandtl number Pr can also be calculated already.

This concludes the pre-calculation phase, and now one can move on to second next step: the **geometry-dependent** phase **B**. For this, only the channel area A, and the wetted perimeter P need to be introduced. This means the hydraulic diameter D_h is also known at this point.

$$u_i = \frac{\dot{m}}{\rho_i A} \tag{3.13}$$
$$\mathrm{Re}_i = \frac{\dot{m} D_h}{A\mu_i} \tag{3.14}$$
$$\mathrm{Nu}_i = f(\mathrm{Re}_i, \mathrm{Pr}_i, \dots) \tag{3.15}$$
$$h_{\mathrm{conv}\,i} = \frac{\mathrm{Nu}_i k_i}{D_h} \tag{3.16}$$
$$A_{\mathrm{p}_i} = \frac{\dot{Q}_i}{h_{\mathrm{conv}\,i}(T_\mathrm{w} - T_{\mathrm{ref}\,i})} \tag{3.17}$$
$$\Delta l_i = \frac{A_{\mathrm{p}_i}}{P} \tag{3.18}$$

In Equation 3.13 the velocity u is calculated, taking into account the changing density ρ. With the hydraulic diameter D_h known (computed with Eq. 3.40), the Reynold's number Re can be determined in Equation 3.14, also taking into account how viscosity μ changes with temperature. The Reynold's number is calculated because for the calculation of the Nusselt number Nu in Equation 3.15 it is often required, just like the Prandtl number Pr. The Nusselt number relation is purposefully left blank here, as many relations can be applied, and many more parameter can play a role in calculating it.

In Equation 3.16 to 3.18 the heat transfer coefficient h_{conv} is calculated. The perimeter area A_p around the channel is then set to precisely delivered power $\dot{Q}$. T_w is then equal to the top wall temperature or replaced by the effective wall temperature T_{ew} (see Section 3.4.5). The reference temperature T_{ref} is the temperature of the fluid at that point in the channel (Equation 3.3).

With the wetted perimeter P this results in the required section length Δl. These last equations are really the only mathematical change to the model in the temperature-step approach. Normally one would solve for the temperature T, which really is just a small rearrangement of the terms. It is, however, this small rearrangement that results in all the major benefits listed above.

[5] At this point the subscript i will be used instead of $0 \to N-1$ for improved readability, unless some index manipulation is required for a calculation, such as in Eq. 3.11

3.1.2. Two-phase model

For the saturation phase, the same process is repeated. However, instead of temperature the vapour quality x is the varied parameter. The benefits are almost the same as for the single-phase calculations. The start and end of the boiling phase of the model precisely coincides with the point of a fully saturated liquid or gas, respectively.

The major difference with the single-phase calculations is that some assumptions about flow behaviour must be imposed to solve the heat transfer equation. These assumptions often dictate the relative speeds of the gas and liquid flow viewed separately. For micro-channel modelling, the homogeneous flow assumption has been considered to give the best results by multiple researchers[26, 29].

The input array T_i of the model in Equations 3.3-3.5 is replaced with x_i, and the boundary values given by Equation 3.20. The vapour quality is defined as the fraction of the mass flow that is in the gas phase.

$$x_i = [x_0 \quad x_1 \quad \dots \quad x_{N-2} \quad x_{N-1}] \qquad \text{with: } x_i \equiv \frac{\dot{m}_{g_i}}{\dot{m}} \tag{3.19}$$

$$\text{with:} \qquad x_0 = 0; \quad x_{N-1} = 1 \tag{3.20}$$

The vapour quality x, together with the saturation pressure p_{sat}, and temperature T_{sat}, determine how some bulk parameters change. Some parameters, such as density ρ, also depend on the void fraction α, which in turn depends on some assumptions, so these will be calculated later. In all the equations below the subscripts “sat,g” and “sat,l” indicate respectively the fully saturated gas, and liquid condition.

$$h_{\text{tp}_i} = h_{\text{sat,g}} + (h_{\text{sat,l}} - h_{\text{sat,g}})x_i \tag{3.21}$$

$$\mu_{\text{tp}_i} = \frac{x_i v_{\text{sat,g}} \mu_{\text{sat,g}} + (1 - x_i) v_{\text{sat,l}} \mu_{\text{sat,l}}}{x_i v_{\text{sat,g}} + (1 - x_i) v_{\text{sat,l}}} \tag{3.22}$$

$$= \frac{x_i \mu_{\text{sat,g}} \left[\frac{\rho_{\text{sat,l}}}{\rho_{\text{sat,g}}}\right] + (1 - x_i)\mu_{\text{sat,l}}}{x_i \left[\frac{\rho_{\text{sat,l}}}{\rho_{\text{sat,g}}}\right] + (1 - x_i)} \tag{3.23}$$

$$k_{\text{tp}_i} = \frac{x_i k_{\text{sat,g}} \left[\frac{\rho_{\text{sat,l}}}{\rho_{\text{sat,g}}}\right] + (1 - x_i) k_{\text{sat,l}}}{x_i \left[\frac{\rho_{\text{sat,l}}}{\rho_{\text{sat,g}}}\right] + (1 - x_i)} \tag{3.24}$$

$$\text{Pr}_{\text{tp}_i} = \frac{x_i \text{Pr}_{\text{sat,g}} \left[\frac{\rho_{\text{sat,l}}}{\rho_{\text{sat,g}}}\right] + (1 - x_i)\text{Pr}_{\text{sat,l}}}{x_i \left[\frac{\rho_{\text{sat,l}}}{\rho_{\text{sat,g}}}\right] + (1 - x_i)} \tag{3.25}$$

The first equation 3.21 for the specific enthalpy h is the only one that is purely based on physics, as it is simply a measure for how much of the flow has been vapourised as a function of the vapour quality x. The next three equations 3.23-3.25 are for the mean two-phase viscosity μ, thermal conductivity k, and Prandtl numberPr. These *mean* parameters do not present a physical reality, like the first equation. Instead it is an average weighted by the fraction of the relative volume each phase takes in, at a given vapour quality. This is done looking at the fraction of the specific volume v each phase takes in.

This approach is taken from Carey who notes that other approaches are possible, but this one is conventional[29]. It is therefore an *assumption* that this is how the mean-two-phase properties behave. However, it must be noted that it is a truly minor assumption, because these values will only be applied to a very small channel section in the boiling phase. For the most significant part of the boiling phase, with high heat fluxes and a rapid increase in vapour quality, they will *not* be used and do not impact calculations. These averaged values will only be used to bridge the gap between the rapid boiling phase and the gas phase. Why this is done will become clear in Section 3.4.3 on the dry-out (quality) of the flow.

For other flow properties, an assumption must be made about the flow regime. In this case it is **homogeneous flow**, in which the two-phases move at the same velocity[29]. This assumption

determines how the void fraction α, the relative area the gas phase takes in a given cross-section of the flow, changes with vapour quality x.

$$\alpha \equiv \frac{A_g}{A} \tag{3.26}$$

$$u_g = \frac{\dot{m}_g}{\rho_g A_g} = \frac{\dot{m}x}{\rho_g A\alpha} \tag{3.27}$$

$$u_l = \frac{\dot{m}_l}{\rho_l A_l} = \frac{\dot{m}(1-x)}{\rho_l A(1-\alpha)} \tag{3.28}$$

$$u_l = u_g \qquad \text{(homogeneous flow)} \tag{3.29}$$

In Equation 3.26 to 3.29, A_g is the cross-sectional area through which the gas phase flows with velocity u_g. The mass flow of the gas phase is $\dot{m}_g$. The subscript l is used for the liquid phase. These equations are valid regardless of the flow regime. Equation 3.29 imposes the assumption that both phases move at the same velocity u.

Zhang et al., Carey, Kandlikar have found this to be an appropriate assumption for micro-channels[26, 29, 31]. However, it must be noted that most authors state there is quite some divergence between experimental data. It is therefore by no means established that homogeneous flow are valid for micro-channels in all circumstances. The divergent data also hints that one should by no means expect the accuracy that one has in macro-channels. One must view it as the best assumption available, and it must be validated against available VLM data for this thesis.

Equation 3.29 for the gas u_g and liquid velocity u_l can be solved to relate the void fraction and vapour fraction in terms of the density differences between the phases:

$$u_l = u_g \tag{3.30}$$

$$\frac{\dot{m}x}{\rho_g A\alpha} = \frac{\dot{m}(1-x)}{\rho_l A(1-\alpha)} \tag{3.31}$$

$$\frac{x}{\rho_g \alpha} = \frac{(1-x)}{\rho_l(1-\alpha)} \tag{3.32}$$

$$\alpha = \frac{x}{1-x}\frac{\rho_l}{\rho_g}(1-\alpha) \tag{3.33}$$

$$\alpha\left[1 + \frac{x}{1-x}\frac{\rho_l}{\rho_g}\right] = \frac{x}{1-x}\frac{\rho_l}{\rho_g} \tag{3.34}$$

$$\alpha = \frac{\frac{x}{1-x}\frac{\rho_l}{\rho_g}}{1 + \frac{x}{1-x}\frac{\rho_l}{\rho_g}} = \frac{x}{(1-x)\frac{\rho_g}{\rho_l} + x} \tag{3.35}$$

With the void fraction given by Equation 3.35, the overall flow velocity and density can be calculated:

$$\rho_{\mathrm{tp}_i} = \rho_g \alpha_i + \rho_l(1-\alpha_i) \tag{3.36}$$

$$u_{\mathrm{tp}_i} = \frac{\dot{m}}{A\rho_{\mathrm{tp}_i}} \tag{3.37}$$

Figure 3.1 demonstrates how quickly, under the homogeneous assumption, the gas fills up the channel even after only a small portion of the flow has boiled. This is due to the large difference in density of the two phases. This in turn means that the two-phase density ρ_{tp} given in Equation 3.36 quickly jumps towards the gas density, in turn greatly accelerating the flow as can be seen in Equation 3.37.

With all these newly introduced variables, the gap between the single-phase and two-phase flow is bridged, and enough information is present to start applying Nusselt numbers on the boiling flow.

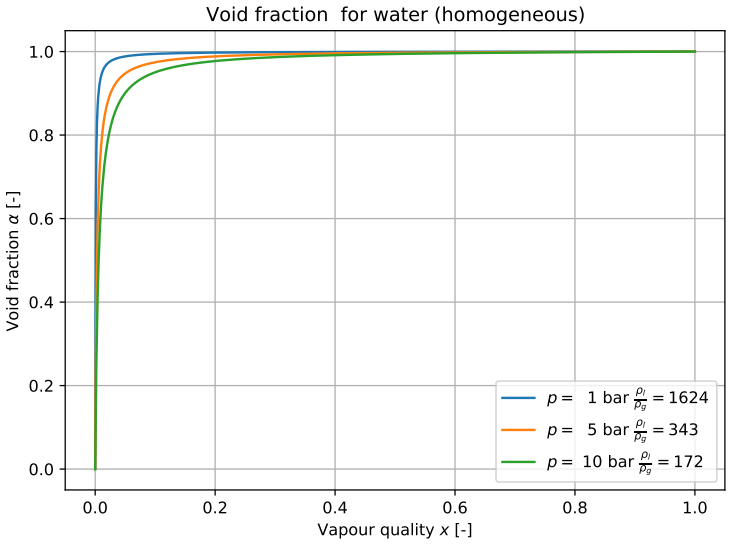

Figure 3.1: Void fraction for water at different pressures

3.2. Heat transfer and Nusselt relations

In the previous section, it was emphasized that step **B2** of the calculations could be any arbitrary Nusselt relation. In fact, great care was taken to ensure this is the case, as the validity and accuracy of the model hinges on applying the correct relations. This section completes the "fundamental model" by providing the Nusselt number Nu_i in Equation 3.15.

During literature research, it became apparent that the most practical models for two-phase heat flow in channels are based on empirical relations, and that micro-channels are not an exception to this approach[18]. To avoid empirical models one must delve into first-principle models, but it is not a given that these models are better or more "real". In reality, it is hard to have sufficient computational power to model with the numerical precision required to extract realistic and accurate behaviour from a full-blown 3D Navier-Stokes model, or even direct simulation of molecular dynamics. It is therefore not feasible to use a first-principle approach for optimization, where such computations must be run again, again and again for a large design space.

Instead, this research uses Nusselt number relations, which model heat flow as a function of flow similarity parameters like the Reynolds Re and Prandtl number Pr. The basic approach is explained here, and the actual used relations will be discussed afterwards.

Equation 3.38 relates the convective heat flux q_{conv} to a convective heat flux coefficient h_{conv} in terms of a temperature difference between the wall T_{w} and a reference temperature T_{ref}. And the **Nusselt** number Nu is defined as the ratio of convective heat flux versus conductive heat flux . It is equal to 1 if the heat flux is fully conductive[8]:

$$q_{\mathrm{conv}} = h_{\mathrm{conv}}(T_{\mathrm{w}} - T_{\mathrm{ref}}) \tag{3.38}$$

$$\mathrm{Nu} \equiv \frac{h_{\mathrm{conv}} D_h}{k} \tag{3.39}$$

The temperature T_{ref} is a reference point determined by the researcher who established the relation, and often is a (weighted) average of inlet/outlet temperatures. The wall temperature T_{w} can be replaced with an effective wall temperature T_{ew}.

3.2.1. Flow conditions

When selecting Nusselt relations from literature, one must take the flow conditions into account. It is for this purpose that extra attention was paid to existing thrusters and their flow conditions in Section 2.2.6 and Table 2.4.

The following flow conditions are often used:

- Two-phase or single-phase flow relation

- Geometric constraints
- Flow similarity parameters and/or mass flux G
- Mass flux

The geometric constraints often concern the shape of the channel. For older experiments, on macro-scale channels, circular cross-sections are the norm. For mini- and micro-channels the channels are more often rectangular and straight. These shapes do not always correspond to the geometry used for VLM. When a relation for a circular cross-section is applied to a channel with a different shape, usually the hydraulic diameter D_h is used as a reference length. This diameter is used to compare the channels in terms of the relative size of the cross-sectional area A and the wetted perimeter P. In this way channels are compared to a circular channel which has the same relation between the two values.

$$D_h \equiv \frac{4A}{P} \tag{3.40}$$

$$= \frac{2d_c w_c}{(d_c + w_c)} \qquad \text{for rectangular cross-sections} \tag{3.41}$$

Flow similarity parameters are used to quantify the relation between the flow regime and the actual heat flux. It is important to note that some parameters are given in terms of a certain reference length (often D_h) or reference temperature T_{ref}. It is important that the reference values used for calculating the parameters in a Nusselt number relation are the same as those used to calculate the final heat flow in Equation 3.38.

$$\text{Re} \equiv \frac{\rho u L}{\mu} = \frac{GL}{\mu} \tag{3.42}$$

$$\text{Pr} \equiv \frac{c_p \mu}{k} \tag{3.43}$$

$$\text{Bo} \equiv \frac{g(\rho_l - \rho_g)D^2}{\sigma} \tag{3.44}$$

The Reynold's number Re is the ratio between inertial and viscous forces in a flow[16]. It is not only used to calculate the Nusselt number Nu, but often used to distinguish between flow regimes. One selects the applicable relation often based on Re, with higher numbers indicating turbulent flow, and lower numbers laminar flow.

The Prandtl number Pr is the ratio between energy dissipating through friction, compared to energy transporting through conduction[16].

The Bond number Bo gives the ratio between buoyancy forces and surface tension forces in boiling flows. Kandlikar and Balasubramanian thought it would not be applicable in micro-channels due to the lack of importance of gravity in micro-channels[27]. However, it still shows up in their nucleate boiling relation for micro-channels. Probably because it can also be viewed as a parameter that captures the relative importance of the relative force of expanding bubbles $(\rho_l - \rho_g)$, compared to the effect of channel size/surface tension D^2. The gravity term g would then simply be an artefact related to the previous use cases of the Bond number.

In section 3.3 and 3.4 the used Nusselt number relations for respectively single-phase and two-phase flow will be summarized.

3.3. Single-phase

In this section Nusselt relations that could be applicable to the single-phase heat transfer in VLM are presented. It starts with laminar duct flow in Section 3.3.1, and continues with turbulent flow in Section 3.3.2.

Beforehand it was unknown in which flow regime the optimal solutions would lie. In Section 4.2.5 it is validated whether the assumed flow similarity parameters were correct.

3.3.1. Laminar duct flow

Bejan discusses the behaviour of laminar duct flow in the book *Convection Heat Transfer*. In it is described how the growth of the boundary layer affects the heat flow. When the boundary layer is fully developed (i.e.: the boundary layers from opposing walls meet in the middle), and the channels sufficiently long, the Nusselt numbers are constant for the given boundary conditions(from Table 3.3)[32]:

$$\mathrm{Nu} = 3.614 \quad \text{for constant wall temperature in square channels} \tag{3.45}$$
$$\mathrm{Nu} = 2.98 \quad \text{for constant heat flux in square channels} \tag{3.46}$$
$$\mathrm{Nu} = 3.66 \quad \text{for constant wall temperature in circular channels} \tag{3.47}$$
$$\mathrm{Nu} = 4.36 \quad \text{for constant heat flux in circular channels} \tag{3.48}$$

To see whether it is applicable the hydrodynamic entrance length X_T must be estimated with Eq. 3.49, which is the section where the boundary layers are developing and have not yet met. This length should be considered an estimation of approximate magnitude, as it varies quite a bit with the assumption of the velocity profile:

$$\frac{X_T}{D} \approx 0.04\mathrm{Re} \tag{3.49}$$

Applied to liquid section of Silva et al.'s VLM as reference, with $D_h = 136\mu$m and the Reynold's number Re ≈ 1 (see Table 2.4), the length of da Silva's channel is 3 orders of magnitude larger. The relations from Eq. 3.45 and 3.48 could therefore be applicable. It is not clear what the value must be when the channel is rectangular instead of square or circular. It will be assumed that the relations for square channels are applicable, because at least for the square case the hydraulic diameter is exactly the same. Furthermore, the a constant wall temperature is assumed. Therefore, when a laminar flow relation is required, Equation 3.45 will be used for channels with rectangular cross-section.

3.3.2. Turbulent duct flow

The Dittus-Boelter heating relation is used for turbulent pipe flow in straight smooth tubes with diameter D, which is replaced by the hydraulic diameter D_h for non-circular channels in this model.

$$\mathrm{Nu} = 0.023\mathrm{Re}_{D_h}^{0.8}\mathrm{Pr}^{0.4} \tag{3.50}$$
$$T_{\mathrm{bulk}} \equiv \frac{T_{\mathrm{in}} + T_{\mathrm{out}}}{2} \tag{3.51}$$

Re and Pr must be evaluated at the bulk temperature for this relation, which is the average of the inlet temperature T_{in} and outlet temperature T_{out}. It is applicable for *single-phase* flow with: $2500 <$ Re < 120000, $0.7 <$ Pr < 700, and $\frac{L}{D} > 60$. Within this range the accuracy is +/- 40% [8].

3.4. Two-phase

As was mentioned in Section 3.1.2, the two-phase thermal conductivity k_{tp} is an ill-defined property. For that reason, it is convention to instead define the Nusselt number for two-phase flow in relation to k_{le}. This is the conductivity if the flow would be entirely liquid instead, i.e.: a saturated fully liquid flow ($k_{le} = k_{\mathrm{sat,l}}$). So, the two-phase Nusselt number Nu_{tp} is defined different than the single-phase Nu in Equation 3.39.

$$\mathrm{Nu}_{tp} \equiv \frac{h_{\mathrm{conv}} D_h}{k_{le}} \tag{3.52}$$

The "mean" two-phase properties, defined by Equations (3.23-3.25) might however, still be of use, after dry-out. This is described in Section 3.4.4.

Below the possible applicable relations are summarized, and in Section 4.2.5 their applicability is checked for validity.

3.4.1. Nucleate boiling for Re_{le} < 100

One recommended relation from literature for micro-channel flow is Kandlikar and Balasubramanian's relation[27, 33] suggested in the work of Carey[29]. It asserts that the dominant mechanism is nucleate boiling when $\mathrm{Re}_{le} < 100$. This is the Reynold's number if the flow where to be entirely liquid.

$$\mathrm{Re}_{le} \equiv \frac{GD}{\mu_l} \tag{3.53}$$

This mechanism quickly tapers off with increased quality of the flow:

$$h_{\mathrm{NBD}} = 0.6683 \left[\frac{\rho_{\mathrm{sat,l}}}{\rho_{\mathrm{sat,g}}}\right]^{0.1} x^{0.16}(1-x)^{0.64} h_{le} + 1058.0\mathrm{Bo}^{0.7} F_K (1-x)^{0.8} h_{le} \tag{3.54}$$

This relation states that the heat transfer due to nucleate boiling h_{NBD} is enhanced compared to regular heat transfer h_{le}, at saturated liquid conditions ($x = 0$). This enhancement shoots up drastically at low vapour quality, and quickly tapers off, a prediction that fits well with the explosive boiling reported in VLM[13]. The increased heat transfer depends on the density ratio of the fluid $\frac{\rho_{\mathrm{sat,l}}}{\rho_{\mathrm{sat,g}}}$, and on the Bond number Bo(Equation 3.44). F_K is a fluid-dependent constant, and is 1 for water.

In Figure 3.2 the relation has been calculated with the laminar h_{le}. The used relation was Equation 3.46 for laminar developed flow in a square channel and constant wall temperature.

It can also be seen that this correlation goes to zero as $x \to 1$, resulting in an infinitely long channel in a numerical model. In reality, dry-out occurs and a combination of the following two results occur:

- The boiling heat transfer is so drastically reduced, it is hard to reach a flow quality of 1.
- The flow regime changes, and boiling occurs with different heat transfer mechanism (e.g.: convective boiling, mist flow)

More on dry-out in Section 3.4.3.

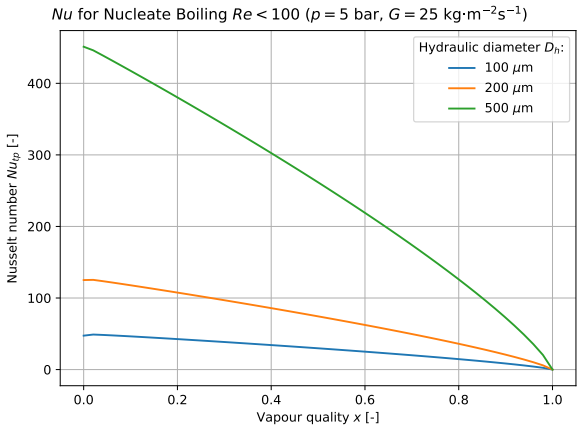

Figure 3.2: Nu for nucleate boiling in micro-channels $Re < 100$

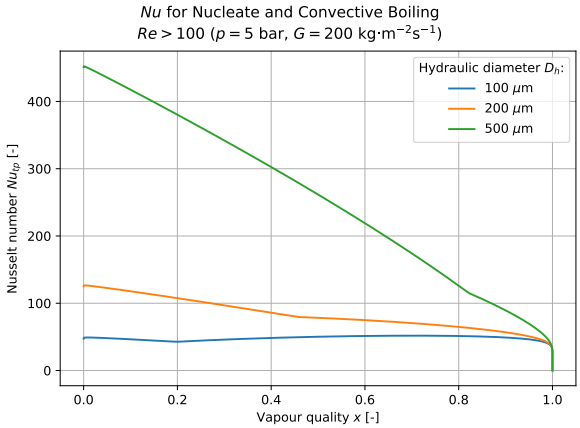

Figure 3.3: Nu for nucleate and convective boiling in micro-channels $Re > 100$

3.4.2. Nucleate and convective boiling for Re > 100

The relation used in the previous section is a simplified version of the one presented here. For channels with $\mathrm{Re}_{le} < 100$, Kandlikar and Balasubramanian stated that regular convective boiling played no major role, and could be ignored. If it is not discarded the convective boiling coefficient h_{CBD} given by Equation 3.55, and the Nusselt number is determined by the maximum of h_{NBD} and h_{CBD} in Equation 3.56. The same laminar flow relations for h_{le} are applicable, up to the point $\mathrm{Re}_{le} < 1600$[33]. Examples of the resulting Nusselt numbers are plotted in Figure 3.3.

$$h_{\text{CBD}} = 1.1360 \left[\frac{\rho_{\text{sat,l}}}{\rho_{\text{sat,g}}}\right]^{0.45} x^{0.72}(1-x)^{0.08} h_{le} + 667.2\text{Bo}^{0.7} F_K (1-x)^{0.8} h_{le} \quad (3.55)$$

$$\text{Nu}_{tp} = \max(h_{\text{NBD}}, h_{\text{CBD}}) \quad (3.56)$$

3.4.3. Dry-out

In earlier given relations, heat transfer goes to 0, as the vapour quality increases to 1 ($x \to 1 : \text{Nu} \to 0$).

For macro-scale channels two correlations are recommended for calculating the dry-out quality $x_{\text{dry-out}}$[6]. Equation 3.58 is for tubes with 8mm diameter. Equation 3.59 adapts it to different diameters.

$$P = \frac{p}{98 \cdot 10^5} \quad (3.57)$$

$$x_{\text{dry-out}_{8mm}} = \left[0.39 + 1.57P - 2.07P^2 + 0.68P^3\right] \left(\frac{\dot{m}}{A \cdot 10^3}\right)^{-0.5} \quad (3.58)$$

$$x_{\text{dry-out}} = x_{\text{dry-out}_{8mm}} \left(\frac{8 \cdot 10^{-}3}{D_h}\right) \quad (3.59)$$

Combined, for mass fluxes, diameters and pressures expected in VLM the following Figure 3.4 is obtained. Sadly, it is clear that these correlations are not applicable to the relatively low pressures and mass fluxes. Virtually all calculations in the sub-100 mass flux G range, are well above 1, and a dry-out quality above 1 is nonsensical.

It does, however, indicate that as mass fluxes and channel diameter decrease, early dry-out seems to be unlikely, and full evaporation is to expected. This makes sense as well, as in smaller channels it is easier for liquid to continue clinging to the walls, and with lower velocities it is less likely droplets shear of the wall. On the other hand, this is based on visual inspection of flows in micro-channels and VLM, and it is not unthinkable that mist flow occurs, in which small droplets are suspended in the flow. These drops are not directly visible. Still, it leaves the question of how the calculations should transition to the gas phase, for which a solution will be posed in the next section.

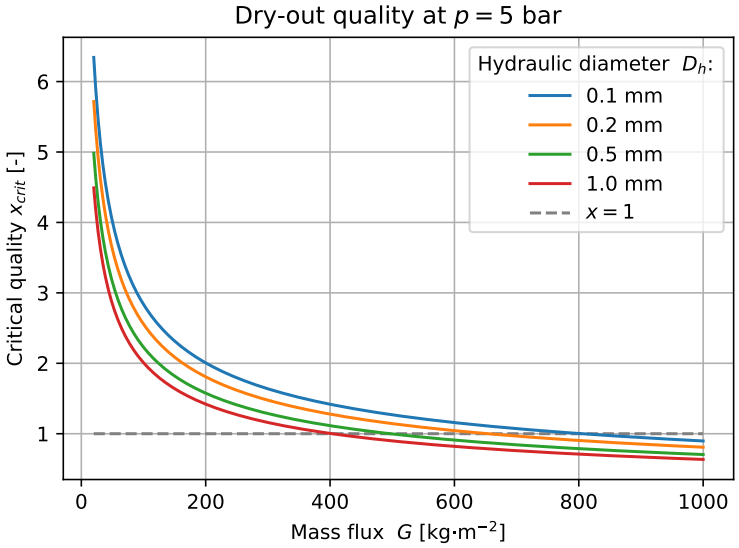

Figure 3.4: Predicted dry-out quality, applied to micro-channels

3.4.4. Mist flow

The phenomenon that the heat flux abruptly flattens off, even at increased temperatures is called Critical Heat Flux (CHF), as it becomes increasingly hard to transfer heat to a flow of high quality, even if wall

[6]Also called “critical quality” x_{crit}

temperatures are increased. This is the most likely reason that Equation 3.56 tapers off so drastically. Carey suggests that at this point, three flow regimes could take over[29]:

- Transition flow boiling
- Convective film boiling
- Mist flow evaporation

Transition flow boiling is poorly understood, but "rarely occurs in normal operating conditions" and is mostly of interest when loss-of-coolant accidents occur in nuclear power plants[29]. Kandlikar and Balasubramanian state that convective boiling is not important for $Re < 100$, which is supported by their data[33]. When $Re > 100$ convective boiling is already taken into account with Equation 3.56. This does suggest in both cases after the wall is dried out, that mist flow evaporation is starting to occur. In this process droplets and vapour in the flow are heated through several mechanisms at once, such as: radiation from the wall to the droplet, droplets impacting the channel walls and evaporating, radiation/convection from the wall to the vapour, and the vapour to the droplets[29].

Carey summarizes several mist flow relations found in literature, but all assume turbulent conditions[29]. The simplest relation is applied for turbulent flow, as all relations will in essence just be a smooth interpolation, with minimal impact on the overall heat flow. For the purpose of this thesis, no meaningful differences between the other available relations are expected.

Furthermore, when searching literature on (fully developed) laminar mist flow boiling, it became apparent that this flow regime has not really received any special attention yet. To solve this issue, it will be assumed that turbulent and fully developed laminar flow transition through mist flow, towards single-phase gas flow in the same manner, but with different relations. To explain and justify this, it is first necessary to discuss the turbulent case.

In case the flow is homogeneous, and assumed to be turbulent, the Dittus-Boelter relation is applicable to the two-phase flow, with the "appropriately defined mean properties".

$$\mathrm{Nu}_{\mathrm{DB,tp}} = \frac{h_{\mathrm{conv}} D_h}{k_{\mathrm{tp}}} = 0.023 \left[\frac{\dot{m} D_h}{A \mu_{\mathrm{tp}}}\right]^{0.8} \mathrm{Pr}_{\mathrm{tp}}^{0.4} \tag{3.60}$$

The suggested properties in Equation 3.60 are precisely those given earlier in Equations (3.23-3.25). The method to calculate these mean properties are not set in stone, and Carey argues that, in fact, the mean properties could be improved by correlating them to experimental data. However, for this thesis, it is assumed that the choice of mean properties is not significant.

Also, regardless of the defined properties, all properties must eventually converge to gas saturation conditions, and must necessarily be close to those values. So no major deviations from the current method can be expected at high quality flows and turbulent flows.

Thus, for the turbulent case, it seems fair to amend the Nusselt relation with mist flow, through a continuous transition. This is done by letting mist flow take over in the model when it is greater than the value calculated for nucleate boiling(Eq.: 3.54) and convective boiling(Eq.:3.55) in turbulent micro-channels:

$$\mathrm{Nu}_{\mathrm{tp}} = \max(\mathrm{Nu}_{\mathrm{NBD}}, \mathrm{Nu}_{\mathrm{CBD}}, \mathrm{Nu}_{\mathrm{DB,tp}}) \tag{3.61}$$

For the turbulent case, this results in a smooth transition towards the single-phase Dittus-Boelter correlation, which is of course, equal to the two-phase Dittus-Boelter correlation at $x = 1$. It is important to note that the mist flow regime occupies such a small part of the two-phase flow that, under all these assumptions, the Nusselt number after dry-out is roughly equal to a linear interpolation(from the point of "dry-out" towards the single-phase gas relation). Regardless of the used relation, the mist flow regime is therefore quite inconsequential for the final result.

As there is no information on the case of fully developed laminar flow, and it is well outside the scope of the thesis to establish what is applicable, it will be assumed that laminar flow case will behave similarly. That is, it will transition smoothly to the relevant single-phase relation, whilst being related to the same "appropriately defined mean properties".

In this case this would mean it would transition to one of the relations with a constant Nusselt number(Eq. 3.45 to 3.48), but that this constant is related to “mean two-phase conductivity” k_{tp} (Eq. 3.24) instead. This is then done in the following manner:

$$\mathrm{Nu}_{\mathrm{FDL,tp}} = C \tag{3.62}$$

$$h_{\mathrm{conv}\,\mathrm{FDL,tp}} = \frac{\mathrm{Nu}_{\mathrm{FDL,tp}} k_{tp}}{D_h} \tag{3.63}$$

$$\mathrm{Nu}_{\mathrm{tp}} = \max(\mathrm{Nu}_{\mathrm{NBD}}, \mathrm{Nu}_{\mathrm{FDL,tp}}); \qquad \text{when: } \mathrm{Re}_{le} < 100 \tag{3.64}$$

$$\mathrm{Nu}_{\mathrm{tp}} = \max(\mathrm{Nu}_{\mathrm{NBD}}, \mathrm{Nu}_{\mathrm{CBD}}, \mathrm{Nu}_{\mathrm{FDL,tp}}); \qquad \text{when: } \mathrm{Re}_{le} > 100; \tag{3.65}$$

3.4.5. Effective wall temperature

As the multiple channels in the chip are heating from one side only, there will be temperature profile along the channels walls. This means that T_{w} in Equation 3.38 is not a constant. This modulates the effective heat transfer, in a manner that is almost similar to the behaviour of extended fins in heat exchangers. Without modelling this effect, the optimization would tend to walls of zero thickness. This is because it would reduce the overall heat loss of the chip by simply reducing the area. In reality, there is a penalty for making the walls arbitrarily small, and calculating the fin effectiveness will take this negative effect into account.

Arguably channel walls and fins are not the same, but mathematically speaking fins touching the opposite side of the channel is simply a special case of fins. The fact that the channel walls do not have a perimeter, is also trivial. This will be shown in the derivation below, which closely follows earlier derivations of this common heat transfer problem[34, 35], but in a subtle variation. Solving the differential equation results in a temperature profile along the wall, and a distinct temperature at the top and bottom of the channel. The new temperature profile and bottom temperature can be used to calculate the heat flow in Equation 3.38 more accurately, while h_{conv} remains constant as it based on the unchanged flow conditions.

To keep the notation concise and clear, some variables symbols in the derivation are switched to conventional symbols for heat transfer problems. These are different from those in the rest of the report: x is the length from the channel wall from the top of the heater ($x = 0$) to the bottom ($x = d_c$). The channel depth d_c is the total height of the channel wall. $T(x)$ is the temperature of the channel wall at location x. t is the thickness of the channel wall (spacing width s_c elsewhere in the report). dL is the infinitesimally small length of the fin in the direction of flow, and equal to the variable in Equation 3.18. dL cancels out, so it is not problematic that the result of the heat flow calculation is used in the derivation.

At each location x in an infinitesimally small fin section of height dx and length dL, conservation of energy must be imposed. There is:

- Heat flowing into the control volume from the top $q_{in} = -ktdL\frac{dT}{dx}$
- Heat flowing out of the control volume: $q_{out} = -ktdL\frac{dT}{dx} + \frac{d}{dx}\left[ktdL\frac{dT}{dx}\right]dx$
- Heat convected from the wall to the fluid $q_{h_{\mathrm{conv}}} = 2h_{\mathrm{conv}}dxdL(T - T_{fl})$

In these terms k is the thermal conductivity of the fin. The thermal conductivity k of silicon is quite dependent on temperature as seen in Appendix D.1 on the properties of silicon. At room temperature around $k \approx 150$ $\mathrm{Wm^{-1}K^{-1}}$, and it is around 30 $\mathrm{Wm^{-1}K^{-1}}$ at 1000 K. For this research the thermal conductivity is set to the value at 700 K at about 50 $\mathrm{Wm^{-1}K^{-1}}$.

Equating the flow of heat in and out results in a common differential equation:

$$q_{in} = q_{out} + q_{h_{\mathrm{conv}}} \tag{3.66}$$

$$-ktdL\frac{dT}{dx} = -ktdL\frac{dT}{dx} + \frac{d}{dx}\left[ktdL\frac{dT}{dx}\right]dx + 2h_{\mathrm{conv}}dxdL(T - T_{fl}) \tag{3.67}$$

$$0 = -kt\frac{d^2T}{dx^2} + 2h_{\mathrm{conv}}T_{fl} \tag{3.68}$$

At this point it is convention to introduce a change of variables($\theta(x) = T(x) - T_{fl}$), and to introduce the new parameter $m = \sqrt{\frac{2h_{\text{conv}}}{kt}}$. This turns the equation into a heat transfer problem with a negative eigenvalue of $\lambda = -m$. Equation 3.70 is the general solution.

$$0 = \frac{d^2\theta}{dx^2} - m^2\theta \tag{3.69}$$
$$\theta(x) = C_1 \sinh(mx) + C_2 \cosh(mx) \tag{3.70}$$

An attempt was made to solve this boundary value problem without introducing an iteration. This required solving a heat balance equation, with the the first derivative $\theta'(L)$ at the bottom of the heater. The initial attempt to equate this with the radiation losses at the bottom yielded the insight that a closed-form solution exists. This solution, however, quite literally spanned multiple pages with many complex terms with high exponentiations of hyperbolic function, and potential singularities (e.g.: $\frac{1}{\tanh^2 x}$) . This solution did not even involve all heat flows of interest. It would require too much time to investigate whether this solution would numerically be accurate. Therefore, the choice was made to solve the system for two known temperatures $T(0)$ and $T(L)$ and to iterate towards a heat balance. Naturally, this introduces a performance hit on the optimization.

Continuing with the boundary value problem:

$$\theta(0) = C_2 \tag{3.71}$$
$$\theta(L) = C_1 \sinh(mL) + C_2 \cosh(mL) \tag{3.72}$$

The straightforward solution is:

$$C_1 = [\theta(L) - \theta(0)\cosh(mL)]\,\text{csch}(mL) \tag{3.73}$$
$$C_2 = \theta(0) \tag{3.74}$$
$$\theta(0) = T_{top,wall} - T_{fl} \tag{3.75}$$
$$\theta(L) = T_{bottom,wall} - T_{fl} \tag{3.76}$$

Additional equations are required to determine the effective temperature of the “fins”, and to solve the energy balance at the bottom of the chip:

$$\theta_{\text{effective}} = \frac{1}{L}\int_0^L C_1 \sinh(mx) + C_2 \cosh(mx)dx \tag{3.77}$$
$$= \frac{1}{mL}\left[C_1(\cosh(mL) - 1) + C_2 \sinh(mL)\right] \tag{3.78}$$
$$\theta'(L) = C_1 m \cosh(mL) + C_2 m \sinh(mL) \tag{3.79}$$

For the energy balance, the assumed bottom wall temperature makes conduction in directions other than through the channel walls impossible. Like in the rest of the model, channels are expected to behave identically. This means that only the heat flow through the bottom area of one channel and one channel wall must be evaluated[7].

The heat balance equation is:

$$0 = \int_0^Y \theta'(L)ktdy \tag{3.80}$$
$$+ \int_0^Y \varepsilon\sigma T(L)^4(w_c + t)dy \tag{3.81}$$
$$+ \int_0^Y h_{\text{conv}}(T(L) - T_{fl})w_c dy \tag{3.82}$$

[7]This is equivalent to evaluating two half channel walls around the channel

The notation requires some clarification due to clashes with conventional notation: Y represents the length along the channel (l_c elsewhere in the report), t is the wall thickness (s_c elsewhere), and w_c is the channel width. $T(L)$ is the bottom wall temperature (T_{bw}).

For the remainder of the report it is important to establish new definitions, and new heat transfer calculations when fin effectiveness is taken into account:

$$T_{\text{bw}} \equiv T(L) = \theta(L) + T_{fl} \tag{3.83}$$

$$T_{\text{sw,eff}} \equiv \theta_{\text{effective}} + T_{fl} \tag{3.84}$$

$$T_{\text{ew}} = \frac{(T_{\text{w}} + T_{\text{bw}})w_c + 2T_{\text{sw,eff}}d_c}{2(w_c + d_c)} \tag{3.85}$$

$$A_{\text{p}_i} = \frac{\dot{Q}_i}{h_{\text{conv}_i}(T_{\text{ew}_i} - T_{\text{ref}_i})} \tag{3.86}$$

As mentioned before, it was infeasibly to find or apply a closed-form solution to this boundary value problem. Instead, the program iterates towards the bottom wall temperature where energy is conserved (See Program Flow in Figure 2.5).

3.5. Pressure drops

Whilst pressure changes do not significantly affect the overall heat transfer of channels, and they tend to be small in existing VLM, early results suggested that optimal heating efficiency is most likely achieved at higher Reynold's numbers. This resulted in optimal solutions with pressure drops that required significant changes to the throat width, in order to maintain specified set of performance parameters $(F, I_{sp}, \dot{m})$.

It is, however, still possible to factor in the pressure drop, by calculating it after the channel length has been determined with the constant pressure assumption. The pressure drop, therefore only affects the nozzle geometry.

The pressure drops that are relevant in micro-channels are:

- Accelerative pressure drop Δp_{acc}
- Frictional pressure drop Δp_{fric}
- Contraction/expansion pressure drop $\Delta p_{\text{con}}/\Delta p_{\text{exp}}$

The total pressure drop Δp_{total} then is:

$$\Delta p_{\text{total}} = \Delta p_{\text{acc}} + \Delta p_{\text{fric}} + \Delta p_{\text{con}} + \Delta p_{\text{exp}} \tag{3.87}$$

Pressure drop due to acceleration, is only of interest if it would affect the heat transfer. It is the only pressure drop that does not have be factored as a loss. This is because the energy is not lost, but used to accelerate the flow. The total pressure p_0 is conserved, whilst the static pressure drops. It is the total/chamber pressure $p_c = p_0$ which determines the nozzle performance in Ideal Rocket Theory (IRT), so its effect is zero in the ideal case.

Pressure drops due to friction and due to sudden contraction/expansion at the inlet/outlet manifold are, however, real losses. This actual loss in total pressure p_0 will be described by Equation 3.88 with the actual pressure *loss* Δp_{loss}. These losses necessitate a larger throat width to maintain nozzle performance. It is this changed nozzle geometry that affects the heat losses, or determines the bounds of the design space.

$$\Delta p_{\text{loss}} = \Delta p_{\text{fric}} + \Delta p_{\text{con}} + \Delta p_{\text{exp}} \tag{3.88}$$

Finally, pressure drop due to elevation of the fluid, are generally irrelevant in micro-channels.

3.5.1. Accelerative pressure drop

The nature of accelerative pressure drops is explained here, for readability of the report, but it must be noted that it does not affect nozzle performance.

The pressure drops as the fluid accelerates due to evaporation. It is easily derived from the conservation of momentum in steady flow through a straight channel. The change in momentum between two points along the channel is equal to the net pressure force applied between the two sections.

$$\Delta pA = \dot{m}u_1 - \dot{m}u_2 \tag{3.89}$$

$$\Delta p = \rho_1 u_1^2 - \rho_2 u_2^2 \tag{3.90}$$

$$\Delta p = G^2\left(\frac{1}{\rho_1} - \frac{1}{\rho_2}\right) \qquad \text{with: } G \equiv \frac{\dot{m}}{A} \tag{3.91}$$

$$\Delta p \approx -G^2\frac{1}{\rho_2} \qquad \text{if: } (\rho_1 >> \rho_2) \tag{3.92}$$

G is the mass flux, through the channel, which is usually constant. So the acceleration pressure drop during steady flow only depends on the density change of the fluid. It is interesting to note that this basic equation predicts an explosive boiling process, once the saturated fluid starts boiling. As the first bubbles form, the pressure drops as the gas accelerates. This results in an even lower saturation temperature, causing more liquid to evaporate, and the cycle repeats. This means the boiling interface moves forward until it reaches the point where the liquid is at saturation temperature again. This explosive boiling process can however, not be modelled with steady flow assumptions.

Since the gas density ρ_g is much lower than the liquid density ρ_l, with the gas density being about 1.0-2.5 kg/m^3 at $p = 5$ bar for various temperatures, the worst case magnitude of the pressure drop is simply the mass flux squared. Existing VLM heating channels have mass fluxes below $G < 50$ kg·m^{-2}. The pressure drop can thus be expected to be below $\Delta p < 0.025$ bar, or $\Delta p/p < 0.5\%$. It is therefore assumed that its effect is negligible on the heat transfer in the channel.

3.5.2. Frictional pressure drop

In contrast to acceleration pressure drops, frictional pressure drops pose a problem for calculating a consistent solution with IRT. This is because it is an actual energy loss, and therefore the total pressure p_0 actually drops. IRT then predicts that the nozzle will no longer have the same performance (Eq. (2.1-2.8)).

A conventional approach for calculating frictional pressure drop Δp is the Darcy-Weisbach relation[8]:

$$\Delta p = \frac{l_c}{D_h}\frac{1}{2}f\rho u^2 \tag{3.93}$$

Ribatski, Wojtan, and Thome have also looked at what methods are applicable for two-phase frictional pressure drop estimations of micro-channels. They conclude that there are problems with the experimental data as there are many inconsistencies, but nonetheless they tried to determine which method is the most suitable at this point in time. Their dataset goes down to hydraulic diameters of 0.2 mm to 3 mm, and covers many different fluids (mostly hydrocarbon refrigerants). They conclude: "*the best prediction was obtained by the macroscale method proposed by Müller-Steinhagen and Heck , which ranked a close second according to* λ [proportion of data within 30% accuracy] *and first according to* ϵ [mean absolute error], *with values of 53.1% and 31.3%*"[36].

The approach by Müller-Steinhagen and Heck takes a pressure drop per unit length of the liquid A and gaseous B phase. They combine them into one two-phase pressure drop $\left(\Delta p_{f,tp}\right)$ as a function of vapour quality x[37]. The single-phase equations are thus simply a variation of the Darcy-Weisbach relation above (Eq. 3.93):

$$\left(\frac{dp}{dL}\right)_{f,l} = f_l \frac{1}{2}\frac{1}{D_h}\rho_l u_l^2 \qquad = A \tag{3.94}$$

$$\left(\frac{dp}{dL}\right)_{f,g} = f_g \frac{1}{2}\frac{1}{D_h}\rho_g u_g^2 \qquad = B \tag{3.95}$$

$$f_{l,g} = \frac{64}{\mathrm{Re}_{l,g}} \qquad ;\ \text{for: Re} << 1187 \tag{3.96}$$

$$f_{l,g} = \frac{0.3164}{\mathrm{Re}_{l,g}^{\frac{1}{4}}} \qquad ;\ \text{for: Re} > 1187 \tag{3.97}$$

They are combined with the following formula, in which $C = 3$ is empirically determined:

$$\left(\frac{dp}{dL}\right)_{f,tp} = [A + 2\,(B - A)\,x]\,(1 - x)^{\frac{1}{C}} + Bx^C \tag{3.98}$$

3.5.3. Pressure drop due to sudden area change

While the pressure does normally also drop as the area changes, due to acceleration, if the area changes suddenly there are also losses associated with that sudden change. This loss will not be recovered as the area changes back to its initial value. These losses can be expected at the inlet and outlet of the heating chamber. It is important to note that as the fluid enters or exits the chamber it is *single-phase*.

The sudden area change is described by the ratio of the smallest cross-sectional channel area A_s, and the largest area A_l. In the case of multi-channel VLM heating chambers with constant channel depth, it is calculated by:

$$\frac{A_s}{A_l} = \frac{N_c w_c}{w_{\text{inlet}}} \tag{3.99}$$

In this N_c is the number of channels with a width of w_c. w_{inlet} is the width of the inlet manifold before sudden contraction. See Figure 3.6 for details.

For macro-channels the loss factor for sudden contraction ζ_c or expansion ζ_e are given by[8]:

$$\Delta p = \frac{1}{2}\rho\zeta {u_s}^2 \tag{3.100}$$

$$\zeta_c = \frac{1}{2}\left(1 - \frac{A_s}{A_l}\right)^{\frac{3}{4}} \tag{3.101}$$

$$\zeta_e = \left(1 - \frac{A_s}{A_l}\right)^2 \tag{3.102}$$

In these equations u_s is the flow velocity in the smallest channel, and A_s and A_l are the cross-sectional area of the smallest and largest channel respectively. Since it is not mentioned in literature, it is useful to note here that for multi-channels, it does not matter if the contraction pressure drop is calculated relative to the single-channel velocity in one of the channels. Equation 3.100 can be rewritten to show that its invariant to the amount of channels. ζ is really multiplied with the total dynamic pressure in the flow, which in turn is related to the mass flux G. The mass flux is not affected by whether one evaluates the pressure drop for all channels combined, or by applying it to a single channel.

$$\Delta p = \frac{1}{2}\rho\zeta {u_s}^2 = \frac{1}{2}\zeta\frac{G^2}{\rho} \tag{3.103}$$

(3.104)

Like most micro-channel phenomena the pressure drop due to sudden contraction has not been studied a lot yet. Kawahara et al. compared experimental data and correlations for contraction coefficients C_C for small rectangular micro-channels, with Re ranging from about 10 to just over 1000. For the Reynold's number above 100 the RMS errors were mostly within 10 %, and for the very low Reynold's number below a 100 the experimentally determined contraction loss was less accurate, but lower than expected. The loss is calculated with Equations (16),(17)&(19) from their paper[38], which are presented below in Equation 3.105 and 3.106. Figure 3.5 shows the resulting coefficients and how well they correlate with experimentally determined values.

$$\zeta_c = \left(1 - \frac{1}{C_C}\right)^2 \tag{3.105}$$

$$C_C = B + (1 - B)\left[\frac{A_s}{A_l}\right]^{4.519} \tag{3.106}$$

$$\text{with:} \quad B = 0.0645 \ln \mathrm{Re}_{D_h} - 0.00792 \tag{3.107}$$

In this equation Re_{D_h} is the Reynold's number downstream, after contraction.

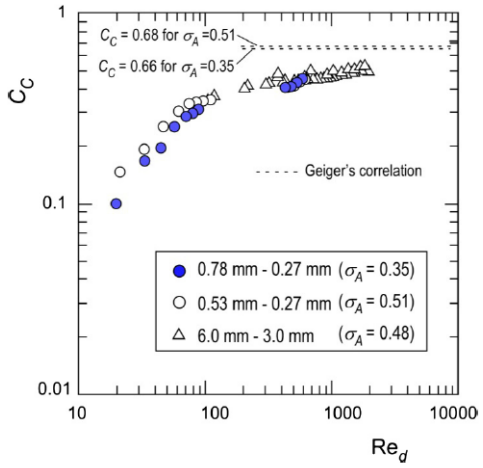

Fig. 15. Contraction coefficient for single-phase liquid flows in micro- and mini channels.

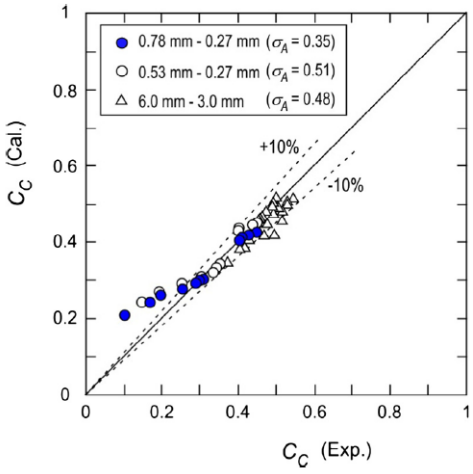

Fig. 16. Comparison of contraction coefficient between experiment and calculation by the present empirical correlation.

Figure 3.5: Contraction coefficient and its accuracy. (Fig. 15 and Fig. 16 reproduced from the work of Kawahara et al.[38])

σ_A is $\frac{A_s}{A_l}$

No similar work was found on expansion losses. This may be due to the fact that these losses are considered to be small in experiments. For, example: Coleman found that in outlet manifolds with area ratios below 0.1, expansion losses make up less than 5% of the overall pressure drop[39]. Whether this is the case for the design space in this research, is unknown.

3.5.4. Nozzle adaptation after pressure drop

For optimization purposes it is required that the high-level performance parameters $(F, \dot{m}, I_{sp})$ are maintained between iterations, as otherwise the comparisons between designs are not meaningful(**TLR-01** and **REQ-01**). The changed nozzle area significantly impacts the area through which heat can be radiated or conducted away to the environment. The area ratio $\frac{A_e}{A_t}$ is unchanged, as otherwise it would not be possible to compare between designs with the same I_{sp}.

From Equation 2.2 follows that the throat area A_t must be adapted to maintain the mass flow $\dot{m}$, as only the chamber pressure p_c has changed. The requirement is thus that the product of chamber pressure and throat area remains constant:

$$p_c A_t = \text{constant} \tag{3.108}$$

To maintain I_{sp} and thrust, also the pressure ratio $\frac{p_e}{p_c}$ needs to remain constant, which remains constant if the area ratio $\frac{A_e}{A_t}$ is constant. This follows from Equation 2.1 for thrust, where the exit velocity u_e remains constant if $\frac{p_0}{p_e}$ is constant, and the product of p_e and A_e remains constant, as follows from the requirement of constant mass flow in 3.108:

$$p_e A_e = \frac{p_e}{p_c} p_c \frac{A_e}{A_t} A_t = \text{constant} \tag{3.109}$$

Of course this is only true insofar the back pressure p_a is zero. In this research, it is zero as the thruster designs are optimized for vacuum conditions (and can be tested in (near-)vacuum chambers).

It is, however, also important how real nozzle effects impact the above described requirements for nozzle adaptations. Makhan has summarized and investigated real nozzle effects[20]. Looking at the used empirical relations for the discharge coefficient C_d, divergence loss C_{div}, and C_{visc} in Appendix C, it becomes clear that:

- The divergence loss C_{div} is insensitive to the changes (Eq. C.4)
- The discharge coefficient C_d is unchanged if the Reynold's Re_t number in the throat is unchanged (C.12).
- The viscous loss C_{visc} is unchanged if area ratio $\frac{A_e}{A_t}$ and Re_t is unchanged.

It is already known that the area ratio is unchanged, but the change to the throat Reynold's number is so slight for the changed hydraulic diameter D_h at the throat, that it results in no significant change in C_{visc} or C_d. It is therefore allowable to simply rescale the throat width w_{throat} to satisfy Equation 3.108. The small change in the throat Reynold's number Re_t is validated in Section 4.2.5, and shown in Figures 4.3 & 4.4.

From all this follows that, as long the required mass flow is maintained by adhering to Equation 3.108, the nozzle behaviour and overall thruster performance ($\dot{m}$, I_{sp}, F) does not change in any significant way. This results in a meaningful comparison between designs. If the Reynold's number in the throat had drastically changed, even if no loss/quality factors are included in the model, then the correction would just be mathematical in nature, with limited physical significance.

In summary, it is acceptable to scale the width w_{throat} linearly with the total pressure loss Δp_{loss} from Equation 3.88 (as the channel depth d_c remains constant).

$$w_{\text{throat}_{\text{new}}} = w_{\text{throat}_{\text{old}}} \frac{p_{\text{in}}}{p_{\text{in}} - \Delta p_{\text{loss}}} \tag{3.110}$$

In Section 3.6.1 the effect on the overall nozzle and chip geometry is explained.

3.6. Geometry/structure

This section focuses on how final chip area A_{chip} relates to the channel design. This is important because the actual geometry of the chip is a large factor in determining the heat losses. Ultimately, it is the heat loss that one would like to minimize.

$$A_{\text{chip}} = l_{\text{chip}} w_{\text{chip}} \tag{3.111}$$

Calculating the chip area is simple, but the total chip length l_{chip} and w_{chip} are slightly more cumbersome. Sometimes, the result requires one to check if structural margins around the nozzle or channels are adhered to.

The chip length and chip width are build up as follows:

$$l_{\text{chip}} = l_{\text{inlet}} + l_c + l_{\text{outlet}} + l_{\text{nozzle}} \tag{3.112}$$

$$w_{\text{chip}} = 2w_{\text{margin}} + \max \begin{cases} w_{\text{inlet}} \\ w_{\text{outlet}} \\ w_{\text{nozzle exit}} \end{cases} \tag{3.113}$$

Figure 3.6 shows how the given dimensions are defined in the case of parallel rectangular channels. It must be noted that for different channel geometries, all equations in this chapter are also valid for serpentine channels or other translation symmetric geometries, as long as the multiple channels are spaced regularly with constant dimensions. The channel length l_c is always the result of Eq. 3.1 of the heat transfer model.

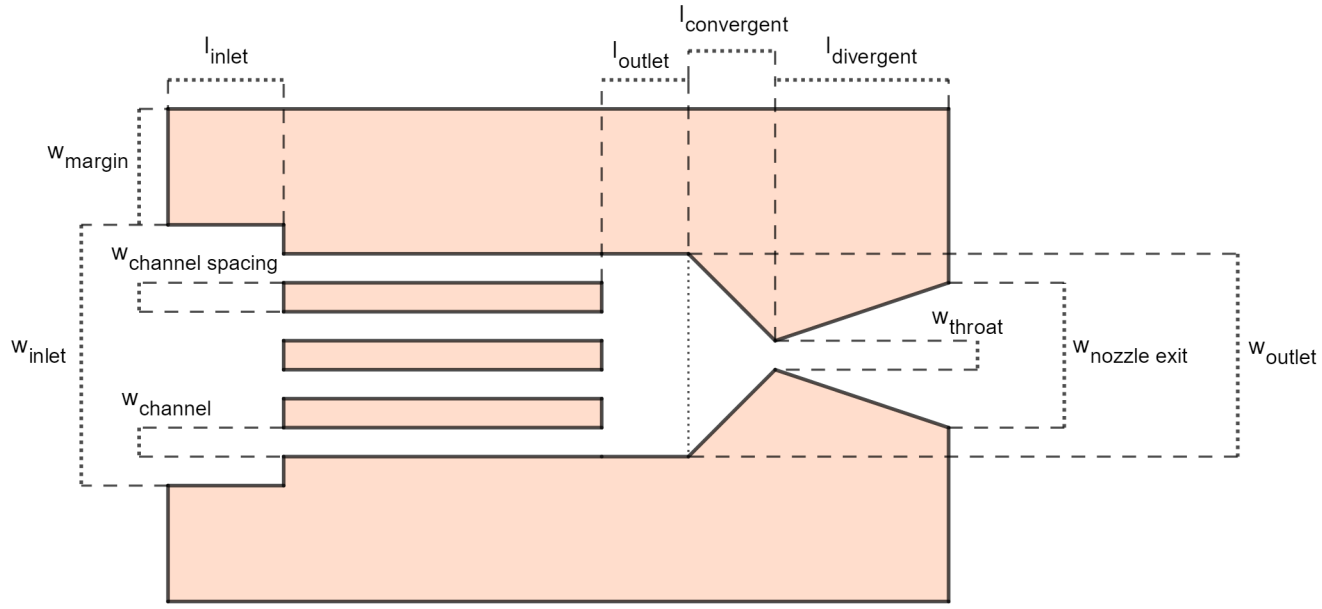

Figure 3.6: Drawing of heating chamber and nozzle geometry

3.6.1. Nozzle dimensions

The nozzle dimensions are of great importance, as its effect on the chip area A_{chip} has a great effect on heat losses. The effect of the pressure drop on the nozzle dimensions is explained in Section 3.5.4.

The nozzle is a 2D-conical nozzle with constant channel depth, and consists of a convergent and divergent part with respectively the lengths $l_{\text{convergent}}$ & $l_{\text{divergent}}$ (Eq. 3.114). All relevant dimensions and angles are shown in Figure 3.7.

The convergent nozzle length, depends on the throat width w_{throat}, the outlet manifold width w_{outlet}, and the convergent half-angle $\alpha_{\text{convergent}}$. For the divergent nozzle length, the exit rea ratio $\frac{A_e}{A_t}$, and the divergent half angle $\alpha_{\text{divergent}}$.

$$l_{\text{nozzle}} = l_{\text{convergent}} + l_{\text{divergent}} \tag{3.114}$$

$$l_{\text{convergent}} = \frac{w_{\text{outlet}}}{2\tan\alpha_{\text{convergent}}}\left(1 - \frac{w_{\text{throat}}}{w_{\text{outlet}}}\right) \tag{3.115}$$

$$l_{\text{divergent}} = \frac{\frac{A_e}{A_t}w_{\text{throat}}}{2\tan\alpha_{\text{divergent}}}\left[1 - \left(\frac{A_e}{A_t}\right)^{-1}\right] \tag{3.116}$$

The half-angles are fixed in this research. See Table 2.5.

3.6.2. Inlet/outlet manifold

VLM have a inlet manifold of a certain length, with the purpose of allowing time and space for the fluid to divide equally over the channels. No mention is made about why certain dimensions are chosen. It makes sense that the required length for proper division of fluid is related to the total width of the channels (and a margin), and a linear relation is assumed.

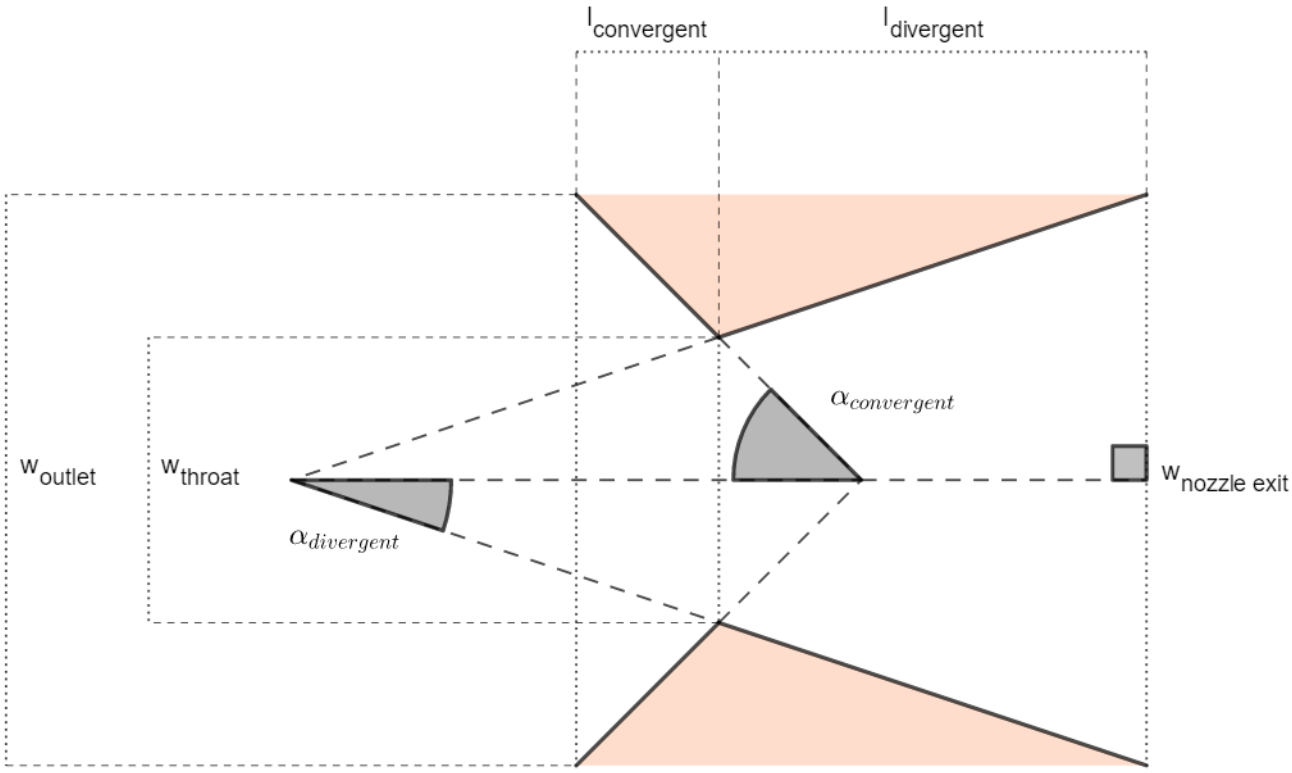

Figure 3.7: Detail view of nozzle geometry

$$l_{\text{inlet}} = \beta_{\text{inlet}} w_{\text{inlet}} \tag{3.117}$$
$$w_{\text{inlet}} = N_c w_c + (N_c - 1) s_c + 2 w_{\text{inlet,margin}} \tag{3.118}$$
$$w_{\text{inlet,margin}} = \beta_{\text{inlet,margin}} w_c \tag{3.119}$$

The design of Cen and Xu is chosen to inform the values for the margins, because it has been shown to work with acceptable quality factors. For this design $\beta_{\text{inlet,margin}} = 5.5$ and $\beta_{\text{inlet}} = 2$.

Whilst an outlet length and margin width are implemented in a similar way to the inlet dimensions by Eq. 3.121, the margin $w_{\text{outlet,margin}}$ and β_{outlet} were both zero for pre-existing VLM design, and also zero in this research.

$$l_{\text{outlet}} = \beta_{\text{outlet}} w_{\text{outlet}} \tag{3.120}$$
$$w_{\text{outlet}} = N_c w_c + (N_c - 1) s_c + 2 w_{\text{outlet,margin}} \tag{3.121}$$
$$\tag{3.122}$$

3.7. Heat loss

Roughly speaking, there are three ways to lose heat: convection, conduction and radiation. Convection is neglected for this research, as the thruster design is optimized for vacuum conditions. Radiation was the main focus of the heat loss model, as the different temperatures of the top and bottom of the chip, as modelled in Section 3.4.5, has quite the impact on the heat loss. Temperature-dependent conduction losses through the chip mounting also play a role. But within the time constraints of the research they have not been implemented. The limitations of this are discussed in Section 5.5.

3.7.1. Radiation

VLM are ultimately expected to operate in a vacuum, so convective losses should play no role in actual operating conditions. Although radiation losses are wave-length dependent, thermal losses are mostly

modelled by an experimentally determined emissivity ε of a material. This is then multiplied with the Stefan-Boltzmann law for black-body radiation, as shown in Equation 3.123. T_s is the temperature of the area A that radiates away heat.

$$P_{\text{rad}} = \varepsilon \sigma {T_s}^4 A \tag{3.123}$$

VLM are mostly flat, with the chip/PCB thickness 10-100 times smaller than chip lengths and widths, and can be neglected compared to the top of the chip surface/bottom of the Printed Circuit Board (PCB). So, the top of the chip surface/PCB, and the bottom of the PCB can be expected to represent the most heat loss.

The values for emissivity of silicon can be dependent on temperature, depending on the doping (as seen in Appendix D.1). However, at about 700 K it is about for both cases $\varepsilon = 0.7$.

The bottom of the PCB is a more special case for radiation, as first the heat must be conducted to the PCB, and therefore the conduction from the top to the bottom of the PCB, the conduction "sideways" out of the PCB to connected structures and the final radiation must be in equilibrium. Ignoring conduction to connected structures for simplicity, the heat loss can be found by equating the conductive heat transfer and the radiation loss with Equation 3.124:

$$\begin{aligned} q_{cond} &= q_{\text{rad}} \\ \frac{k_{\text{PCB}}(T_{\text{top}} - T_{\text{bottom}})}{t_{\text{PCB}}} &= \varepsilon_{\text{PCB}} \sigma T_{\text{bottom}}^4 \end{aligned} \tag{3.124}$$

This equation is solved for the temperature T_{bottom} at the bottom of the PCB surface. The top temperature is set to chip temperature, which is approximately the wall temperature $T_{\text{top}} = T_{\text{w}}$.

However, a clear value for the emissivity and conductivity of the PCB could not be found within the time-frame of the research. The material from which heat is radiated is therefore also assumed to be silicon. The thermal conductivity of silicon is quite high, so the silicon has no substantial insulating effect at the small wall thicknesses (100 micron or lower) considered.

The difference in temperature was very small, resulting in no significant reduction in radiation losses due to insulation. This was mostly due to the thin PCB. For this reason, the insulation is neglected, and the radiation from the bottom wall is simply calculated with the bottom wall temperature T_{bw} from Section 3.4.5.

4

Verification and Validation

In this chapter the implementation of the model from Chapter 3 and the design tool from Section 2.4.2 will be verified and validated.

Section 4.1 on verification explains how it was checked that the program indeed functions as intended (i.e.: implemented equations work as intended). Section 4.2 on validation compares the results from the model with real-world data, and validates if the optimization algorithm in the design tool indeed works as intended.

4.1. Verification

As validation data for the overall results of the model were scarce, an extra thorough verification effort was performed on the model. Whilst it is not substitute for a complete validation, it is expected that following strategy will mitigate this issue:

- Verify that libraries/functions providing physical/thermodynamic data are correctly reproducing well-established tabulated data.
- Verify that basic low-level functions are correctly implemented (i.e.: those stemming from physical law)
- Verify that applied empirical functions are correctly implemented (e.g..: Nusselt number relations)
- Verify at each step of integration, that functions in the previous three steps are correctly implemented.

All the above functions and libraries have been validated to various extents through scientific research. The first set of functions, which simply provide data about materials, propellants and physical constants are very well established, and only in rare edge cases break down. The second set of functions are very well researched, and definitely correct, as long as necessary assumptions hold and the physical description of the system is correct(e.g.: calculation of power needed to heat propellant to certain temperature or the radiation from a surface).

The data from the first step verifies that well established physical constants and values only affect the end calculation by the uncertainty of the experiments establishing them. Examples of these constants and values are the Stefan-Boltzmann constant σ, or the density of water at 5 bar, and 500K. This ensures that no errors are introduced by inputting wrongful data. In practice, all but a few values are so precise that their uncertainty does not affect the end result in any meaningful way. The values with larger uncertainty are discussed in Appendix B. After verification, the used values can be considered valid by virtue of the scientific research establishing these values.

The second and third step verifies that the implementation of physical laws and empirical relations is correct. Physical laws, such as basic radiation laws, cannot be expected to introduce any errors themselves. Instead, errors can only be introduced through incorrect application. The same holds true for empirical relations, except that the inaccuracies of the relations themselves are also introduced

into the model. Both type of errors cannot be solved by verification. Instead these errors must be determined through validation.

The last step verifies that the integration of all the functions in the above three steps happens correctly and no unnecessary errors are introduced at this point. An example of such integration test is found in Appendix B. For the overall integration test of the heat transfer model and pressure drop a manual test case was constructed in Microsoft Excel. In this case each channel phase was split into 3 sections. In this manner it was easy to verify that all calculations performed as intended and that the integration happened correctly. The only deviation between the manual case and the program was caused by differences in the source of thermodynamic parameters[1].

All steps are implemented through the method of automated tests. The extent of the unit tests can be checked by opening *"./htmlcov/index.html"* in the code repository. It is an automatically-generated webpage that shows which parts of the code are reached by unit tests[2]. Most(85%) of the code is reached by the unit tests, but not all unreached code was ultimately used in the program. Some of it was used for reporting purposes, or to do quick calculations.

4.2. Validation

The goal of the validation is to determine whether the models used for heat transfer can be used to predict both the power consumption, and heating chamber outlet conditions with sufficient accuracy to determine overall high-level Vaporizing Liquid Micro-thruster (VLM) performance.

In the next Section 4.2.1 the lack of complete data for validation is discussed, as well as what is done to remedy this issue as well as possible. In Sections 4.2.2 and 4.2.3 the model is applied to the design of the existing thrusters presented in Section 2.2.6. This is followed by checking if the flow similarity parameters of the found optimal solutions coincide with the range of validity of the heat transfer relations presented in Section 3.2. Lastly, in Section 4.2.6 the robustness of the optimization algorithm is checked, to validate if it finds the global optimum.

4.2.1. Challenges with validation data

At the time of writing, identifying data sets, that are complete enough to validate the model well enough to quantitatively assess the accuracy of heat transfer models was difficult. This was due to lack of the chamber temperature and the wall temperature being combined in the data set. For future research work and improvement of heat transfer models it is vital that both temperatures are measured, and that the field of micro-channel two-phase flow literature is monitored for new data sets relevant to VLM. The data sets used are:

- Multiple tests on the identical thruster from Cen and Xu, with the highest wall temperature($T_w = 573.15$ K), and the inlet pressure p_{in} ranging from 1.28 bar to 2.52 bar[13].
- Thruster #5 from Silva et al.[11].

This issue with validation data is mitigated by checking a possible range of temperatures to predict the heat transfer. At the very least it allows for establishing whether the used heat transfer relations are "not necessarily wrong". When chamber temperature data is lacking, the model is not necessarily wrong if:

- The model comes close or precisely predicts the channel length for at least some range of temperatures
- If the channel length vs. chamber temperature predictions vary as expected as the input changes (e.g.: increased mass flow results in lower chamber temperature for the same channel length)
- The predicted chamber temperature for a given channel length at least believably predicts the actual thrust according to Ideal Rocket Theory (IRT)

[1] Example calculation cases included in code repository.

[2] The report was automatically generated by 'Coverage.py' python package. See `https://coverage.readthedocs.io/en/coverage-5.3/` for the documentation.

The only way to increase the quality of the validation, is if this unknown chamber temperature is fed into an IRT model with sufficiently accurate corrections for real nozzle behaviour. If the resulting chamber temperature would then, together with nozzle geometry data, accurately predict thrust, mass flow and specific impulse, one could gain more confidence in the validity of the heat transfer model for VLM. Even though some attempts have been made to apply and validate these IRT corrections by Versteeg and Makhan[20, 21] , they are not yet accurate enough for this purpose. Makhan noted that his used empirical relation for viscous loss C_{visc}(see Eq. C.8) in the nozzle poorly predicted performance for throat Reynold's numbers below $\text{Re}_t < 2000$[20]. So, the justification for the weak validation is that within the scope of this research, no methods have been identified to improve it.

In addition to the above problem, the data from Silva et al. has a slight inconsistency, as the reported chamber temperature and full vaporization does not fit with the saturation temperature. The temperature deviates by less than 0.5 degrees. This can, however, be explained by measurement uncertainty(see Section 2.2.6) or very small pressure drops. The *inlet* pressure data is only reported with 0.1 bar precision, and acceleration through evaporation also already gives a pressure drop. It is, therefore, possible that the temperature is correct. For the purpose of the validation, with the no pressure drop assumption, the chamber temperature is increased by 0.5 K, to achieve full evaporation, with only a small impact on the resulting chamber temperature.

4.2.2. Comparison to data from Cen and Xu

Despite all available validation data being incomplete, the great advantage of the data of Cen and Xu is that the wall temperature is well known. This is because the chip was attached to a copper block, which can be expected to have plenty of thermal capacity to stay at near-constant temperatures. The other advantage is that, since it is the wall temperature that is known, and full vaporization has been reported, the possible range of resulting chamber temperatures can be restricted from the saturation temperature T_{sat} to the wall temperature T_{w}.

From the available relations the following were used:

- Single-phase gas and liquid: Equation 3.45 for fully developed laminar flow for a square channel with constant wall temperature.
- Two-phase: Nucleate boiling relations(3.54) and dry-out equations from Section 3.4.1 and 3.4.3.

These relations were used to calculate the resultant channel length, when the entire range of chamber temperatures was provided to the model. The result of this is shown in Figure 4.1. The red line in the figure is the actual length of 6 mm.

The model behaves as expected with the predicted channel length shifting up as the mass flow increases, as more power must be delivered to the fluid. The temperatures for which the correct length is predicted are tabulated below in Table 4.1, together with their IRT prediction, and quality factors. The chamber pressure for IRT is assumed to be the measured average inlet pressure ($p_c = p_{\text{in}}$).

Table 4.1: IRT predictions from Cen and Xu's thruster data, and calculated chamber temperature

Chamber conditions			**IRT prediction**			**Experimental**			**Quality factors**		
p_c [bar]	T_c [K]	γ [-]	F [mN]	I_{sp} [s]	$\dot{m}$ [mg·s^{-1}]	F	I_{sp}	$\dot{m}$	ζ_F [-]	$\zeta_{I_{sp}}$ [-]	C_d [-]
1.28	571.90	1.3039	3.92	133.5	3.00	2.3	100.7	2.33	0.59	0.75	0.78
1.52	570.80	1.3048	4.65	133.2	3.56	3.0	102.0	3.00	0.65	0.77	0.84
1.80	568.86	1.3059	5.51	133.0	4.23	3.8	105.9	3.66	0.69	0.80	0.87
2.08	565.95	1.3072	6.37	132.5	4.90	4.5	106.0	4.33	0.71	0.80	0.88
2.28	562.22	1.3085	6.97	132.0	5.39	5.2	106.1	5.00	0.75	0.80	0.93
2.52	557.80	1.3100	7.71	131.4	5.98	5.7	102.7	5.66	0.74	0.78	0.95

Nozzle parameters: $A_t = 0.018\text{mm}^2$; $\frac{A_e}{A_t} = 11.72$; $p_a = 0$; $p_c = p_{\text{in}}$; *Propellant*: water
Chamber temperature T_c calculated from 1D-model with $T_w = 573.15$ K, and channel length $l_c = 6$ mm
Inlet pressure p_{in} measured in experiment

The experimental performance is compared with the ideal performance with quality and correction factors (see Eq. 2.10-2.12 in Section 2.2.1).

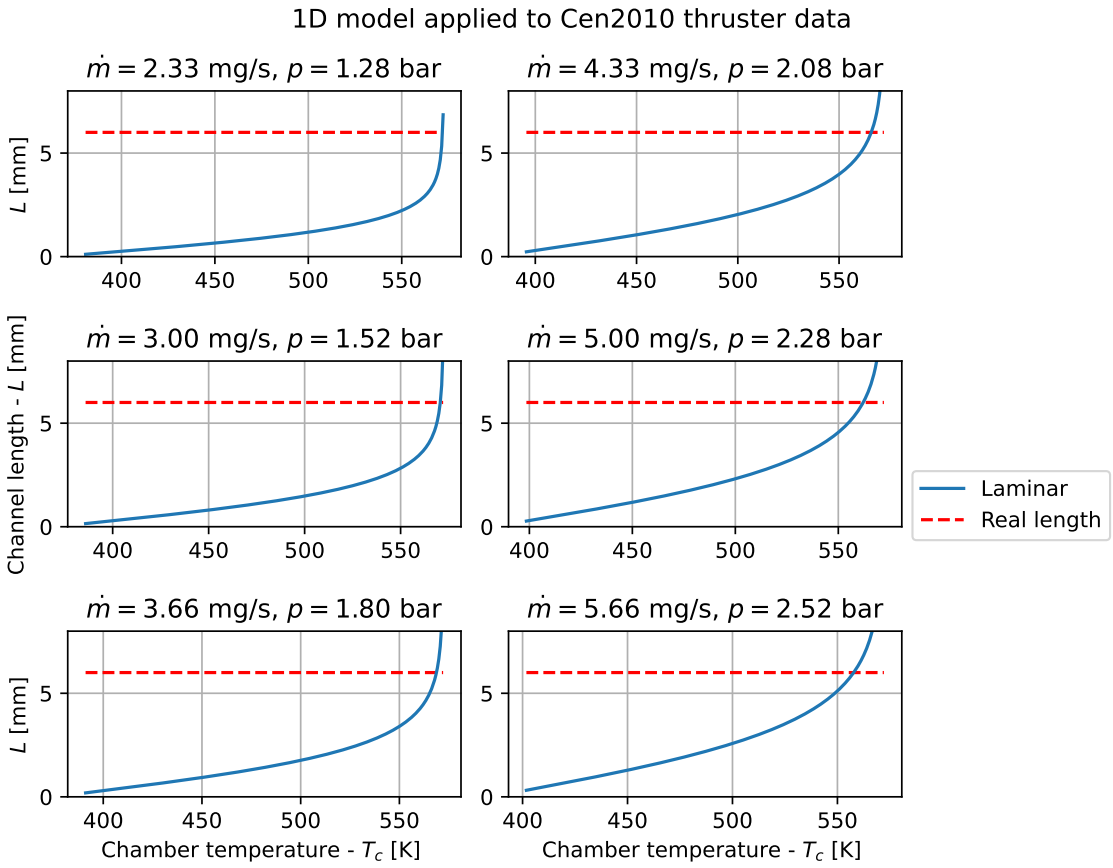

Figure 4.1: Heat transfer model applied to Cen and Xu's thruster under various operating conditions.

The calculated quality factors are ordinary results for VLM. The reported discharge factor C_d behaves as predicted, and increases with pressure. This fits with the calculations that the pressure drop stays relatively constant with pressure, and the impact of pressure drop therefore diminishes as the pressure increases(Figure E.1 shows that this is the case for this thruster[13]). In addition, the boundary layer in the throat shrinks with higher pressures, and lower temperatures.

Efficiencies of specific impulse I_{sp} of about 80% are also no unexpected result, and this values is in the range expected by Sutton[15]. Together with the discharge factor, the overall result makes sense for this thruster. The calculated chamber temperatures could therefore be correct, but it is hard to prove that they are with the limited data. In general, the quality factors $\zeta_F, \zeta_{I_{sp}}, C_d$ all being smaller than one, are an indication the calculation is correct. It is very unlikely that one outperforms the ideal calculations. But in this case, this is very weak support of the chamber temperature T_c being correct, as the quality factors would also have been below 1, if the wall temperature of $T_w = 573.13$ K would have been used.

Within the scope of this research, it can be concluded that the implemented 1D-model and the combined set of heat transfer relations for *laminar* flow, nucleate boiling, and dry-out, and single-phase liquid/gas flow are likely to be applicable for calculating the heat transfer for VLM optimization. In practice, this means that resulting combination of channel length l_c and temperature T_c for a given channel geometry, mass flow and inlet pressure are usable for VLM optimization purposes. However, with the current data, no accuracy can be quantified. This limits the ability to validate the model with respect to the required accuracies in the Top-Level Requirements (TLR).

4.2.3. Comparison to data from Silva et al.

The same approach to validation was done for the thruster #5 from Silva et al.[11]. In their work no wall temperature was known, so this is the unknown variable. In Figure 4.2 one can see that the same set of relations predicts the channel length l_c of 14 mm at a wall temperature T_w of 424.6 K. This is

only marginally above the chamber temperature T_c of 423.5 K. Note that the chamber temperature was already artificially raised to force the propellant to be liquid in the model (see Section 2.2.6 on the measurement uncertainty in this work). The uncertainty on the chamber temperature was 4 K.

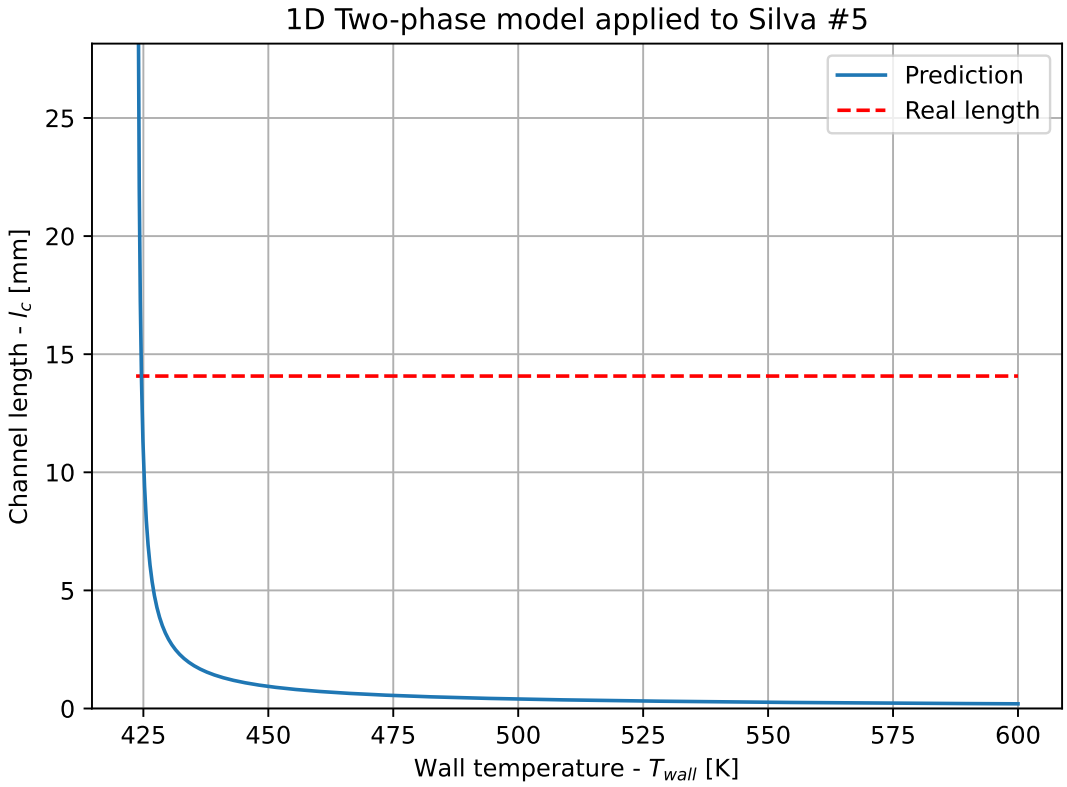

Figure 4.2: 1D Two-phase model applied to Silva et al.'s thruster

There were also no thrust measurements on this work, which makes it impossible to compare an IRT prediction with the actual result. On top of this, the wall temperature is so close to the chamber temperature, it might just be a 'solution' due to the asymptomatic behaviour of the heat transfer Equation 3.17. This ensures there is always a "right" channel length, as long as one assumes a low enough wall temperature.

However, the behaviour is very similar to the low mass flow $\dot{m} = 2.33$ mg·s^{-1} case in Figure 4.1. In addition, the mass flux and Reynold's number for Silva et al.'s thruster are about 25 and 10 times lower, respectively, than the low mass flow case of Cen and Xu. It therefore makes sense that the wall temperature and final chamber temperature lie even closer than in that case.

The only conclusion that can therefore be drawn is that the result is at least consistent with respect to the comparison to the thruster of Cen and Xu. With no other more complete and relevant data sets available, the possibilities to better validate the heat transfer model *directly* are exhausted. The heat transfer relations were, however, based on experimental data. Indirectly, validation can be further expanded by checking if the flow similarity parameters established in Table 2.4 are correct. This is done in Section 4.2.5.

4.2.4. Mist flow

In Section 3.4.4 it was mentioned that it was unclear how the heat transfer behaves after dry-out, and that there are no models to predict this behaviour for micro-channel flow. Still, a heat transfer model was necessary to bridge the gap between nucleate boiling and heating a fully vapourised flow. However, with the current data it is impossible to say anything of value about mist flow specifically, as only the model in its entirety can be validated. As became clear in the previous sections, this task was already impossible to do in a quantitative manner.

For future work it is therefore recommended that this assumption is investigated, but this should only be a high priority if the flow entering the nozzle turns out to not be fully vapourised *and* this significantly impacts nozzle performance. The effect of the mist flow assumption is only that at very high qualities (close to 1) the heat transfer function is continuously and smoothly connected to the Nusselt relation for heat transfer in the gas phase. There are no indications that heat transfer mechanisms exist at these high qualities that would result in discontinuous behaviour around the transition towards full gas flow. Neither have experiments indicated this type of behaviour suddenly arises in micro-channels. After all in Section 3.4.3 on dry-out qualities, it seems more likely that all micro-channels tend to dry-out completely, based on the trend of dry-out relations for larger channels.

The author is therefore of the *opinion* that investigating this part of the heat transfer is only important if:

- It turns out full vaporisation is not achieved, or if nozzle behaviour cannot be explained if the nozzle inlet conditions have a vapour quality $x = 1$
- Experiments in micro-channel literature show new behaviour at high-quality flow boiling.

Absent indications of discontinuous/non-smooth behaviour of the heat transfer at high-qualities, it is hard to imagine how the result is impacted in a significant extent by another heat transfer model that is also continuous and smooth.

4.2.5. Assumed flow similarity parameters

Before starting the optimization, one must first set the applicable relations for pressure drops and heat transfer. These are the relations presented in Section 3.5 and 3.2 respectively. The applicability depends mostly on the Reynold's number Re in various sections of the channels. The optimizer could steer the design towards different flow regimes, so the resulting design must be shown to be consistent with the chosen relations. Inconsistency would be a sign of invalid results.

The largest factors influencing the Reynold's number are the dimensions of the channel, the mass flow, phase of the flow and the propellant. The mass flow in a single channel is in turn mostly affected by the selected thrust F, the number of channels N_c, and the chamber temperature T_c. In Figures 4.3 and 4.4, the effect of those parameters on Re will be shown. The red dashed lines show the location where the optima were found, and they correspond with the cases presented in Section 5.1.1 and Section 5.1.2, where the full results are presented. The red dotted lines are at the location where the resulting power loss was first 5% larger than at the optimum.

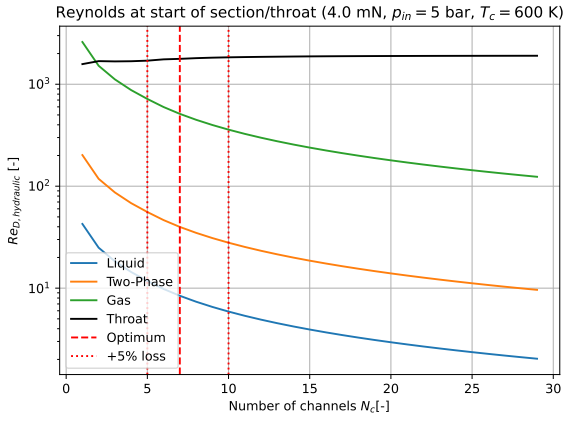

Figure 4.3: Reynold's number Re for $F = 4mN; T_c = 600K$ resulting in $\dot{m} = 3.018$ mg·s^{-1}

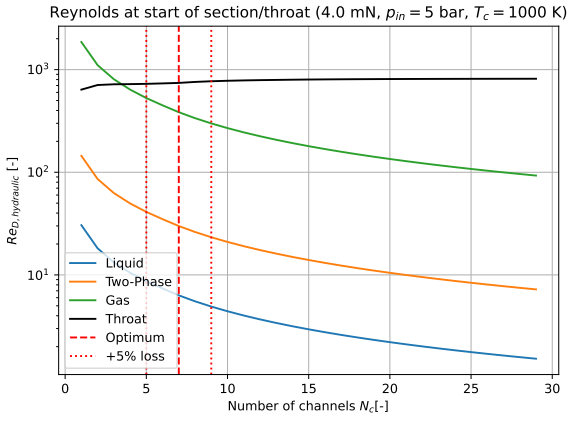

Figure 4.4: Reynold's number Re for $F = 4mN; T_c = 1000K$ resulting in $\dot{m} = 2.266$ mg·s^{-1}

In the plots Re is determined at the start of each section(right after the phase-change). In Figure 4.3 for $F = 4mN$ and $T_c = 600K$ it is about 8, 40 and 512 for the liquid, two-phase, and gas phase respectively. The Reynold's number for the two-phase flow is equal to Re_{le}, which is the Reynold's number as if the flow where entirely liquid(see Equation 3.53). In Figure 4.4, when $F = 4$ mN and $T_c = 1000$ K the Reynold's numbers are 6, 30 and 385 for the 3 phases. Clearly the results at and around the optimum are well into the assumed laminar flow range.

However, the assumption was that the flow would be *fully developed laminar flow*, which is when the channel is much longer than the hydrodynamic entrance length. X_T. Inspection of the channel lengths of each respective phase, shows that this assumption is violated, as the channel sections are almost as long as the hydrodynamic entrance length(as calculated with Eq. 3.49). This can be seen for $F = 4mN$ and $T_c = 1000K$ in Figure 4.5 and 4.6 for liquid and gas phase respectively. The resulting plots look similar for other chamber temperatures.

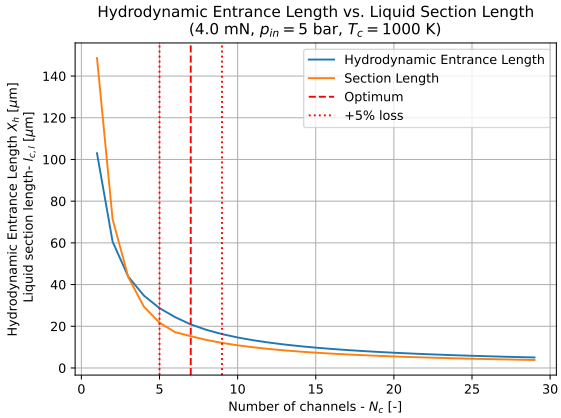

Figure 4.5: Hydrodynamic entrance length (liquid phase) X_T for $F = 4mN; T_c = 1000K$ resulting in $\dot{m} = 2.266$ mg·s^{-1}

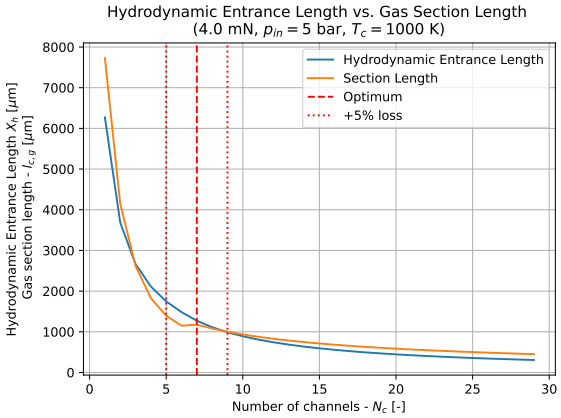

Figure 4.6: Hydrodynamic entrance length (gas phase) X_T for $F = 4mN; T_c = 1000K$ resulting in $\dot{m} = 2.266$ mg·s^{-1}

This means that the flow is actually *thermally developing flow*, which is expected to enhance the heat transfer. Using relations for thermally developing flow would thus predict shorter channel lengths. Recently Su et al. published a paper on this type of flow in rectangular micro-channels. Their research includes the effect of the aspect ratio of the channels on the heat transfer. It is recommended that for future work, their newly proposed heat transfer correlations are implemented when optimizing VLM heating chamber designs[40].

Another important result is that the Reynold's number at the throat stays relatively constant with the pressure drop (and thus chamber pressure), especially around the optimum. This can be seen in Figures 4.7 & 4.8. For $F = 4mN$, the throat Reynold's numbers for the throat Re_t at the optimal solutions are respectively 1803 and 759. Within the bounds around the optimal solution the ranges are $1754 - 1848 (-2.7\% - +2.5\%)$ and $734 - 779 (-3.3\% - +2.6\%)$. The bounds (red dotted lines indicate the solutions where the power loss is about 5% worse).

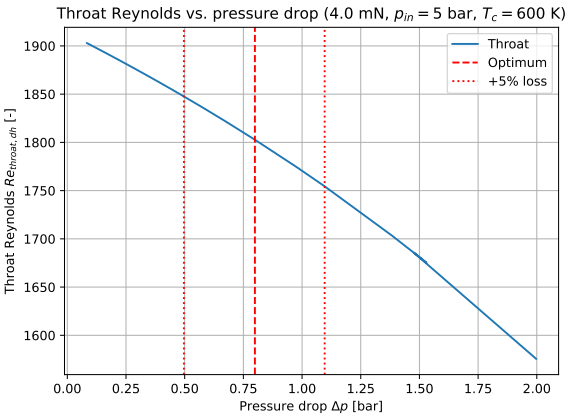

Figure 4.7: Re_t vs. Δp for $F = 4mN; T_c = 600K$ resulting in $\dot{m} = 3.018$ mg·s^{-1}

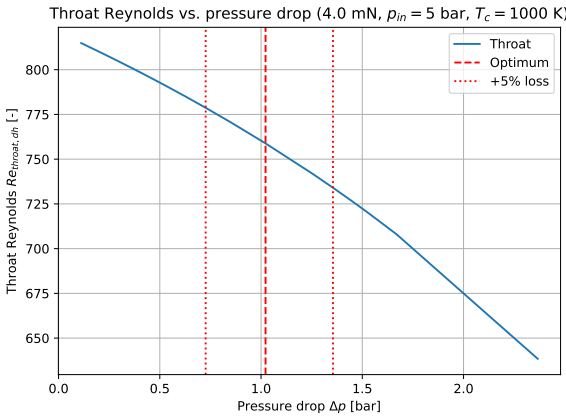

Figure 4.8: Re_t vs. Δp for $F = 4mN; T_c = 1000K$ resulting in$\dot{m} = 2.266$ mg·s^{-1}

This validates the assumption made in Section 3.5.4 that the throat can simply be linearly rescaled to maintain mass flow, due to very small variations in the Reynold's number. Especially the relative

change in Re_t results in even smaller relative changes in real nozzle performance parameters.

This validation also shows that it is possible to incorporate nozzle correction factors into the model at almost no computational cost. As long as the throat Reynold's number is estimated correctly for the given chamber temperature T_c and thrust F *before* the optimization, then a more accurate mass flow can be estimated with the uncorrected nozzle design. The nozzle can then again be linearly corrected with Equation 3.110. This improved mass flow calculation would greatly improve the total power consumption P_t results, as the bulk of the power consumption comes from vaporizing the propellant.

4.2.6. Robustness of optimization algorithm

To perform the optimization, "L-BFGS-B"[3] as implemented in SciPy was chosen. The algorithm, its settings, and the settings of the underlying model are described in Section 2.4.3. In theory, if there is just one local optimum, the algorithm performing a search, will find the global optimum by looking in the direction of steepest descent. The accuracy would then only be bounded by the desired accuracy for the solution (which is given by the programmer). Other settings of the algorithm would thus not matter.

In practice, there could be several optima, or even an infinite amount of optima, lying on a continuous line. The algorithm then could get stuck in a local optimum. These problems are exacerbated by numerical issues. The output function for power loss P_{loss} is in reality an continuous function of the input variables: channel width w_c, channel spacing s_c and top wall temperature T_{w}. But, because the simulation underlying the optimization has limited resolution, numerical artefacts may from time to time affect the calculation of (approximate) gradients, and affect the outcome of the optimization.

To validate that the optimization algorithm finds the correct outcome, and the true optimum, two checks for robustness are employed: single-variable variation, and a Monte-Carlo sensitivity analysis.

The single-variable variation checks if the power loss is indeed higher if any of the variables are varied, whilst other remain fixed. This helps to see if the algorithm did not stop prematurely, and partially checks if there is not another optimum anywhere else. In Figures 4.9 & 4.10 one can see what the resulting power loss P_{loss} would be if one moves *one* of the input variables away from the found solution. In all cases, the power loss clearly increases. It is an indication that the optimization algorithm estimates the gradient of the objective function properly. It gives some confidence that the solution is at the very least in a local optimum.

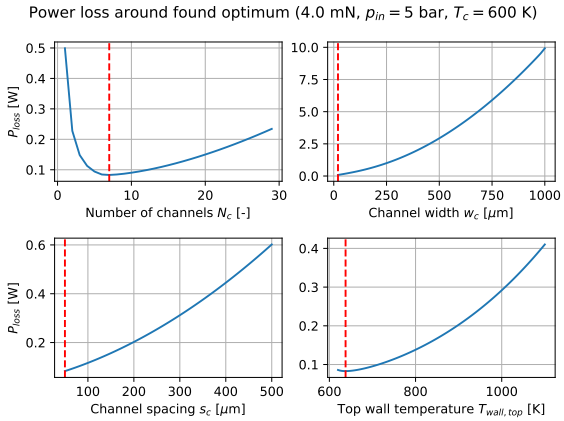

Figure 4.9: Re_t vs. Δp for $F = 4mN; T_c = 600K$ resulting in $\dot{m} = 3.018$ mg·s^{-1}

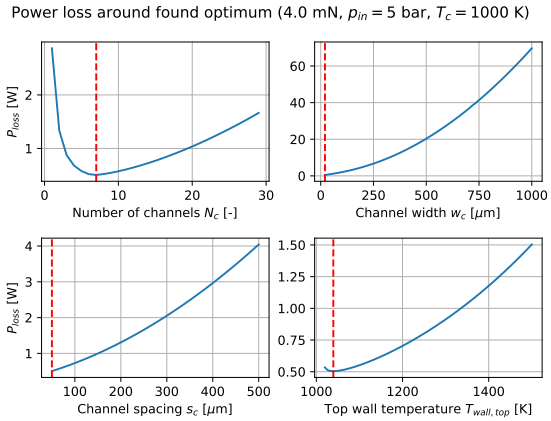

Figure 4.10: Re_t vs. Δp for $F = 4mN; T_c = 1000K$ resulting in$\dot{m} = 2.266$ mg·s^{-1}

To increase the confidence in this optimum being a global optimum, a Monte-Carlo analysis is performed. The optimization algorithm works by either taking the upper bounds of the design space as the initial guess, or by using the previous found optimum (for a different amount of channels) as the starting guess. In Figures 4.11 & 4.12 one can see what happens when random starting guesses are chosen.

For the case of $F = 4mN$ & $T_c = 600K$ none of the 250 guesses resulted in a power loss that differed more than 0.0001% from the optimum found with the regular algorithm. This is strong evidence that

[3]Short for "Limited Memory Broyden–Fletcher–Goldfarb–Shanno (Bounded)"

this optimum is indeed global.

For the case of $F = 4mN$ & $T_c = 1000K$ 15 of the 250 guesses resulted in a power loss that differed more than 0.0001% from the optimum found with the regular algorithm. These outcomes are indicated with a red cross. However, all these other found optima were *higher* than the one found by the regular algorithm. This is, again, strong evidence that the found optimum was indeed global. However, it also shows that at higher temperatures the algorithm is more prone to get stuck, especially if the initial guesses of channel width are very large. However, in Table 4.2 one can see that these solutions would stick out, and are obvious to the user of the software. This is because it would manifest as a sudden increase in power loss for just one or several number of channels[4]. In practice, with the regular algorithm, these problems did not occur after the settings for the algorithm were adjusted to work with the model employed in this research.

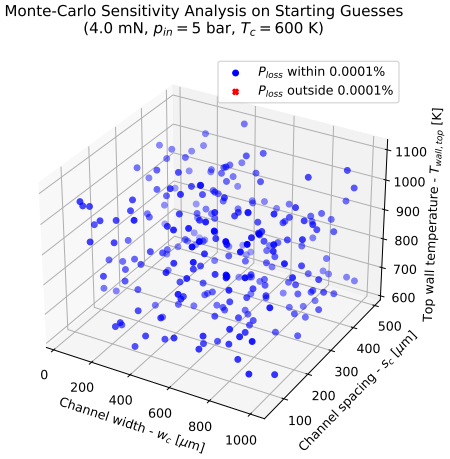

Figure 4.11: Re_t vs. Δp for $F = 4mN; T_c = 600K$ resulting in $\dot{m} = 3.018$ mg·s^{-1}

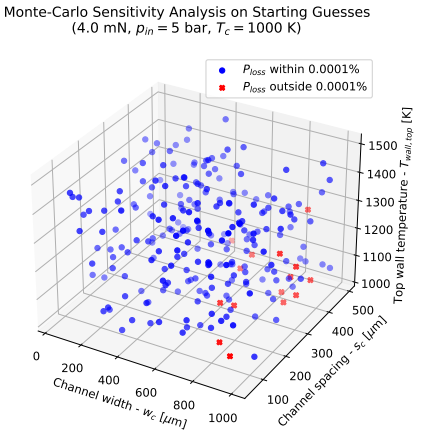

Figure 4.12: Re_t vs. Δp for $F = 4mN; T_c = 1000K$ resulting in$\dot{m} = 2.266$ mg·s^{-1}

Another important aspect of the Monte-Carlo analysis, is that it produces a distribution of the design parameters that results in the optimum value. This helps to assess whether there are multiple sets of design parameters that result in the same optimal value. Table 4.2 shows the minimum and maximum values of the distribution. For the $T_c = 1000K$ the distributions are split in the correct and incorrect solutions. It is clear that the correct solutions barely vary in terms of power loss, and the calculated solutions. In fact, one could argue that computational power is wasted to gain this accuracy, as this accuracy is clearly not required in the preliminary design phase. However, this accuracy is a by-product of the settings that were required to make the algorithm robust.

4.3. Conclusions

Extensive verification ensured that the model was implemented as intended, from the lowest level of the code, and the high level of full integration. However, the actual accuracy of the model depends on how well it reproduces actual experimental data from VLM. The best available was from the thruster experiments of Cen and Xu[13], but it did have not enough information to validate the heat transfer model on its own.

This was alleviated by finding the chamber temperature that predicted the actual channel length. This chamber temperature was used to predict the thruster performance based on IRT. This predicted performance was then compared to the measured performance. The determined quality factors in this comparison were realistic, and behaved as expected. Therefore this approach showed no indications that the heat transfer model, producing the input for IRT, was invalid. However, it is impossible to make stronger claims than stating that the model is “not necessarily wrong”.

Furthermore, a check was performed on the Reynold’s numbers Re in various parts of the flow. This

[4]In fact, reducing these jump discontinuities were used as a heuristic for robustness when altering the optimizer settings (with non-random starting guesses).

Table 4.2: Distribution of found solutions in Monte-Carlo Sensitivity Analysis

Correct optima for $\mathbf{F = 4mN; T_c = 600K}$				
	Minimum		*Maximum*	
Power loss P_{loss}	0.08295733	[W]	0.08295734	[W]
Channel width w_c	20.000000	[μm]	20.000000	[μm]
Channel spacing s_c	50.000000	[μm]	50.000000	[μm]
Top wall temperature T_{w}	637.59878	[K]	637.620772	[K]
Correct optima for $\mathbf{F = 4mN; T_c = 1000K}$				
	Minimum		*Maximum*	
Power loss P_{loss}	0.50500276	[W]	0.50500276	[W]
Channel width w_c	20.000000	[μm]	20.000000	[μm]
Channel spacing s_c	50.000000	[μm]	50.000000	[μm]
Top wall temperature T_{w}	1039.41871	[K]	1039.424928	[K]
Incorrect optima for $\mathbf{F = 4mN; T_c = 1000K}$				
	Minimum		*Maximum*	
Power loss P_{loss}	0.53085331	[W]	0.53153693	[W]
Channel width w_c	20.739854	[μm]	20.756560	[μm]
Channel spacing s_c	50.000000	[μm]	50.000000	[μm]
Top wall temperature T_{w}	1020.00285	[K]	1020.172601	[K]

showed that the range of possible heat transfer relations proposed in Section 3.2 was not sufficient. The resulting optima turned out to be deeper in the laminar flow range, i.e.: *thermally developing* instead of *fully developed* laminar flow. In future work, more applicable heat transfer relations must therefore be used in the model. Su et al. published research on heat transfer in thermally developing laminar flow in rectangular micro-channels with various aspect ratios[40], which could be applied in future research.

The check on Reynold's numbers in the throat Re_t also revealed that this value is very insensitive to the pressure drop and associated changes in the throat dimensions. Therefore, applying correction factors to the ideal prediction from IRT would have been possible.

Lastly, it was determined that optimization algorithm was robust and found global optima through varying single parameters around the found optima, and a Monte-Carlo analysis on starting guesses of the algorithm. In the Monte-Carlo analysis the algorithm sometimes found incorrect solutions with higher power losses. However, this behaviour did not occur in practical use of the tool.

5

Results

The results of the design tool are presented in two perspectives: first in Section 5.1 a detailed view of the optimal result for a given thrust F and chamber temperature T_c are given. These are not the top-level results, as required by the Top-Level Requirements (TLR). However, they provide the best insight into the workings of the tool, and how the design is optimized. Secondly, the results will be aggregated into the top-level result: curves of power consumption P_t vs. specific impulse I_{sp}, together with tables of the design parameters resulting in these optimal designs. These plots are the envisioned outcome of the design tool, as described in the Research Objective in Section 1.4.2.

After these main results, in Section 5.3 sensitivity analyses will be performed on design parameters and constraints that had a large effect on the optimal outcome. After the sensitivity analysis, the design tool is ran on a thruster designed, build and tested by Cen and Xu[13]. The differences in the design will be investigated in Section 5.4.

The, after stating the limitations on the results in Section 5.5, the main findings and recommendations will be presented in Section 5.6.

Lastly, the common baseline parameters are restated here in Table 5.1. The values are derived from the design space presented in Table 2.5 on page 22[1].

Table 5.1: Common baseline parameters and bounds on input

Parameter	**Value**	
Propellant	Water	
Specific heat ratio	*See Figure D.3*	
Inlet temperature - T_{in}	300	[K]
Inlet pressure - p_i	5	[bar]
Back pressure - p_a	0	[bar]
Exit area ratio - $\frac{A_e}{A_t}$	10	-
Nozzle divergent half-angle - $\alpha_{\text{divergent}}$	22.5	[deg]
Nozzle convergent half-angle - $\alpha_{\text{convergent}}$	45	[deg]
Bounds on input parameters		
Number of channels - N_c	[1-30]	[-]
Channel width - w_c	[20-5000]	[μm]
Channel spacing/wall thickness - s_c	[50-500]	[μm]
Top wall superheat - (T_{w}-T_c)	[1-500]	[K]

[1]The nozzle divergent half-angle $\alpha_{\text{divergent}}$ was set to 22.5 degrees in error instead of 30 degrees. For the purpose of this research, it is not very consequential, but the effect is briefly discussed in the Appendix E.2.

5.1. Optimal design for given thrust and chamber temperature

In this section a few optimized designs for given thrust and chamber temperature will be laid out to answer what chip geometry makes a specific design optimal. Recall from Section 2.4.3 on the optimization algorithm that for each integer in the range of allowed channel numbers an optimum power loss is determined. The cases will therefore be presented with the number of channels N_c on the x-axis. The optimal number of channels is indicated with a red dashed line, and the location where the power loss is first 5% higher than the optimum are indicated on with red dotted lines on either side.

Case 1 with $F = 4$ mN and $T_c = 600K$ in Section 5.1.1 will be the most detailed analysis of a case, as similar results for different cases will not be restated. Case 2 in Section 5.1.2 discusses the results for a Vaporizing Liquid Micro-thruster (VLM) with $F = 4$ mN and $T_c = 1000K$, where the effect of a different chamber temperature will be shown. Between the two cases, the mass flow $\dot{m}$ naturally varies as well, according to Ideal Rocket Theory (IRT). Finally in Section 5.1.3 Case 3 will vary on the previous two cases by having a lower thrust of 2 mN, together with a chamber temperature of 1000 K. This more significantly impacts the mass flow and the required throat width.

5.1.1. Case 1: 4 mN thrust and 600 K chamber temperature

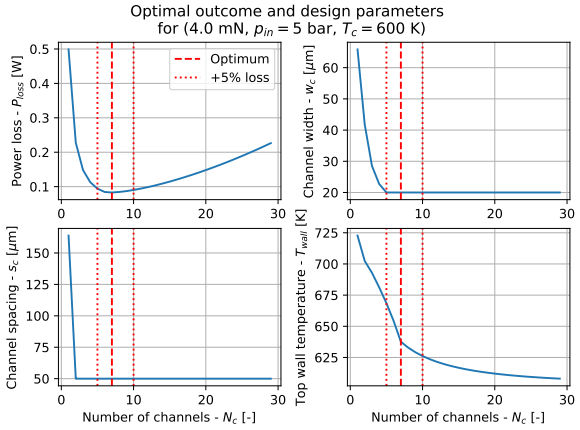

Figure 5.1: Optimal design for $F = 4$ mN; $T_c = 600$ K resulting in $\dot{m} = 3.018$ mg·s^{-1} and $I_{sp} = 135.1$ s

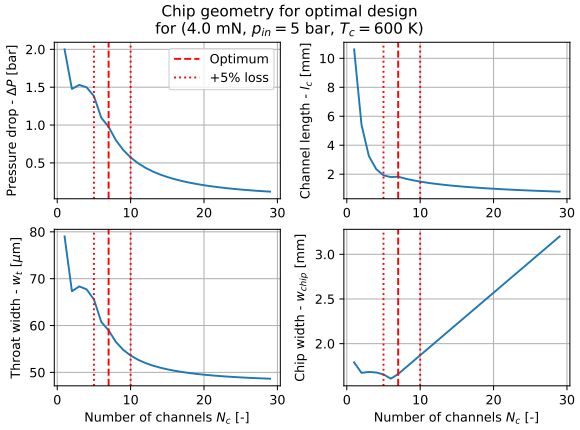

Figure 5.2: Optimal chip geometry for $F = 4$ mN; $T_c = 600$ K resulting in $\dot{m} = 3.018$ mg·s^{-1} and $I_{sp} = 135.1$ s

In Figure 5.1 the optimal outcome for the case of $F = 4$ mN and $T_c = 600$ K is presented. This case results in a **specific impulse** of $I_{sp} = 135.1$ s and a **mass flow** of $\dot{m} = 3.018$ mg·s^{-1}. The minimized power loss is $P_{\text{loss}} = 0.083$ W, together with an ideal power consumption $P_{\Delta h} = 9.076$ W resulting in **total power consumption** of $P_t = 9.158$ W. All the relevant values, comparing all three cases, are tabulated in Table 5.2.

The vertical red dashed line on each plot marks the value of the optimal solution. The lowest power loss occurs when the **number of channels** is $N_c = 7$. The vertical red dotted lines indicate the sensitivity of the solution to the number of channels. When the number of channels first results in +5% power loss or higher, a red dotted line is placed. In this case it occurs at 5 channels or lower, or 10 channels and higher. Below 5 channels the ideal power consumption rises steeply, and above it increases more gradually.

This trend also appears in the channel length l_c in the top right of Figure 5.2. For future designers of VLM this is an important result, as it indicates, that it is safer to design a chip with slightly more channels than is optimal. Referring back to Figure 4.9(bottom right) on 60, where the robustness of the algorithm was validated, it can be noted that top wall temperature can be increased in case a design fails to reach the desired temperature in experiments. This can be done with a relatively low increase in power loss. The optimal **top wall temperature** in this case is $T_{\text{w}} = 637.6$ K.

The penalty for producing a chip with too few channels(and too high a pressure drop), is however pretty steep. This is because a mismatch between channel length, number of channels, and the desired chamber temperature can according to this model not be alleviated with small changes in wall temperature. Also, the optimal channel width does not change with slightly more channels, again providing some safety that the designed chip would work optimally, even if it does not behave precisely as

expected.

Another result is that the optimal channel width w_c (top right of Figure 5.1) and channel spacing s_c (bottom left), lie precisely on the lower bound of the design space. These lower values were chosen when the design space was bounded in Table 2.5. Here it must be restated that these values were deemed to be manufacturing-limited in the case of the channel width w_c, and pressure-limited in case of the channel spacing/wall thickness s_c. Clearly, another lower optimal power consumption would be found if these limitations can be reduced. In Section 5.3 a sensitivity analysis on these lower bounds will be performed to inform manufacturers and designers about the potential benefits of doing so. From this can also be concluded, that if it is known that the optimal result will be constrained by the lower bound, the optimization can be simplified and sped up by simply setting those parameters to be constant.

Looking into more detail at the **channel spacing** s_c in Figure 5.1 one can see that, in contrast to the channel width w_c, it immediately lies on the lower bound (starting from 2 channels or higher). The higher value for 1 channel can be ignored, as the optimization algorithm returns an arbitrary value, as it finds out it has no effect on the objective function.

One potential explanation for this is that a smaller channel spacing reduces the bottom wall temperature T_{bw} of the chip. Whilst this reduces the effective heat transfer to the fluid, this could be offset by a reduced radiation loss, with the latter being more important. Analysis of the data shows that for all solutions the differences between top T_{w} and bottom T_{bw} wall temperature is minimal. It is never greater than 19 degrees, and the difference is about 14 degrees for the optimum. Looking at the fourth-power dependency of the radiation loss given by Equation 3.123, this slight difference would already result in 9% less power loss from the bottom of the chip as $1 - \left(\frac{600}{600-14}\right)^4 = 9\%$. This reduced heat loss is improved with minimal impact on the heat transfer, because that impact scales roughly in a linear fashion.

This immediately gives another explanation for this behaviour. If the effect of reducing the channel spacing on the heat transfer is so small, then reducing the channel spacing also makes the chip less wide. This reduces the radiation loss of the chip even further than the aforementioned benefit.

Turning again to the **channel width** w_c, one sees a different reason for this race to the bottom. First it must be noted that, unlike the channel spacing, the channel width is not *always* on the lower bound. Instead, for fewer channels, the optimal solution is to have a wider channel. This behaviour is dictated by the **pressure drop** Δp (top left of Figure 5.2), which is an important factor in determining the optimum. In this case, the pressure drop is $\Delta p = 0.98$ bar. Referring back to Section on all forms of pressure drops 3.5, it must be noted that the *accelerative* pressure drop is *not* included in this pressure drop, as it has no effect on the nozzle dimensions.

To explain this, one must look back at the effect of the pressure drop on the nozzle, and the effect of the nozzle size on the radiating chip area in Section 3.5.4 and 3.6, respectively. Smaller channels increase the flow velocity and enhance heat transfer per unit area. On the flip-side, the flow speeds up and the reduced wall area increases the channel length. The former increases the pressure drop quadratically, and the latter linearly. Both effects together, quickly drive up the pressure drop with small changes.

To maintain the mass flow through the nozzle, the throat width (and the entire nozzle) must scale up in size. At low channel numbers this increase in nozzle size increases the radiating area of the entire chip, as it becomes the widest element of the entire chip. At higher channel numbers, instead the pressure drop is low, and the chip width is determined by the combined size of all heating channels. The point at which the chip width w_{chip} changed from nozzle-dominated to channel-dominated can be seen in the bottom right of Figure 5.2. One can see the chip width gradually drops with the pressure, until after 6 channels it suddenly starts to increase linearly with number of channels, because all channels are 20 micron wide after this point.

Looking with this context at the **channel length** l_c at the top right of Figure 5.2 and the **top wall temperature** T_{w} in bottom right of Figure 5.1, it becomes more clear why the optimum lies close after the point of the closest chip width w_{chip} with 6 channels. Before this point, the optimization algorithm appears to reduce the impact of the pressure drop, by employing a higher wall temperature than at the optimum. Without this high temperature the channel would be even longer, and the pressure drop even worse. In turn the chip would be even wider. However, after this point the reason for drastically reducing the channel length suddenly disappears. The channel length therefore starts to decline gradually. At the same time, the chip width quickly starts growing, as it must due to the bounds set on channel width

and channel spacing in the design space. The chip is quickly becoming much wider, while the channel length barely decreases. When you take into account that the channel length is only a portion of the overall chip length l_{chip}, the chip area A_{chip} is growing quickly as well. The wall temperature follows the same behaviour as the channel length, and starts declining much slower. Everything taken together, increasing the channel length no longer results in lower radiation losses. The heating channel length at the optimum is $l_c = 1.82$ mm.

All these values, of course results in an overall chip design, and this design is presented in Table 5.2. The dimensions were defined earlier in Figure 3.6. Take note that the nozzle exit width $w_{\text{nozzle exit}}$ is only a bit smaller than the inlet manifold width w_{inlet} (590 vs. 660 micron).

Table 5.2: Overview of chip geometry for 3 separate cases

Performance				
	Case 1	*Case 2*	*Case 3*	
Thrust -F	4	4	2	[mN]
Chamber temperature -T_c	600	1000	1000	[mN]
Chamber pressure - p_c	5	5	5	[bar]
Specific heat ratio -γ	1.309	1.254	1.254	[-]
Specific impulse - I_{sp}	135.1	180.0	180.0	[s]
Mass flow - $\dot{m}$	3.018	2.266	1.133	[s]
Ideal power consumption - $P_{\Delta h}$	9.076	8.782	4.391	[W]
Power loss - P_{loss}	0.083	0.505	0.308	[W]
Total power consumption - P_t	9.158	9.287	4.700	[W]
Optimal input parameters				
	Case 1	*Case 2*	*Case 3*	
Number of channels - N_c	7	7	4	[-]
Channel width - w_c	20	20	20	[μm]
Channel spacing - s_c	50	50	50	[μm]
Top wall temperature - T_{w}	637.6	1039.4	1043.2	[K]
Resulting length dimensions				
	Case 1	*Case 2*	*Case 3*	
Inlet manifold length - l_{inlet}	1.320	1.320	0.9	[mm]
Heating channel length - l_c	1.826	1.227	1.042	[mm]
Convergent nozzle length - $l_{convergent}$	0.191	0.189	0.101	[mm]
Divergent nozzle length - $l_{divergent}$	0.641	0.677	0.311	[mm]
Total chip length - l_{chip}	3.977	3.413	2.354	[mm]
Resulting width dimensions				
	Case 1	*Case 2*	*Case 3*	
Inlet manifold width - w_{inlet}	660	660	450	[μm]
Total channel width	440	440	230	[μm]
Throat width - w_{throat}	59.0	62.3	28.6	[μm]
Nozzle exit width - $w_{nozzle\ exit}$	590	623	286	[μm]
Chip margin width - w_{margin}	0.5	0.5	0.5	[mm]
Total chip width - w_{chip}	1.660	1.660	1.450	[mm]
Total chip area - $\mathbf{A_{chip}}$	6.60	5.67	3.413	[mm^2]

5.1.2. Case 2: 4 mN thrust and 1000 K chamber temperature

In Figure 5.3 the optimal outcome for $F = 4$ mN and $T_c = 1000K$ is shown. This case results in a higher $I_{sp} = 180.0$ s and lower mass flow $\dot{m} = 2.266$ mg·s^{-1} than for Case 1. The minimized power loss is $P_{\text{loss}} = 0.505$ W, together with an ideal power consumption $P_{\Delta h} = 8.782$ W resulting in total power

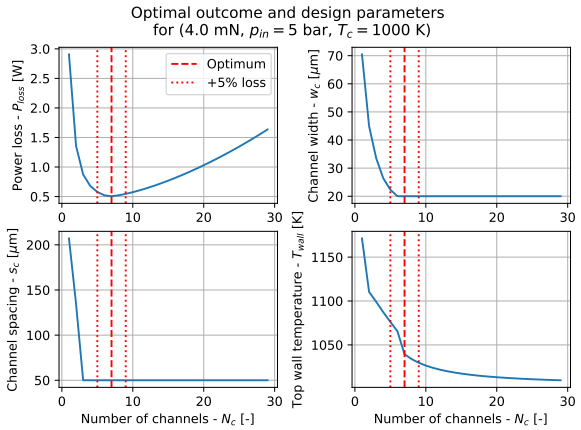

Figure 5.3: Optimal design for $F = 4$ mN; $T_c = 1000$ K resulting in $\dot{m} = 2.266$ mg·s^{-1} and $I_{sp} = 180.0$ s

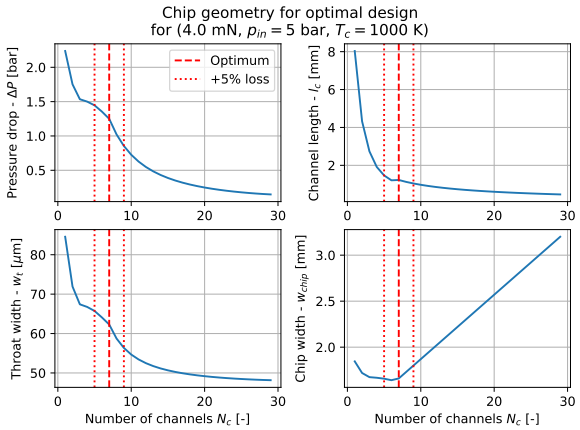

Figure 5.4: Optimal chip geometry for$F = 4$ mN; $T_c = 1000$ K resulting in $\dot{m} = 2.266$ mg·s^{-1} and $I_{sp} = 180.0$ s

consumption of $P_t = 9.287$ W. All the relevant values, comparing all three cases, are tabulated in Table 5.2.

Compared to Case 1, the power loss has increased with 0.422 W (or 6 times higher than 0.083 W). The difference in total power consumption is, however, only 0.129 W. This is easily explained by IRT, as the increased chamber temperature for the same thrust , results in a lower mass flow (see Eq. 2.2). Since most energy for heating the flow goes into vaporization, the ideal power consumption drops, despite the increased chamber temperature. In Section 5.2 this effect will be presented over the entire range from $T_c = 600$ K to $T_c = 1000$ K.

Similarly to Case 1, this optimum occurs at $N_c = 7$ **number of channels**, with the power loss first being +5% worse at 5 and 9 channels. The optimal **channel width** and **channel spacing** have also dropped to $w_c = 20$ and $s_c = 50$ micron, respectively. Again, the optimal design is limited by the lower bound of the design space. The optimal number of channels is again found just after the chip width goes from nozzle-dominated to channel-dominated. However, the pressure drop at which this occurs is higher ($\Delta p = 1.25$ bar). This difference is explained by the nozzle being smaller in the first place, due to the decreased mass flow. This result means that if the pressure drop can be larger without affecting the chip width, it must be larger. I.e.: below a certain pressure threshold the pressure does not affect performance according to the model. This is because the nozzle is not yet dominating the chip width(see Section 3.5.4 on pressure drop affecting the throat width). If the pressure drop would be lower than this threshold, it comes at the expense of power consumption. After all, unnecessarily preventing pressure drops is done by decreasing the flow speed or channel length (see Eq. 3.95 for pressure drop).

Reducing the flow speed is accomplished by increasing the channel width, which increases the radiating chip area overall. This is because the chip is much longer than it is wide, and any potential decrease in channel length is tempered by reduced flow speed. Alternatively, increasing the wall temperature to decrease channel length quickly increases the radiation loss ($\propto T^4$).

The optimal top wall temperature is $T_w = 1039.4$ K. Just like Case 1 with $T_c = 600$ K, which has a 637.6 K wall temperature, the difference with the chamber temperature is only moderate.

The heating channel length is $l_c = 1.227$ mm, which is 33% shorter than the channel length of 1.826 mm in Case 1. This channel is much shorter, since the length to reach 600 K is much shorter with a wall temperature of about 1040 K compared to 640 K, as the temperature difference is much larger and the mass flow 33% lower. Heating it further to 1000 K is also easier due to the large difference in mass flow.

Aside from the aforementioned differences in pressure drop and channel length, there appear to be no major differences in the optimal values. Even the resulting difference in power loss is only moderate. In the next section the thrust will be varied instead, to see how this impacts the results.

An overview of the resulting chip geometry is in Table 5.2. Take note that just like in Case 1, the nozzle exit width $w_{\text{nozzle exit}}$ is only a bit lower than the inlet manifold width w_{inlet} (623 vs. 660 micron). Again this in spite of the 25% larger pressure drop in Case 2. Since the nozzle is almost the same,

and the amount of channels are the same, the inlet manifold length (as given by Eq. 3.117) and nozzle length (as calculated in Section 3.6.1) are virtually the same. Therefore, the total chip length between Case 1 and Case 2 has only changed due to the total heating channel length.

5.1.3. Case 3: 2mN thrust and 1000 K chamber temperature

In Figure 5.5 the optimal outcome for the case of $F = 2$ mN and $T_c = 1000$ K is presented. This case results in an specific impulse of $I_{sp} = 180.0$ s and a mass flow of $\dot{m} = 1.133$ mg·s^{-1}. The minimized power loss is $P_{\text{loss}} = 0.308$ W, together with an ideal power consumption $P_{\Delta h} = 4.391$ W resulting in total power consumption of $P_t = 4.700$ W. All the relevant values, comparing all three cases, are tabulated in Table 5.2.

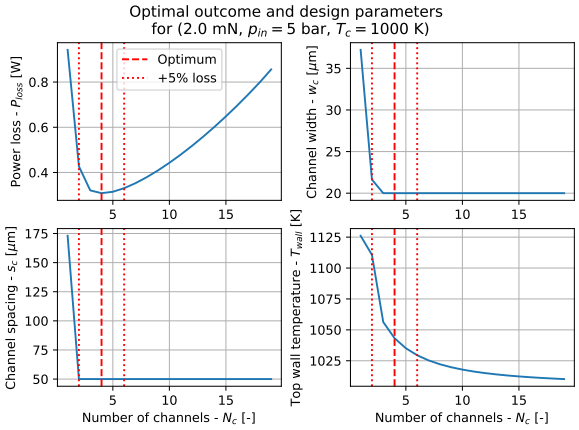

Figure 5.5: Optimal design for $F = 2$ mN; $T_c = 1000$ K resulting in $\dot{m} = 1.133$ mg·s^{-1} and $I_{sp} = 180.0$ s

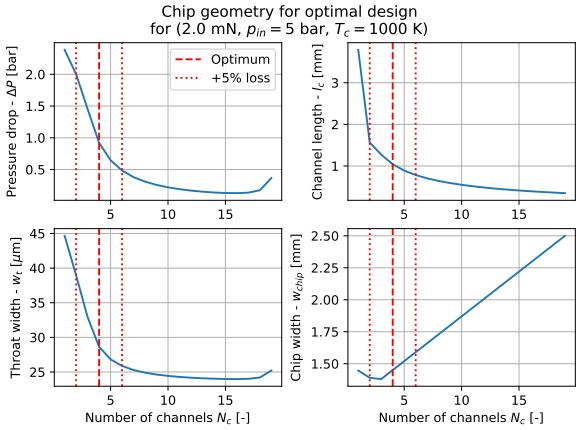

Figure 5.6: Optimal chip geometry for$F = 2$ mN; $T_c = 1000$ K resulting in $\dot{m} = 1.133$ mg·s^{-1} and $I_{sp} = 180.0$ s

Compared to Case 2, the optimum is at 4 channels instead of 7, again with channel widths and spacings at the lower bound. Looking at the bottom right plot of Figure 5.6, and comparing the inlet manifold and nozzle width in Table 5.2: $w_{\text{inlet}} = 450\mu$m and $w_{\text{nozzle exit}} = 286\mu$m shows that optimum again lies at the point where the nozzle width does no longer dominate the width of the chip.

The number of channels for which the power loss is first 5% higher or more than the optimum is now 2 and 6 channels. This is slightly narrower than the range for Case 2, but the excess power loss at 2 and 6 is higher. (comparing top left of Figure 5.5 and 5.3). At this lower thrust level, the power loss is more sensitive to the number of channels.

The power loss, is relatively speaking higher than at the higher thrust level: $\mu_{\text{mh}} = 7\%$ at $F = 2$ mN and $T_c = 1000$ K versus $\mu_{\text{mh}} = 5\%$ at $F = 4$ mN and $T_c = 1000$ K. This is most likely caused by the structural margins around the edge being constant at $w_{\text{margin}} = 0.5$ mm. The heating efficiency for different thrust levels will be further discussed in Section 5.2.1.

There are no further major differences between the cases.

5.2. Optimal power consumption for desired specific impulse and thrust

The previous section looked at the found optima when the thrust F and chamber temperature T_c were given. In this section all these optima are aggregated into high-level data. Results are generated for five levels of thrust F from 1 to 5 mN. The chamber temperature T_c runs from 500 to 1100 K. This results in a range of specific impulses I_{sp}: 122 to 190 s.

This entire range is presented, because there is no ‘optimal’ combination of I_{sp} and thrust F. From the perspective of the system engineer or chip designer, only this question makes sense: “What is the highest attainable I_{sp} for the desired thrust F, given a limited power budget for propulsion P_t?”. The results in Section 5.2.1 answer this question for the range of thrusts that were set in the design space (Table 2.5).

Section 5.2.2 looks at what the optimal design parameters are for the different thrust levels and I_{sp}. Finally, Section 5.2.3 looks at the large role the pressure drop and the nozzle play, when it comes to

determining the optimal outcome.

5.2.1. High-level performance

This high-level data shows the required total power consumption P_t for a given thrust F and specific impulse I_{sp} combination (Figure 5.7).

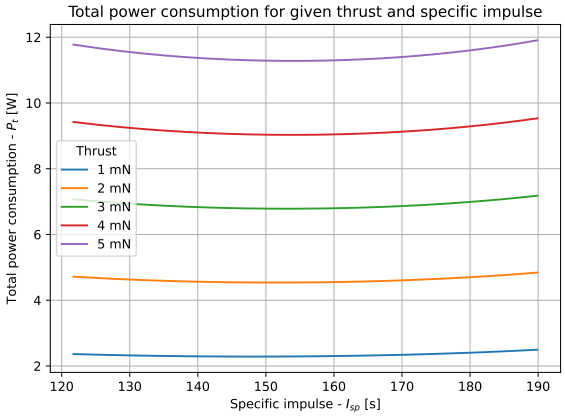

Figure 5.7: Optimized total power consumption vs. I_{sp} for $1-5$ mN thrust

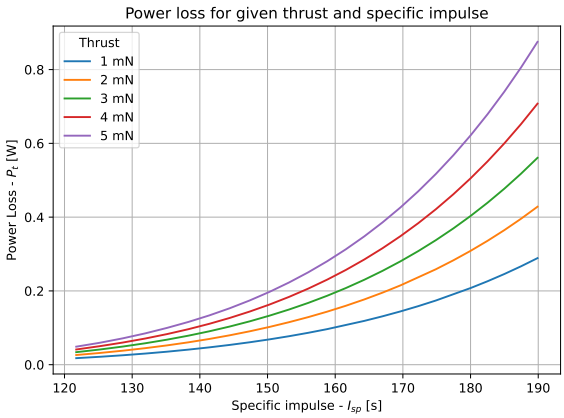

Figure 5.8: Optimized power loss vs. I_{sp} for $1-5$ mN thrust

The first noticeable thing is that the total power consumption does not monotonically increase with increasing I_{sp}. This happens despite the clear increase in power loss P_{loss} as shown in Figure 5.8. This is to be expected from IRT: for higher chamber temperatures/I_{sp} the mass $\dot{m}$ drastically lowers, resulting in a lower ideal power consumption $P_{\Delta h}$. To more clearly see this, both the ideal power consumption and the total power consumption are plotted in Figure 5.9 for $F = 4$ mN. Figure 5.10 shows the associated chamber temperature, mass flow and I_{sp} combination that explains this behaviour. It is, however, interesting to note that in literature the highest reported chamber temperatures in VLM was 573 K[13]. Aside from that, many VLM stay around 425 K [11, 14]. It is recommended that VLM researchers and designers should explore much higher temperature ranges. For instance, looking at Figure 5.9, the optimal power consumption decreases still towards $T_c = 750$ K. It suggests that below certain chamber temperatures a VLM design could potentially waste too much energy heating a high mass flow for a suboptimal I_{sp}. A better design with higher I_{sp} could be found for the *same* total power consumption P_t.

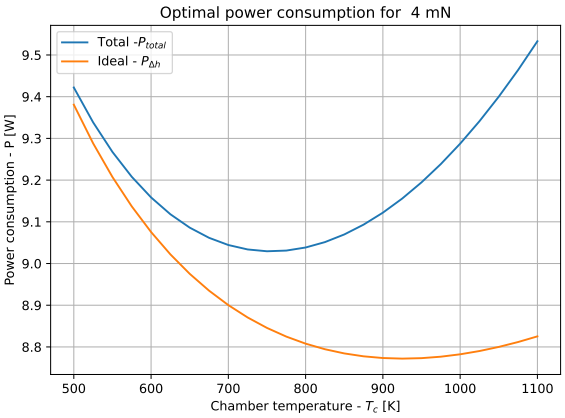

Figure 5.9: Optimized power consumption for $F = 4$ mN

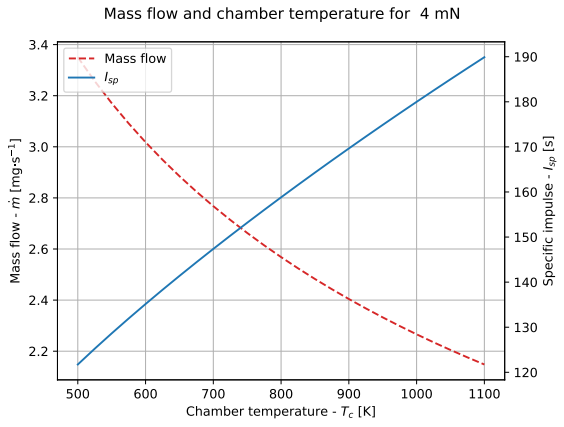

Figure 5.10: Mass flow and chamber temperature for $F = 4$ mN

In Figure 5.11 the heating efficiency μ_{mh} for different thrust levels and specific impulses is shown. For low specific impulse/chamber temperatures there is no large difference in the efficiency of the heaters

for different thrust levels. But the lower the thrust level, the lower the efficiency becomes as well. The heating efficiency drops as the specific impulse increases. This must be caused by the increase in wall temperature, as this happens despite the chip area A_{chip} decreasing with increased I_{sp}.

However, between thrust levels, it is the chip area that causes the difference in heating efficiencies. In Figure 5.14 in the next section it is clear that it is hard to discern a relation in the temperature at which the chip radiates for the same specific impulse I_{sp} and thrust F. The chip area A_{chip} did, however, not linearly scale back with the thrust level. At 5 mN the chip is about 7.5 mm^2 in size over the entire range, and for 1 mN it is about 2.5 mm^2. Per unit thrust, the chip therefore has more radiating area at the lower thrust levels, than at the higher thrust level. This is best explained by the margin of 0.5mm added around the nozzle and heating chamber with Equation 3.113.

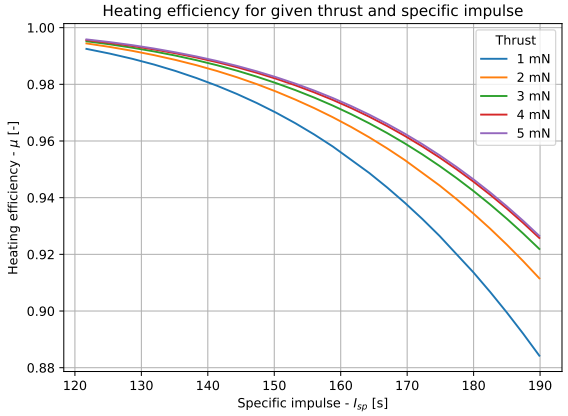

Figure 5.11: Heating efficiency for given thrust and specific impulse

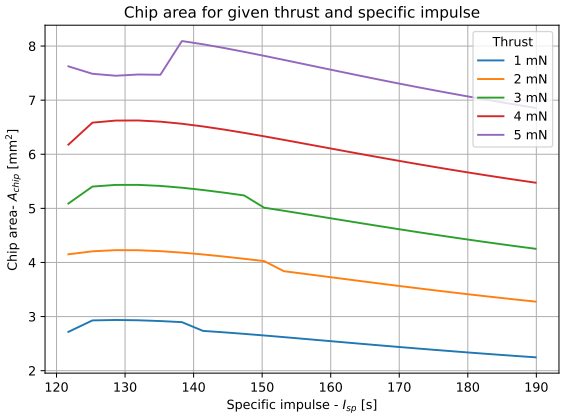

Figure 5.12: Chip area for given thrust and specific impulse

5.2.2. Design parameters

In this section, the resulting optimal design parameters are presented and investigated. The first result is to note that in all cases the optimal channel width w_c(20 micron) and spacing s_c(50 micron) was on the lower bound of the pre-determined design space (Table 2.5). The reason for this result was extensively discussed in Case 1 in Section 5.1.1, and in Section 5.3 the discussion will continue with a sensitivity analysis.

The two remaining parameters do, however, vary between all the found optimal solutions for different thrust levels. In Figures 5.13 and 5.14 respectively the optimal number of channels N_c and the superheat of the top wall $(T_{\text{w}} - T_c)$ are given.

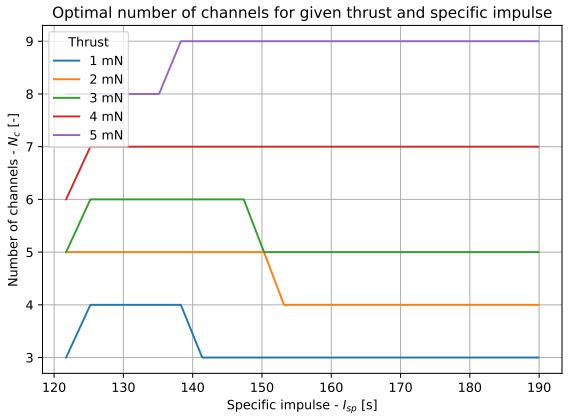

Figure 5.13: Optimal number of channels for given thrust and specific impulse

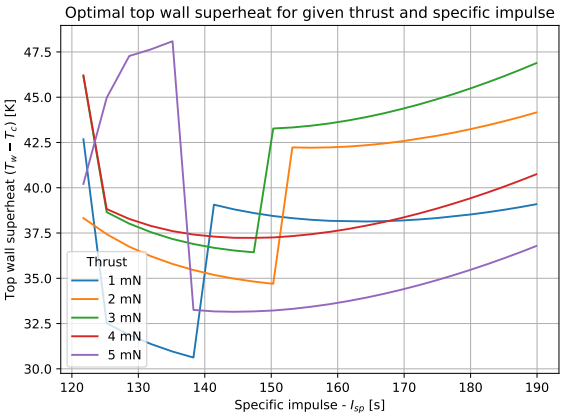

Figure 5.14: Optimal top wall superheat for given thrust and specific impulse

The optimal number of channels varies mostly between different thrust levels. Increasing thrust increases the required amount of channels for optimal power performance. At 1 mN about 3-4 channels are optimal, and at 5mN this is about 8-9 channels. It must be noted that the fluctuations in channel numbers for a given thrust level are not significant, as they arise from slight numerical fluctuations in the power loss P_{loss}. These fluctuations are much larger than conventional floating point errors. The optimization algorithm terminates when the power loss barely changes when the optimal guess is iterated (i.e.: the gradient of the objective function is almost 0.). This threshold is many orders of magnitude higher than regular floating point or other numerical errors.

Actually an attempt to prevent this was made when the optimization tool settings were determined (see Section 2.4.3). These type of fluctuations did show up in, for instance, the plots provided in Section 5.1.1. They never impacted the optimal power loss, but they did make it harder to analyse the data. These channel number fluctuations are much harder to prevent due to the discontinuous nature of the variable. It is not necessary to prevent this behaviour, as the results in Section 5.1.1 already showed that the optimal result barely changes with 1 or 2 channels more or less than the found optimum. In fact, it is this insensitivity that causes the fluctuations.

Moving to Figure 5.14 on the right for the top wall superheat, the result shown in Case 1 and Case 2 is the same here: it is optimal to only have a wall temperature that is moderately higher than the desired chamber temperature. All the values are well between 30 and 50K. This means that, during preliminary design, one can assume that the wall superheat is about 40 K to get a good result. Again, one can see sudden fluctuations, and these occur in tandem with the the sudden changes in channel numbers. Again, they do not affect the optimal power loss, but it is clear that for each number of channels there is a different optimal solution for the wall temperature.

Another result is that the wall temperature does not show a clear trend with the thrust level, but this does not necessarily mean that a relation between thrust and wall temperature does not exist. It could be that the trend is lost due to the optimal number of channels settling just a bit higher or lower over the entire range of solutions. If one, for instance, looks at the superheat for 1mN, it crosses the optimal solutions for the other thrust levels just by switching from 3 to 4 channels and back.

5.2.3. Pressure drop and throat width

Figure 5.15 and Figure 5.16 confirm the role the pressure drop Δp plays in designing an optimal VLM. In all cases in Section 5.1 the pressure drop tended to increase with decreasing channel numbers N_c. And it is this pressure drop that affects the throat width w_{throat} (Eq. 3.108). But still the throat width remains relatively constant for each thrust level, despite the large change in mass flow $\dot{m}$ and I_{sp}. Also, the pressure drop has significant fluctuations that coincide with the fluctuations in the number of channels (shown in Figure 5.13), but it was already established that these fluctuations barely affect the power loss.

This means that the pressure drop itself is not important, but its effect on the nozzle size is important. It confirms that the optimization tries to minimize the number of channels, but that it does not decrease further if the nozzle almost starts or has started to dominate the width of the chip. This result therefore gives an important recommendation to future VLM designers. It is not allowable to look at the nozzle and the heating channels in isolation, if one wants to find the optimal VLM design. The pressure drop is necessary to relate the two. This indirect importance of the pressure drop was not entirely anticipated. During the literature study the pressure drops of existing VLM[11, 13] were found to be much smaller than 1 bar.

To this recommendation must be added that this also means that the entire model can be vastly improved by including nozzle corrections, potentially with only a small increase in computational cost. During the design of the model, it was thought it would not be computationally efficient to include real nozzle effects in the model. The expectation was that it would drastically alter the mass flow $\dot{m}$ and I_{sp}/T_c. This would not only require an extra level of iteration, but it would also undo the benefits of the "pre-calculated" values (See Section 3.1.1).

Whilst it is true that including nozzle corrections would drastically alter the required flow conditions, it turned out that the Reynold's number of the throat Re_t was very insensitive to the pressure drop, and the corresponding change in nozzle size. As shown during the validation of the nozzle correction assumption in Section 4.2.5 with Figures 4.7 and 4.8. Since most important nozzle corrections depend on this Reynold's number(or other nozzle constants, such as the divergence half-angle $\alpha_{\text{divergent}}$), the nozzle effects could have been included by having a good initial guess of Re_t. Lacking a guess for

this value, one can make clever use of its near-invariance by performing only a few or even only *one* iteration(s), to find Re_t. The optimization can then be restarted with an extended IRT model, based on this found value, and one can safely assume it will barely vary any more.

It is expected that this addition would yield a large benefit if the work in this research is continued. First of all, including a discharge factor C_d would immediately impact the nozzle size and the radiating area. Secondly, including a correction factor $\zeta_{I_{sp}}$ on I_{sp} would require a higher chamber temperature to maintain thrust (as **TLR-01** requires the optimum design for a given I_{sp}). This would immediately impact the power consumption, as one would have to increase the specific enthalpy increase Δh, given in Equation 1.6, of the propellant even further.

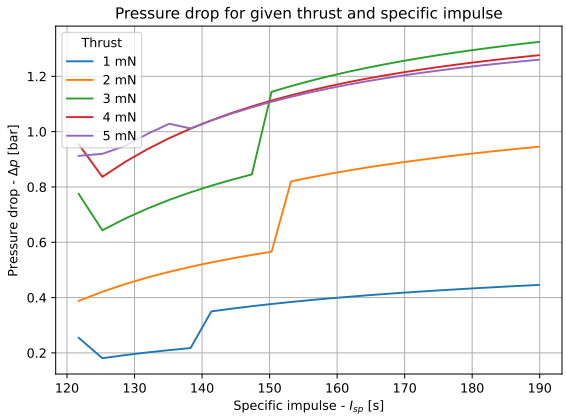

Figure 5.15: Pressure drop for given thrust and specific impulse

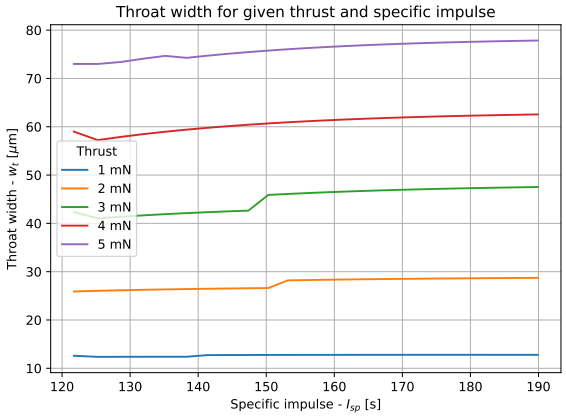

Figure 5.16: Throat width for given thrust and specific impulse

5.3. Sensitivity analysis

From the results earlier in this chapter, it became clear that the optimal outcome is likely to be sensitive to some contraints on the design space, and constants in the design of the chip. First of all, the channel width w_c and channel spacing s_c always were on the lower bound of the design space. If these values would be lower it can be expected to affect the power loss and optimal design parameters. These values will be varied down to investigate the results.

Also, it became clear that there is quite some interplay between the allowable pressure drop in the heating channels, the nozzle width, and the optimal number of channels. The nozzle width is, however, significantly affected by the area ratio. It is therefore necessary to see how a changed area ratio $\frac{A_e}{A_t}$ (which drastically affects the nozzle performance) will affect the optimal power loss and design parameters.

Take note that whilst the power differences in the figures and tables of this section are presented as a difference in *total* power consumption P_t, it is only the power loss P_{loss} that has changed. Just like in the design tool, great care was taken to only compare thruster designs with the same performance parameters (F, I_{sp} and $\dot{m}$). In the sensitivity analyses on the area ratio $\frac{A_e}{A_t}$ this meant that the range of specific impulses I_{sp} had to be truncated on the lower or higher range, as there was not necessarily a design available for comparison.

5.3.1. Channel width bounds

In all previously presented results the optimal outcome was that the channel width w_c was always equal to 20 micron, the lower bound of the design space given in Table 2.5. In this section it is investigated what the effect of this is on the found optima.

In Figures 5.17 and 5.18 respectively the absolute ($\Delta P_t \equiv P_{t_{\text{old}}} - P_{t_{\text{new}}}$) and relative($\frac{\Delta P_t}{P_{t_{\text{old}}}}$) power reduction are plotted. In Table 5.3 the maximum effect of the changed bound($w_c \geq 10\mu$m) is tabulated. This maximum occurs only at the highest chamber temperatures/I_{sp}. Also, both the absolute and relative power reduction tend to decrease with increasing thrust levels.

For the higher thrust levels (4-5 mN) this impact of this power loss difference is hardly important in the context of heating efficiency μ_{mh} (see Figure 5.11). It is at most a 4-8% reduction in a 7% power loss. So the benefit of smaller channels at these thrust levels is at most a 0.6% reduction in total power consumption. However, for 1 mN the result is more pronounced. In that case there is a maximum reduction in power loss of 31% on a power loss of almost 12%, resulting in 4.4% total power reduction. A reduction in the total power consumption of 4% at the highest chamber temperatures is therefore possible. However, at the lowest chamber temperature, there are no differences larger than 0.25%. Looking more in the middle with a specific impulse of $I_{sp} = 160$ s; $T_c = 810$ K at 1mN the reduction is already below 2%, and below 0.2% at 5 mN.

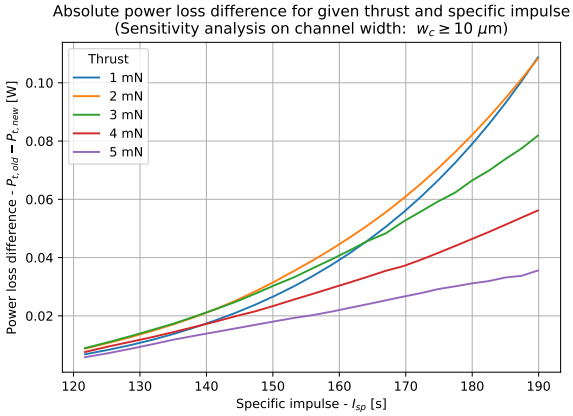

Figure 5.17: Absolute power loss difference vs. I_{sp} for $1-5$ mN thrust (Sensitivity analysis: $w_c \geq 10\mu$m)

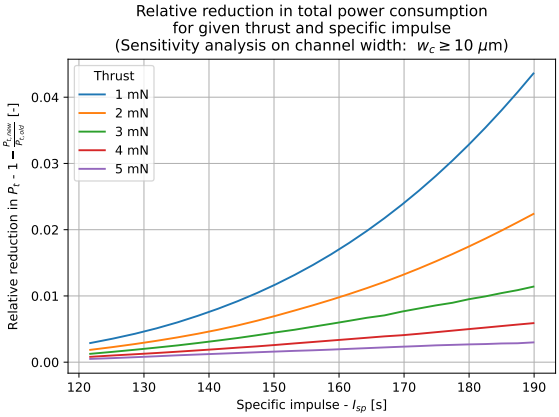

Figure 5.18: Optimized power loss vs. I_{sp} for $1-5$ mN thrust (Sensitivity analysis: $w_c \geq 10\mu$m)

Table 5.3: Overview of sensitivity analysis: maximum change

	Maximum absolute and relative power reduction							
	$w_c > 10$ μm		$s_c > 25$ μm		$\frac{A_e}{A_t} = 5$		$\frac{A_e}{A_t} = 15$	
Thrust [mN]	ΔP_t [W]	$\frac{\Delta P_t}{P_{t_{\text{old}}}}$ [%]	ΔP_t [W]	$\frac{\Delta P_t}{P_{t_{\text{old}}}}$ [%]	ΔP_t [W]	$\frac{\Delta P_t}{P_{t_{\text{old}}}}$ [%]	ΔP_t [W]	$\frac{\Delta P_t}{P_{t_{\text{old}}}}$ [%]
1	0.11	4.4 %	0.03	1.3 %	-0.20	-8.4 %	0.09	3.6 %
2	0.11	2.2 %	0.06	1.3 %	-0.35	-7.6 %	0.15	3.1 %
3	0.08	1.1 %	0.09	1.3 %	-0.50	-7.2 %	0.19	2.7 %
4	0.06	0.6 %	0.12	1.3 %	-0.64	-6.9 %	0.22	2.3 %
5	0.04	0.3 %	0.17	1.4 %	-0.77	-6.6 %	0.23	1.9 %

Reducing the channel width w_c does also impact the found optimal design parameters. First of all, the optimal number of channels increases across the board (Figure 5.19), with for instance 11-12 channels for 5 mN instead of 8-9 channels (Figure 5.13). This makes sense in the context of earlier results, where it was shown that the optimum tends to lie just behind the point where the channels start to dominate the chip width (instead of the nozzle). When the channels can be smaller it takes a larger number of channels to reach this point.

More interesting is the result that the channel width no longer lies precisely on the lower bound, except for the case of 1 mN and part of 2 mN (Figure 5.20). In the context of the mostly small changes in total power consumption in this sensitivity analysis, it means that there are likely to be only small benefits for reducing the bound on the design space below 20 micron for higher thrust levels. It is recommended to simply set the channel width to 20 micron if the thrust is above 4 mN to reduce computation time and simplify the model.

Lastly, it must be noted that the plotted channel widths in Figure 5.20 are not behaving smoothly. This is a numerical artefact of the optimization algorithm[2] . The fluctuations barely impact the power

[2]For the designer of a chip, these artefacts are hardly relevant, but for the purpose of analysing the main results the algorithm

loss, so the algorithm terminates early before converging to the true optimal value.

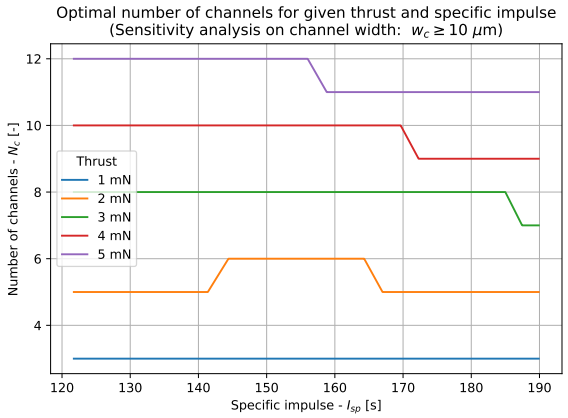

Figure 5.19: Optimal number of channels vs. I_{sp} for $1-5$ mN thrust (Sensitivity analysis: $w_c \geq 10\mu$m)

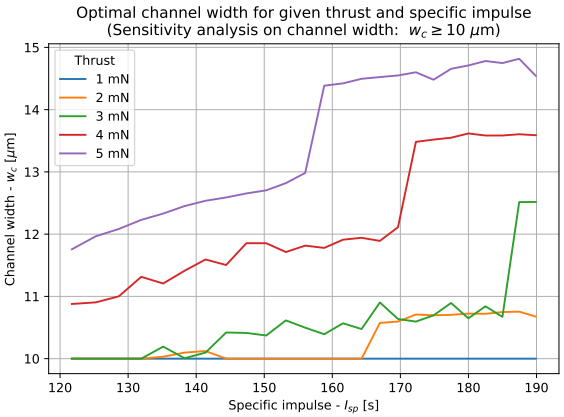

Figure 5.20: Optimized Channel Width vs. I_{sp} for $1-5$ mN thrust (Sensitivity analysis: $w_c \geq 10\mu$m)

5.3.2. Channel spacing/wall thickness

In this section the channel spacing/wall thickness s_c bound is lowered from 50 micron to 25 micron. In the earlier results, the optimal solution for this parameter was always $s_c = 50\mu$m. The first result is that the optimal value was still always on the lower bound with $s_c = 25\mu$m. The second result is that power loss differences were very small, ranging from at most 0.03 W for 1mN and $I_{sp} = 190$ s, and 0.17 W for 5 mN and $I_{sp} = 190$. These are respectively a 1.3% and 1.4% difference in total power consumption P_t. The relative decrease in power consumption was always below 1% for $I_{sp} < 178$ s (see Figure 5.22). In Figures 5.21 and 5.22, respectively the absolute and relative power reduction are shown over the entire range thrust and I_{sp} range.

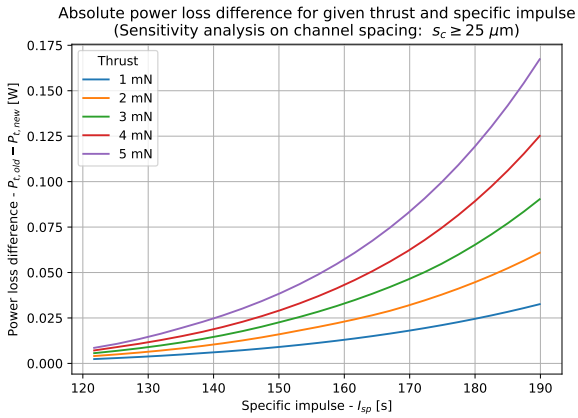

Figure 5.21: Absolute power loss difference vs. I_{sp} for $1-5$ mN thrust (Sensitivity analysis: $s_c \geq 25\mu$m)

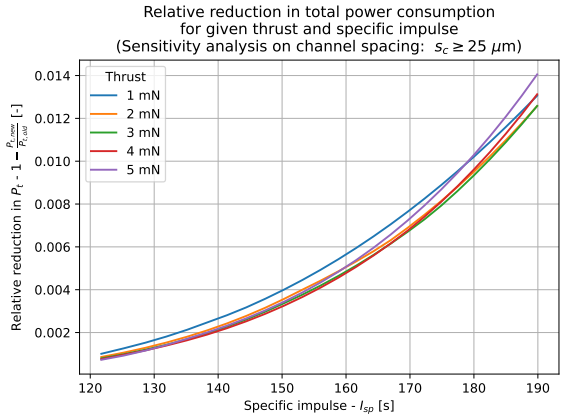

Figure 5.22: Optimized power loss vs. I_{sp} for $1-5$ mN thrust (Sensitivity analysis: $s_c \geq 25\mu$m)

The results for the other design parameters are that:

- the number of channels N_c has increased by about 1-2 channels for each thrust level (see Figure 5.23),
- the range for the top wall superheat $T_w - T_c$ has increased by about 2.5K,
- and optimal solution for the channel width remained $w_c = 20\mu$m.

was set to avoid this behaviour. (See Section 2.4.3) Producing 'smoother' data comes at a computational cost after all.

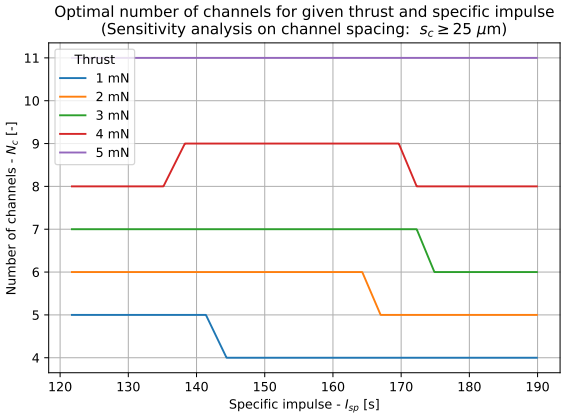

Figure 5.23: Optimal number of channels vs. I_{sp} for 1 – 5 mN thrust (Sensitivity analysis: $s_c \geq 25\mu$m)

Furthermore, when inspecting the effective wall temperature T_{ew}(Eq. 3.85), the difference with the top wall temperature T_{w}, was only between 6 and 12 K for all cases. Compared with the fluid temperature, the relative difference in heat transfer can thus be expected to be insignificant.

The overall finding is that reducing the bound on the channel spacing s_c moderately affects the optimal geometry and wall temperature, but barely influences the actual power loss. Although it is beneficial, it should therefore not be a priority to reduce the wall thickness when designing future VLM.

The effective wall temperature calculation was included because there had to be a sensible mechanism for the wall thickness to affect the heat transfer. Without it, the solution for the optimizer would always have been to pick the smallest possible value. This is because it would simply reduce the size of the chip with no penalty in heat transfer. The effect of including it, however, still yields the minimum s_c as the optimal solution, whilst only showing moderate differences in resulting power losses if the bound is lowered. This solution, however, comes at great computational cost, as one must introduce an iteration to find the correct effective wall temperature (explained in Section 3.4.5).

It is therefore recommended that one investigates whether the effective wall temperature calculation can be either omitted entirely, or be approximated by simply reducing the wall temperature by a few degrees to achieve the same effect.

5.3.3. Area ratio

In this section a sensitivity analysis on the area ratio $\frac{A_e}{A_t}$ is performed. From IRT is known that the area ratio impacts the mass flow $\dot{m}$, specific impulse I_{sp} and the size of the nozzle. Because only cases with the same I_{sp}, mass flow and thrust F are compared, the ideal power consumption for each case is the same[3].

When the **area ratio is 5** instead, there is an *increase*[4] in total power consumption in all cases. In Figure 5.24 one can see that absolute power difference increases in magnitude with the thrust level. At an I_{sp} of 180 s, this difference is maximally 0.20 W for 1 mN, and 0.77 W for 5 mN.

Relatively speaking, the difference is only about 3% at the lowest I_{sp} of 122s. The relative change increases with the I_{sp}. For $I_{sp} = 180$ s it is -8.4% for 1 mN and -6.6% for 5mN. The difference across the entire range is plotted in 5.25. An overview of the maximal changes can be found in Table 5.3.

When the **area ratio is 15**, there is a decrease in total power consumption. Again, the absolute difference is larger for higher thrust levels(See Figure 5.24). It is at most 0.23 W lower for an $I_{sp} = 190$ and 5mN thrust, and 0.09 W lower for 1 mN.

The relative difference is shown in Figure 5.27. At the lowest I_{sp} the difference in power consumption is less than 1.5%, and for the highest specific impulse, the relative decrease become 3.6% for 1 mN, and 1.9% for 5 mN.

[3]Unlike the other sensitivity analyses, there is no longer a precise one-to-one correspondence between the data points of the baseline and the new cases. The same chamber temperatures T_c does, after all result in different I_{sp} and $\dot{m}$ for the same F.The I_{sp} range was therefore truncated, and the power losses were linearly interpolated.

[4](i.e.: a negative power reduction)

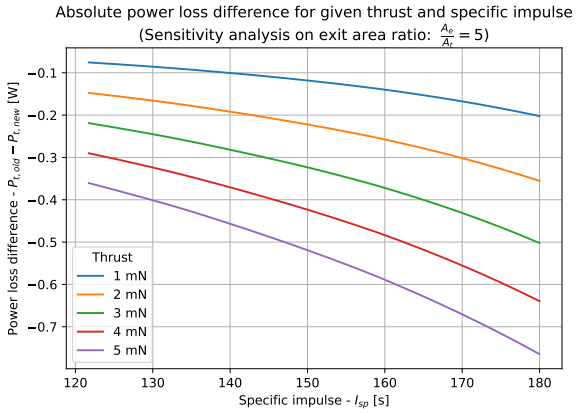

Figure 5.24: Absolute power loss difference vs. I_{sp} for $1-5$ mN thrust (Sensitivity analysis: exit area ratio $\frac{A_e}{A_t} = 5$)

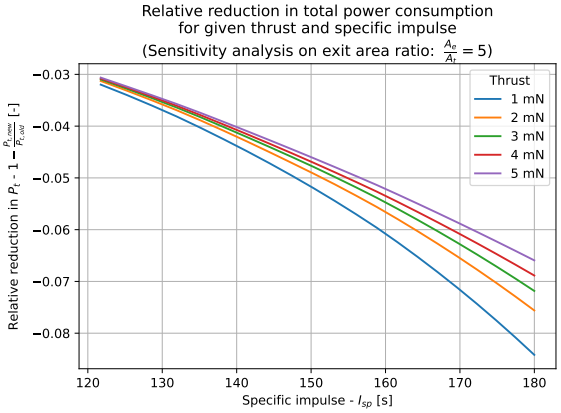

Figure 5.25: Optimized power loss vs. I_{sp} for $1-5$ mN thrust (Sensitivity analysis: exit area ratio $\frac{A_e}{A_t} = 5$))

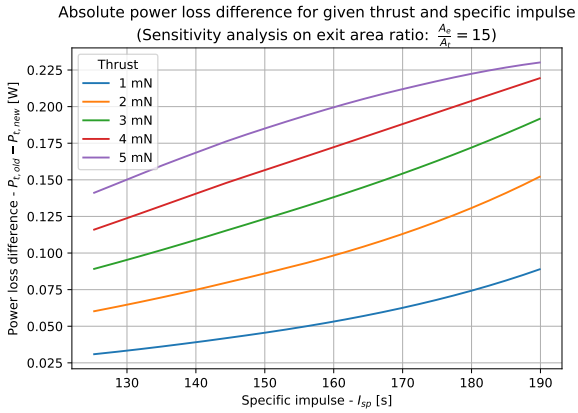

Figure 5.26: Absolute power loss difference vs. I_{sp} for $1-5$ mN thrust (Sensitivity analysis: exit area ratio $\frac{A_e}{A_t} = 15$)

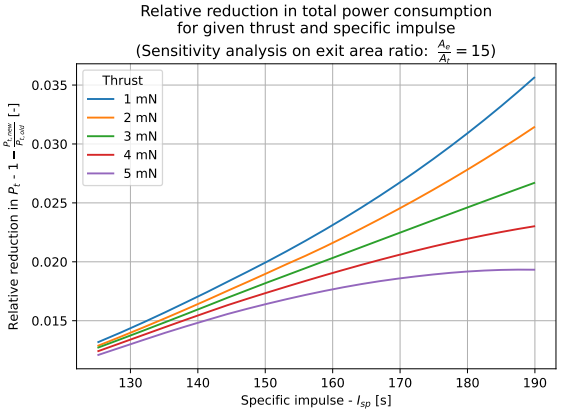

Figure 5.27: Optimized power loss vs. I_{sp} for $1-5$ mN thrust (Sensitivity analysis: exit area ratio $\frac{A_e}{A_t} = 15$))

As for the resulting optimal design, in both analyses ($\frac{A_e}{A_t} = 5$ and $\frac{A_e}{A_t} = 15$), the following optimal parameters remained the same: channel width ($w_c = 20$ micron) and channel spacing ($s_c = 50$ micron). There was no apparent difference in the range of top wall superheat compared to the baseline either. For the higher area ratio, the optimal number of channels slightly increased for thrust levels about 3mN with about 2-3 channels and remained roughly the same for the lower thrust levels. For the lower area ratio, the optimal number of channels only decreased by about 1-2 channels for the highest thrust of 5mN.

Since only cases with the same specific impulse I_{sp}, mass flow $\dot{m}$ and thrust F are compared in this analysis, one must take in mind that the *overall ideal* performance must be the same. The shape of the nozzle and the chamber temperature have changed, and this shape results in the same nozzle performance.

The result of changing the area ratio is thus solely the effect on the optimal geometry of the heating chamber, the change in chamber temperature, and the change in power loss through the differently-sized nozzle.

Looking at the area ratio of 15, the combined effects of increasing $\frac{A_e}{A_t}$ are quite moderate, given the expected change in chamber temperatures for the same specific impulses I_{sp} with only a few percent 2-4% improvement in power consumption (in the best case for high I_{sp}). The penalty for reducing it to $\frac{A_e}{A_t} = 5$ is, however, more severe and between 6-8% for the highest I_{sp}. Crucially, it was always 3% worse or more.

Since the effect is very moderate, it is recommended that one does not vary the area ratio $\frac{A_e}{A_t}$ based on the design tool results. Instead it is likely that more improvement will be made by selecting a value that has been shown to work in earlier designed VLM. It is, for instance, unclear whether condensation effects will become an issue if the area ratio is increased beyond 17 (as stated before in Section 2.2.2). Also, from IRT it is known that further increasing the area ratio comes with rapidly diminishing returns[8]. This means, it is expected that there will quickly come a point at which increasing the area ratio is no longer beneficial, but starts leading to more power losses instead. The increased nozzle size, and the heat lost through it, will then counteract nozzle performance, resulting in lower overall performance.

5.4. Comparison of found optimum to other VLM design

In this section an optimal design for the VLM of Cen and Xu[13] with the highest inlet pressure p_{in} is presented. Just as in the validation chapter, it must be restated that data is not complete enough to warrant a proper comparison (see Section 4.2.1). To compensate for this, a chamber temperature T_c has to be assumed. This temperature is taken from the validation results in Table 4.1. This temperature would result in the actual channel length l_c, provided that the used heat transfer relations are valid (see Section 4.2.2 for more details). The comparison here thus answers the questions: *Is the design of Cen and Xu optimal, provided that the heat transfer relations are valid? If not: what design is optimal?*

An overview of the (changed) parameters are given in Table 5.4. The optimal result and the original design are given in Table 5.4. The optimal result yields that more and smaller channels are optimal: 23 channels with a width of 24.2 micron, instead of 9 channels with a width of 80 micron. The original design has a combined wetted perimeter $N_c \cdot P$ of 3.6 mm, and the optimal solution 6.6 mm. This is 84% more surface area per unit length of channels. The top wall temperature T_{w} has also increased by 5.5 K from 573.15 K to 578.67 K. The hydraulic diameter D_h was originally 96.0 micron, and in the optimal case is 40.3 micron (2.4 times smaller). The channel length has become 1.483 mm, 4.0 times shorter than the original 6 mm. These new channels are associated with a pressure drop of 0.4 bar Δp, resulting in a corrected nozzle width of 178.6 micron, therefore, a slightly larger and longer nozzle. The overall chip length has reduced to 9.644 mm from 13.485 mm, mostly due to the decreased channel length l_c. The chip width has barely changed: 5.120 mm originally, versus 5.214 mm in the optimal design. The total chip area A_{chip} has therefore decreased from 69.042 mm^2 to 50.279 mm^2.

The chip area A_{chip} has substantially reduced in size (27%) , whilst the top wall temperature T_{w} has only increased 1.0%. The radiation per unit area has thus only increased by about 4%. Based on this alone, one would expect that the power loss has decreased 24%[5]. This power reduction is mostly accomplished by the 75% decreased channel length l_c, which in turn is accomplished by finding a more optimal design of the channels.

This decrease is very large, but makes sense. The combined effect of the increase in wetted perimeter P (+84%) and the decrease in hydraulic diameter D_h (-58.3%) is on its own sufficient to explain the change. The increased wetted perimeter simply increases the area per unit length through which the flow is heated, according to Equation 3.18. And the convective heat transfer coefficient h_{conv} scales inversely with the hydraulic diameter, provided the Nusselt number Nu remains the same (Equation 3.16). Under fully developed laminar flow assumptions in the gas section of the channel (which is by far the most significant in length) the Nusselt number can indeed be expected to remain the same (see 3.45 and 3.47). Together, the optimal channel geometry does indeed result in 77% shorter channel length according to the model.

It must be noted that the comparison does show the value of the design tool, as it is not caused by other factors such as differences in heat transfer relations. The lack of complete data was alleviated by properly choosing the chamber temperature, based on earlier validation results. If the original input parameters in Table 5.4 are provided to the model, it will results in precisely the same chip geometry as the original, and precisely the same ideal performance. The design tool has therefore accomplished a potential decrease of 24% in power loss, provided the model is valid. Also, seeing that the nozzle and channels are again about the same in size, it again shows that it is important to include the pressure drop and nozzle-rescaling in the design of the heating chamber.

[5]The original power loss is not known.

Table 5.4: Design tools settings for optimal design comparison with VLM from Cen and Xu

Parameter	Value	
Thrust F	7.71	[mN]
Chamber temperature T_c	557.80	[K]
Inlet pressure p_{in}	2.52	[bar]
Area ratio $\frac{A_e}{A_t}$	11.72	[-]
Divergent half-angle $\alpha_{\text{divergent}}$	15	[deg]
Convergent half-angle $\alpha_{\text{convergent}}$	45	[deg]
Channel depth d_c	120	[-]
Chip width margin w_{margin}	1.56	[mm]

Table 5.5: Optimum design compared to original design[13]

Input parameters			
	Original	Optimal	
Number of channels - N_c	9	23	[-]
Channel width - w_c	80	24.2	[μm]
Channel spacing - s_c	50	50	[μm]
Top wall temperature - T_{w}	573.15	578.67	[K]
Resulting length dimensions			
	Original	Optimal	
Inlet manifold length - l_{inlet}	4000	3.848	[mm]
Heating channel length - l_c	6.000	1.483	[mm]
Convergent nozzle length - $l_{convergent}$	0.484	0.739	[mm]
Divergent nozzle length - $l_{divergent}$	3.000	3.573	[mm]
Total chip length - l_{chip}	13.485	9.644	[mm]
Resulting width dimensions			
	Original	Optimal	
Inlet manifold width - w_{inlet}	2000	1924	[μm]
Total channel width	1120	1657	[μm]
Throat width - w_{throat}	150	178.6	[μm]
Nozzle exit width - $w_{nozzle\ exit}$	1758	2094	[μm]
Chip margin width - w_{margin}	1.562	1.562	[mm]
Total chip width - w_{chip}	5.120	5.214	[mm]
Other results			
	Original	Optimal	
Resultant pressure drop Δp	0.30(0.25[c])	0.40	[bar]
Mass flow $\dot{m}$	5.985	5.985	[mg·s^{-1}]
Specific impulse I_{sp}	131.4	131.4	[s]
Ideal power consumption $P_{\Delta h}$	17.51	17.51	[W]
Power loss P_{loss}	0.622[c]	0.429	[W]
Total power consumption P_t	18.139[c]	17.947	[W]
Total chip area - A_{chip}	69.042	50.279	[mm^2]

c=calculated with the model

5.5. Limitations

The results presented in this chapter come with some limitations. Some stem from the scope of the research, others from making choices that were not wise in retrospect, and some simply from time constraints. The main limitations at this point are that:

- no quality factors are included in the nozzle model,
- no conduction losses are included in the heat loss,
- constant wall temperature was assumed,
- and the heat transfer relations are not necessarily accurate for the range of Re numbers in the channel.

The first point was omitted, even though it was originally planned to be included. As the pressure drop in the optimal designs turned out to be higher than anticipated, it was thought it was no longer possible to keep the mass flow in the channels and nozzle consistent without adding a computationally intensive iteration (see Sections 2.2.4 and 4.2.5 for details). This line of thought turned out to be incorrect, and quality factors could have included relatively easily.

The main consequence of this is that the I_{sp} is overestimated. For example, the thruster of Cen and Xu[13] has a nozzle quality factor $\zeta_{I_{sp}}$ of about 0.8 (see Table 4.1). This means that a 25% higher mass flow $\dot{m}$ is needed to achieve the desired thrust F. In the results presented above, heating and vaporizing water takes up 90% of the power consumption in almost all cases. This higher required mass flow thus lead to a 22.5% increase in power consumption. This is clearly significant, as it is larger than the currently calculated heat loss.

It is therefore recommended that quality factors are included in future research. In the current state of the design tool, including this should be trivial, as the nozzle model is neatly separated from the rest of the code. All that is required is a method for establishing the Re_t a-priori, or a good estimation of its value.

The second point is that no conduction losses were implemented. The main reason for this was the time constraint of the thesis, and prioritizing other issues more central to the research. Within the limited time, it was hard to find values for the thermal conductivity of the Printed Circuit Board (PCB) that the chip would be mounted on, or to establish precisely how heat would be conducted away. The latter would be difficult due to the assumption of constant wall temperatures at the top and bottom. It is assumed that most heat would be lost by conduction through fastening to the structure. If this type of conduction was to be implemented, it would linearly scale with the temperature of the chip. This means that on top of the power consumption, presented in figures like Figure 5.7, there would be an additional heat loss that would increase with the desired I_{sp}. Potentially, this could alter the total power consumption P_t to be more sensitive to the change in chamber temperature T_c and I_{sp}, and reverse the trend that power consumption decreases with increased I_{sp}.

The third point is that a constant wall temperature T_w was assumed. It is not uncommon that temperature gradients are reported through micro-channel flow boiling literature, such as in the work of Zhang et al.[26]. Often this temperature gradient is the result of constant heat flux assumptions instead, and not from modelling heat flow through the chip walls. Hanselaar did attempt to determine effect of the temperature profile through modelling the heat flow through the walls of the silicon chip, but found at most 3.1 K differences in temperature[19]. The situation in this research would not have been different enough to expect different results, so likely it would barely have had an impact on the results.

The last point was discussed earlier in Section 4.2.5, where it was found that the channels were not much longer than the assumed hydrodynamic entrance length. This means that the flow is not fully developed laminar flow, but thermally developing laminar flow. It is expected that in this flow regime the heat transfer is actually further enhanced, and therefore shorter channels would suffice. This should decrease the heat losses.

5.6. Conclusions

The most important result is that current VLM designs might have an unnecessarily low performance due to low chamber temperatures. When a propellant must be heated and vaporized by an external power source, designers must realize that the mass flow can be drastically lowered by increasing the

chamber temperature. This means that it is possible to increase the I_{sp}, whilst still decreasing the (ideal) power consumption. The highest reported chamber temperature in literature of 573 K is too low to reap this benefit. The results indicate that the chamber temperature can be increased to about 750K before the total power consumption P_t starts increasing again. In fact, for the *same* power consumption, there can be two associated I_{sp}, a low and a high one. Naturally, the latter is preferred. In answer to **RQ3** it can thus be said that VLM performance can be improved drastically if higher chamber temperatures are used.

Another major insight is that the pressure drop was much higher in the optimal designs, than for the designs described in literature. The pressure drop itself played no *direct* part in heat transfer or heat losses. Instead, the pressure drop required the nozzle to be rescaled to maintain the desired thrust and specific impulse, which affected the radiation losses through the nozzle section of the chip. This effect is the reason that the interplay of pressure drop and the nozzle must be included when design a VLM heating channel. In the optimal results, the pressure drop always tended to be just high enough to prevent the nozzle from making the chip wider than was required to contain all the heating channels in the chip width. Designing for lower pressure drops than this, results in more power loss. In answer to **RQ2** it can be said that it is *not* allowable to neglect pressure drop, so that its effect on the nozzle can be included. As a design consideration (for **RQ3**) one must not unnecessarily avoid pressure drops and only ensure that the pressure drop does not result in too large a nozzle.

Additionally, in Sections 5.1.1-5.1.3, three cases with given thrust and chamber temperature were investigated in detail. One major finding is that the chip design is limited by the lower bounds on the channel width w_c and channel spacing s_c in all cases. This finding persisted when the entire range of thrusts from 1 to 5mN , and from 500 to 1100 K chamber temperature was considered in Section 5.2. This seemed to indicate that the design can be improved if the limitations on these values can be reduced. However, during the sensitivity analysis on the channel width, only for low thrust levels and high chamber temperatures were there large reductions in total power consumption.

The analysis of the three cases also yielded the following design insight (as answer on **RQ3**): it is possible to ‘defensively’ design a chip with slightly more channels than is optimal. The geometry of the chip does not drastically change with a few more channels. Perhaps the wall temperature would have to be tweaked to yield the desired result, but that is a parameter that can be changed after the chip is produced, and would have a minor effect on power loss.

Furthermore the three sample cases revealed that modelling the temperature profile around the channel walls was of limited benefit. Ultimately, the temperature differences between the top and the bottom wall were slight. Including this effect resulted in only about 9 % less power losses through the bottom of the chip, whilst only marginally affecting the effective wall temperature (10 K or less difference). In answer to **RQ2**, it can therefore be said that assuming a constant wall temperature all along the channel perimeter is allowable.

Lastly, when the thruster of Cen and Xu[13] was fed into the design tool, the optimization algorithm found that the power losses could be decreased by about 0.2 W. This is done by reducing the channel width from 80 micron to 24.2 micron, and increasing the amount of channels from 9 to 23. This reduced the heating channel length from 6.0 mm to 1.5 mm. The reduced heat loss was mostly explained by the reduced chip size (69 mm^2 to 50 mm^2).

6

Conclusions

The research objective set in the introduction (Section 1.4) was as follows:

> "To develop a practical and accurate preliminary design tool to aid in designing efficient VLM heating chambers, by establishing which combined thermal/multi-phase flow model approach accurately predicts heating chamber performance."

The main research subgoals were split into several research questions(**RQ0-RQ02**), the answers to which shall be summarized below. **RQ3** on the design recommendations shall instead be discussed in Section 7.1 in the next chapter on recommendations.

6.1. Top Level Requirements

RQ0 was:

> What are the Top-Level Requirements(TLR) for the preliminary design tool?

The Top-Level Requirements (TLR) have already been established and justified in Section 2.1. They are tabulated in Table 2.1. Here they will be checked for compliance, with the results given in Table 6.1. For the justification, the reader is referred to the relevant sections. The TLR that were not or only partially complied with will be discussed below.

TLR-05 required that the calculated power consumption was accurate within 20%. There was only one paper available with power measurements at the time of writing, but it did not have a functioning thruster in it. However, despite the lack of validation data, it can safely be assumed that this requirement was not met. In Section 5.5 on the limitations it was concluded that the lack of quality factors in the nozzle model has a major impact on the mass flow. The mass flow can easily be 25% higher than as determined by Ideal Rocket Theory (IRT) for the desired thrust. So the total power consumption also rises by about this percentage. It is therefore unlikely that this requirement is met.

This immediately ties in to the partial compliance with **TLR-09**, which required that the tool should be compatible with nozzle model using quality factors. Technically, the design tool was capable of this, but it was not implemented due to uncertainties concerning the Reynold's number in the throat Re_t. The consequence is that the mass flow and specific impulse are not accurately estimated. This also has an impact on the calculated power consumption and thrust.

TLR-06 required that the design tool was compatible with multiple design geometries. Due to time constraints, not all geometries were implemented. The impact of this is that relative efficiency of different designs cannot be compared.

Table 6.1: Top-Level Requirements: compliance matrix

Id.	Requirement	Compliance?	Clarification/reference
TLR-01	*The design tool shall find the optimal design resulting in a minimal calculated power loss (+/- 1%) for a fixed thrust F and specific impulse I_{sp}.*	**Yes**	The *calculated* power loss was validated to be the global minimum. (See Section 4.2.6)
TLR-02	*The design tool shall be able to provide the highest possible I_{sp} given a thrust F and a total power constraint P_t.*	**Yes**	See resulting plots of design tool in Section 5.2
TLR-03	*The design tool shall work with a thrust F range from 0.01 mN to 10 mN.*	**Yes/Partial**	Shown to work in for 1-5 mN range in Chapter 5. No issues discovered down to 0.5mN and up to 10 mN, but not extensively checked.
TLR-04	*The design tool shall work chamber temperatures T_c up to 1000 K.*	**Yes**	Results generated from 500 to 1100K. See Chapter 5.
TLR-05	*The calculated total power consumption P_t shall be accurate within 20%.*	**No/Unknown**	No data available for validation.
TLR-06	*The design tool shall work with at least the following geometries: "single rectangular channel", "parallel rectangular channels", "snake channels", "metal mesh"*	**Partial**	Results generated for single/rectangular parallel channels in Chapter 5. Other geometries can be implemented if heat transfer relations are provided for it.
TLR-07	*The main output shall consist of at least a complete geometric description of the design from the inlet manifold to nozzle exit, together with the top wall temperature T_w and the total power consumption P_t.*	**Yes**	See Chapter 5.
TLR-08	*The auxiliary output shall be sufficient to provide insight into the characteristics of an optimal design, to establish the validity of the design tool, and to make recommendations for future Vaporizing Liquid Micro-thruster (VLM) design.*	**Yes**	See Chapter 5.
TLR-09	*The design tool shall be compatible with nozzle models like IRT and conventional extensions of IRT using quality factors.*	**Partial**	Only IRT implemented, but change of nozzle model is possible if Re_t is provided. See Section 4.2.5.
TLR-10	*The design tool shall be compatible with arbitrary empirical relations for heat transfer and pressure drop*	**Yes**	See Appendix A.
TLR-11	*The design tool shall be compatible with arbitrary liquid mono-propellant*	**Yes**	See code repository: "FluidProperties" class.
TLR-12	*The design tool shall be open-source.*	**Yes**	See code repository.
TLR-13	*The design tool shall provide the optimal design within 1 hour, on a 2018-issued TU laptop.*	**Yes**	Author owns laptop. Run-time is below 15 minutes.

6.2. Heat transfer models

RQ1 was:

> Which multi-phase heat transfer model is most suited for preliminary design purposes?

The applicability of heat transfer models is mostly determined by flow similarity parameters, mass fluxes and the hydraulic diameter. The expected values for these were determined in Section 2.2.6 based on the data from existing VLM.

In the Section 3.2 a range of possibly applicable heat transfer relations was established and these were implemented in the program. It ranged from fully developed laminar flow(low Re) to turbulent flow(high Re). This was done to be open to the possibility that the optimum would lie in flow regime with a higher Reynold's number than anticipated.

However, during validation in Section 4.2.5 it was shown that the flow regime was more deeply laminar than anticipated. The flow regimes in the optimal designs turned out to be thermally developing laminar flows. The answer to **RQ1** is therefore that heat transfer relations for thermally developing flow in micro-channels are most suited for the preliminary design of VLM.

6.3. Assumptions / modelled phenomena

RQ2 was:

> Which assumptions are allowable for preliminary design purposes, and which must be discarded?

As the scope excluded 3D-models, one must assume certain behaviours along the neglected dimensions in the model. The research focussed mostly on the geometry of the heating channels. Therefore the made assumptions focused on the effects of the geometry on the heat transfer and the heat losses.

Based on literature, it was assumed that the pressure drop would be small and therefore could be neglected. During the course of the research, it became clear that it is absolutely necessary to model the pressure drop in the channel and its effect on the nozzle size(see Section 5.2.3). Without it, it is not possible to factor in the effect of the number of channels and the channel width on the overall heat loss. This is because the nozzle size plays an important role in the heat loss, as it radiates away heat.

It was also thought that it was necessary to model the temperature profile along the walls of the heating channels. Otherwise there would be no mechanism for the channel spacing/wall thickness to affect the heat losses. However, the channel spacing always tended to the smallest possible value(25 micron). The effective wall temperature was barely different from the top wall temperature (10 K or less). Consequently, the radiation losses from the bottom of the chip were also barely different. It was therefore concluded that it is allowable to neglect the effect of the wall thickness on the heat transfer and heat losses.

Lastly, an unexpected result was that despite the rescaling of the nozzle, required due to pressure drop, the Reynold's number in the throat stayed relatively constant. This means that if one were to implement a nozzle model with correction factors based on the Reynold's number(as is convention), that one can assume that it barely changes even if the nozzle changes. This means that no iteration is required to account for the changed nozzle performance after rescaling the nozzle. Instead the nozzle throat can be linearly rescaled with the pressure drop to achieve the desired mass flow (see Section 3.5.4).

7

Recommendations

Over the course of the research some additional findings and recommendations could be established. The next Section 7.1 focuses on design recommendations that pertain to Vaporizing Liquid Microthruster (VLM) design. Afterwards, in Section 7.2, recommendations for further developing the model will be given. Lastly, the other more general recommendations are presented in Section 7.3.

7.1. Design recommendations

RQ3 was:

> What design recommendations can be established based on the results of the design tool?

Aside from producing optimal designs, the design tool also provided pointers towards better VLM designs. The most important recommendation is to focus all efforts on increasing the chamber temperatures of VLM. Ideal Rocket Theory (IRT) predicts that required mass flow of a thruster greatly decreases with chamber temperature. Even though the specific enthalpy increase required increases, the power required to heat the flow reduces, as the mass flow decreases so much that it offsets this increase. This means that in the ideal case, up to about 750 K chamber temperature, the power consumption decreases whilst the specific impulse I_{sp} increases. The highest reported chamber temperature of VLM is currently 573.15 K, so it is recommended to focus efforts on increasing the chamber temperature.

The second important design consideration is that more and smaller channels can be employed to decrease the heating channel length, which in turn decreases the chip size. This reduces the heat losses by reducing the radiation from the chip. This can be done even if it increases the pressure drop in the heating channels. The effect of the pressure drop on heat losses is marginal, as long as it does not result in too large a nozzle. This is because the nozzle throat width must increase to accommodate the same mass flow.

7.2. Modelling and design tool recommendations

There are several steps to take to improve the design tool performance. Firstly, it is recommended to no longer model the temperature profile around the channel walls[1]. The effect on the effective wall temperature was marginal, and so was the effect on the heat loss. This will reduce the computation time of the model substantially (10 times faster at the very least) and potentially free up computation time for modelling more important phenomena.

Secondly, it is important to include a nozzle model with quality factors, such as proposed by Makhan[20]. Including discharge and nozzle quality factors will greatly improve the design tool performance.

Lastly, it is recommended that further students and researchers monitor the field of micro-channel flow boiling. This field of research is very related to the flow regimes in VLM heating chambers. Sadly, it was concluded that the flow regimes in the optimal designs were more deeply laminar than anticipated. Any new findings or heat transfer relations, that originate from the field of micro-channel flow boiling literature, are likely to be applicable to VLM research.

[1] It is trivial to disable it in the code, by simply not passing the parameters describing the wall into the model. The model then automatically reverts to using the (top) wall temperature.

7.3. Other recommendations

One finding was that the model often tried to find solutions with the minimum channel width and spacing. In the scope of the research it was hard to determine what precisely limits this minimal value. The sensitivity analysis did not show large improvements in power consumption when these bounds were lowered, but nonetheless there are some small benefits from determining how small the channel walls and widths can be.

Last but not least, it is recommended that VLM researchers generate more complete data sets. At the time of writing, there was no known data set which included both the chamber temperature and wall temperature of a thruster. This makes it impossible to validate a heating channel model directly. Also, no data was found on total power consumption of VLM, which makes it hard to validate the calculated heat losses.

A

Software code

The code repository is available at `https://github.com/j-thd/thesis/`. A more slimmed down version, focused on a bit more usability, can be found at `https://github.com/j-thd/tidy-thesis`.

A.1. Extending the model

The arbitrary heat transfer relations are called in the models.one_D.py.

For the single-phase section of the model `Nu_func` is the arbitrary heat transfer function passed to the function `calc_channel_single_phase` at (`https://github.com/j-thd/thesis/blob/master/models/one_D.py#L71`).

`Nu_func` is passed the dictionary `args`, which currently contains the NumPy arrays `Re` and **Pr** for the Reynold's Re and Prandtl Pr. If required, new key-value pairs can be added to the dictionary, if future Nusselt relations require them.

For the two-phase section the function is `calc_homogenous_transition`: `https://github.com/j-thd/thesis/blob/2dd0f72bacf293509a17125bb377b5c1b1990a5e/models/one_D.py#L214`

Three heat transfer relations are passed:

- `Nu_func_tp`: The high-level two-phase heat transfer relation.
- `Nu_func_le`: The Nusselt number if the flow would be entirely liquid. Passed to `Nu_func_tp`.
- `Nu_func_dryout`: The Nusselt number in case of dry-out. assed to `Nu_func_tp`.

`Nu_func_tp` also gets passed arbitrary arguments, in addition to `Nu_func_le` and `Nu_func_dryout`. `Nu_func_tp` controls if and how the other two Nusselt relations are used.

The arbitrary functions are passed in the dictionary `Nusselt_relations` which is set in the design tool settings.

The same approach is used for pressure drop relations, and these are passed in the dictionary `pressure_drop_relations`.

B

Example verification case

For verification of the code of the basic model, no example calculation was found, so a basic case was constructed and calculated manually. The relevant equations in Chapter 3 were used, and the results are given below. For the thermodynamic data `https://webbook.nist.gov/chemistry/` was used (instead of CoolProp[30] in the code). Since the model is split up in a liquid/multi-phase part and a gas part, the intermediate results of both sections are compared as well.

The inputs are given in Table B.1. The results and important intermediate values are in Table B.2. The channel length is the final result and is within 1% of the manually calculated result. Upon inspection, the reason that the difference is not smaller is due to a difference in the viscosity provided by CoolProp and the Chemistry Webbook. This difference is explained by the more recently developed correlations which are implemented by CoolProp, which have slightly improved accuracy. This difference propagates itself from the calculation of the Prandtl number Pr, through the Nusselt number into the final result. Its impact (1.3%) is slightly attenuated through subsequent calculations.

Table B.1: Inputs for basic two-phase single-channel model

Parameter	**Value**
T_{in} [K]	300
T_c [K]	500
T_{w} [K]	600
p_{in} [bar]	5
$\dot{m}$ [mg· s^{-1}]	1
d_c [μm]	100
w_c [μm]	100
Nu relation	Dittus-Boelter for both phases(Eq. 3.50)
Propellant	Water

Table B.2: Comparison of manual calculation and results from basic single-channel two-phase model

Parameter		**Liquid/two-phase**		**Gas**		
		Expected	*Result*	*Expected*	*Result*	Δ_{max}
$\dot{Q}_f$	[W]	2.6351	2.6351	0.1646	0.1646	$< 0.1\%$
T_{bulk}	[K]	362.49	362.49	462.49	462.49	$< 0.1\%$
u_{bulk}	[ms^{-1}]	0.10353	0.10353	41.423	41.423	$< 0.1\%$
ρ_{bulk}	[kg$\cdot m^{-3}$]	965.93	965.93	2.4141	2.4141	$< 0.1\%$
Re_{bulk}	[-]	31.556	31.579	640.70	640.61	$< 0.1\%$
Pr_{bulk}	[-]	1.9730	1.9789	0.99236	1.0051	1.3%
Nu	[-]	0.4775	0.4783	4.0338	4.0541	$< 1\%$
St	[-]	0.00767	0.00766	0.0063444	0.0062961	$< 1\%$
h_{conv}	[Wm^{-2}K^{-1}]	3224.5	3218.3	1377.4	1366.7	$< 1\%$
A_{mh}	[μm^2]	3.4407	3.4474	0.86903	0.87573	$< 1\%$
l_c	[mm]	8.6018	8.6818	2.1726	2.1893	$< 1\%$
		Total				
		Expected		*Result*		
l_c	[mm]	10.773		10.808		$< 1\%$

C

Nozzle modelling based on IRT and Makhan (2018)

This chapter restates the equations used in the nozzle correction factors of Makhan, for the reference of the reader. The underlying equations from Ideal Rocket Theory (IRT) were already implemented, verified and validated during the literature study. All used equations in this chapter are sourced from Chapter 2 of “Performance of the MEMS Vaporizing Liquid Microthruster using cold nitrogen gas as propellant: An experimental study” by Makhan[20] unless stated otherwise.

C.1. Corrections

C.1.1. Reynolds number at the throat

The Reynold’s number Re is often a good flow characteristic to (empirically) predict the behaviour of real flows. It is important to be specific about the characteristic length used, to ensure everyone is using the same reference. In this model this length is the hydraulic diameter D_h, which is commonly used when the cross-section is not circular.

$$\mathrm{Re}_t = \frac{\rho_t u_t D_h}{\mu} = \frac{\dot{m} D_{h_t}}{\mu_t A_t} \tag{C.1}$$

$$D_{h_t} = \frac{4A_t}{P_t} \tag{C.2}$$

$$= \frac{4 w_{\text{throat}} d_c}{2(w_{\text{throat}} + d_c)} \qquad \text{for rectangular throat cross-sections} \tag{C.3}$$

C.1.2. Divergence loss

IRT assumes a quasi-1-dimensional nozzle flow, but in reality the gases are not expelled perfectly parallel to the nozzle axis, but have some radial element to their exit velocity. The divergence losses account for this and these were the used corrections:

$$C_{\text{div2D}} = \frac{\sin \alpha_{\text{divergent}}}{\alpha_{\text{divergent}}} \qquad \text{for 2D conical nozzles} \tag{C.4}$$

(C.5)

In this $\alpha_{\text{divergent}}$ is the half angle in radians of the nozzle. No range of validity is mentioned, and it is not unthinkable that rarefied flow does not follow the nozzle contour as much as continuous flow. This loss factor is then applied to the thrust coefficient, by multiplying it with the characteristic thrust coefficient C_F^0:

$$C_{F\,\text{div}} = C_{\text{div}} C_F^0 + \frac{p_e - p_a}{p_c} \frac{A_e}{A_t} \tag{C.6}$$

Alternatively, one can recognize that this divergence loss is applied to the momentum thrust only, and work with the thrust F directly:

$$F_{\text{div}} = C_{\text{div}}\dot{m}u_e + (p_e - p_a)A_e \tag{C.7}$$

C.1.3. Viscous loss

IRT does not account for viscous losses in the flow. Makhan uses the following equation to estimate the viscous losses, with reported validity for a nozzle area ratio of $25 < \frac{A_e}{A_t} < 150$, and throat Reynolds numbers of $2000 < \text{Re}_t < 10000$, but no accuracy was mentioned for this range. Another problem is that this correction is intended for 3D conical nozzles, and not 2D conical nozzles.

$$C_{\text{visc}} = \frac{17.6e^{0.0032\frac{A_e}{A_t}}}{\sqrt{\text{Re}_t}} \tag{C.8}$$

It is not clear whether Makhan corrected the initial Re_t for the actual nozzle wall temperature T_{w} for cold and hot flow, which according to Ernie W. Spisz are[41]:

$$\text{Re}_{t\,\text{wall}} = \text{Re}_t \frac{T^*}{T_{\text{w}}}^{\frac{5}{3}} \tag{C.9}$$

The argumentation by Ernie W. Spisz is that a more appropriate reference temperature must yield better results, and they found the nozzle wall temperature T_{w} to be an appropriate choice. This is interesting, because it means that a Vaporizing liquid micro-thruster Heating Chamber Model (VHCM) could help to estimate this wall temperature, by slightly extending the model towards the nozzle. However, for now, a correction factor will be applied based on their experimental data, namely:

$$\text{Re}_{t\,\text{wall, hot}} = \text{Re}_t 1.388^{\frac{5}{3}} \tag{C.10}$$

$$\text{Re}_{t\,\text{wall, cold}} = \text{Re}_t 0.857^{\frac{5}{3}} \tag{C.11}$$

C.1.4. Throat boundary loss

The throat boundary loss is also due to viscous effects. The formation of a boundary layer comes at the expense of momentum in the flow, and in addition, it reduces the effective throat area ratio[8]. These effects are captured in the discharge factor C_d. The equation used is:

$$C_{d\,\text{boundary loss}} = 1 - \left(\frac{\gamma+1}{2}\right)^{\frac{3}{4}} \left[\frac{72 - 32\sqrt{6}}{3(\gamma+1)} + \frac{4\sqrt{6}}{3}\right]\left(\frac{1}{\sqrt{\text{Re}_{\text{mod}}}}\right) + \left[\frac{2\sqrt{2}(\gamma-1)(\gamma+2)}{3\sqrt{\gamma+1}}\right]\left(\frac{1}{\text{Re}_{\text{mod}}}\right) \tag{C.12}$$

$$\text{Re}_{\text{mod}} \equiv \text{Re}_t \sqrt{\frac{R^*}{R_t}} \tag{C.13}$$

In this equation γ is the specific heat ratio, and Re_{mod} is the Reynolds number at the throat modified by the radius of curvature of the throat R^* and the throat radius R_t. According to Figure 2.13 in Makhan's work, the result is very sensitive to $\frac{R^*}{R_t}$[20].

D

Material and propellant properties

D.1. Silicon (wafers)

The transport properties of silicon depend heavily on temperature around the boiling temperature of water (300K), with thermal conductivity k_{si} dropping by a third from 300 to 400K, and halving from 300 to 500K[42]. Shanks et al. measured these properties in their 1963 paper on pure silicon properties:

T [K]	**k** [W/(mK)]
300	142.2
400	97.4
500	69.2
600	57.7
700	48.3
800	40.0
900	33.7
1000	29.8

Table D.1: Thermal conductivity of pure silicon (Reproduced Table III (truncated at 1000K) from H. R. Shanks et al. "Thermal Conductivity of Silicon from 300 to 1400°K". in: *Physical Review* 130.5 (June 1963), pp. 1743–1748. DOI: 10.1103/physrev.130.1743)

No statement was made about the purity of the samples.

Another source[43], also includes values over a larger range of temperatures, and used high-purity crystals instead of very lightly doped silicon. It states accuracies of about 5%. Glassbrenner and Slack are also more clear on what is considered high-purity. They state that the concentration of impurities(elements carrying charge through the silicon) was so low that it could not affect the thermal conductivity at all[43].

T [K]	**k** [W/(mK)]	**T** [K]	**k** [W/(mK)]
100	950	400	105
125	600	500	80
150	420	600	64
175	325	700	52
200	266	800	43
250	195	900	35.6
300	156	1000	31

Table D.2: Thermal conductivity of high-purity silicon (Reproduced truncated Table I from C. J. Glassbrenner and Glen A. Slack. "Thermal Conductivity of Silicon and Germanium from 3°K to the Melting Point". In: *Physical Review* 134.4A (May 1964), A1058–A1069. DOI: 10.1103/physrev.134.a1058)

The **density** of silicon at room temperature (25°C) is 2329.02 $kg \cdot m^{-3}$ with temperature variations being maximally 1% in the 300 to 1400K temperature range.[42]

The **emissivity** ε of silicon is dependent on the doping of the silicon, and the temperature.Timans studied this behaviour, with the following plot as a result[44]:

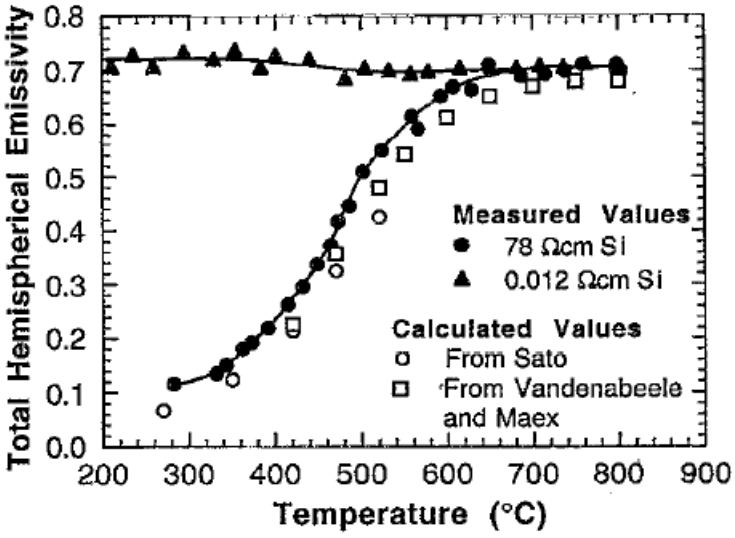

FIG. 15. The total hemispherical emissivity of the lightly (78 Ω cm) and heavily (0.012 Ω cm) doped silicon specimens as a function of temperature. The solid curves are fits to the data points. The open circles are values calculated from the data of Sato (see Ref. 14) and the open squares are values calculated using the data of Vandenabeele and Maex (see Ref. 12).

Figure D.1: Emissivity of silicon (Reproduced Figure 15 from the work of Timans[44])

D.2. Water properties

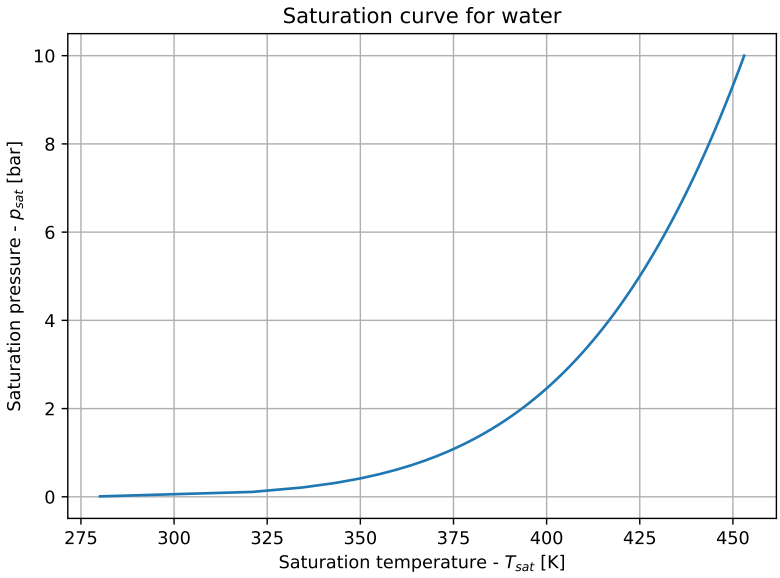

Figure D.2: Saturation curve of water

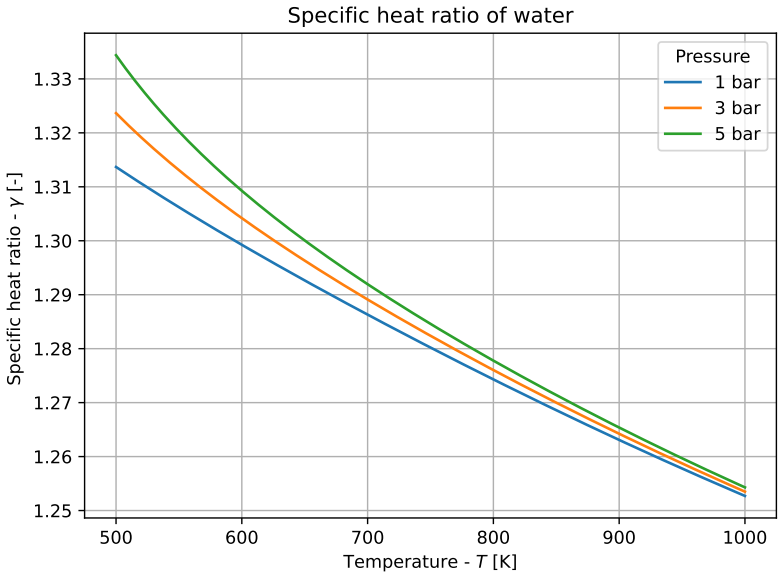

Figure D.3: Saturation curve of water

E

Additional figures

This appendix contains some additional figures, which may be of interest to the reader. They have been omitted from the main text as they did not clarify the matter at hand. However, they might be required for the reader for convenience or to check data that was taken from plots instead of tables.

E.1. Figures from Cen and Xu

Many values on thruster performance for validation purposes, were taken from plots in Cen and Xu. These plots are in Figure E.1. The design values taken from Cen and Xu were taken from Figure E.2. The originals can be found in their work, which is fully cited here: J.W. Cen and J.L. Xu. “Performance evaluation and flow visualization of a MEMS based vaporizing liquid micro-thruster”. In: *Acta Astronautica* 67.3-4 (Aug. 2010), pp. 468–482. DOI: 10.1016/j.actaastro.2010.04.009.

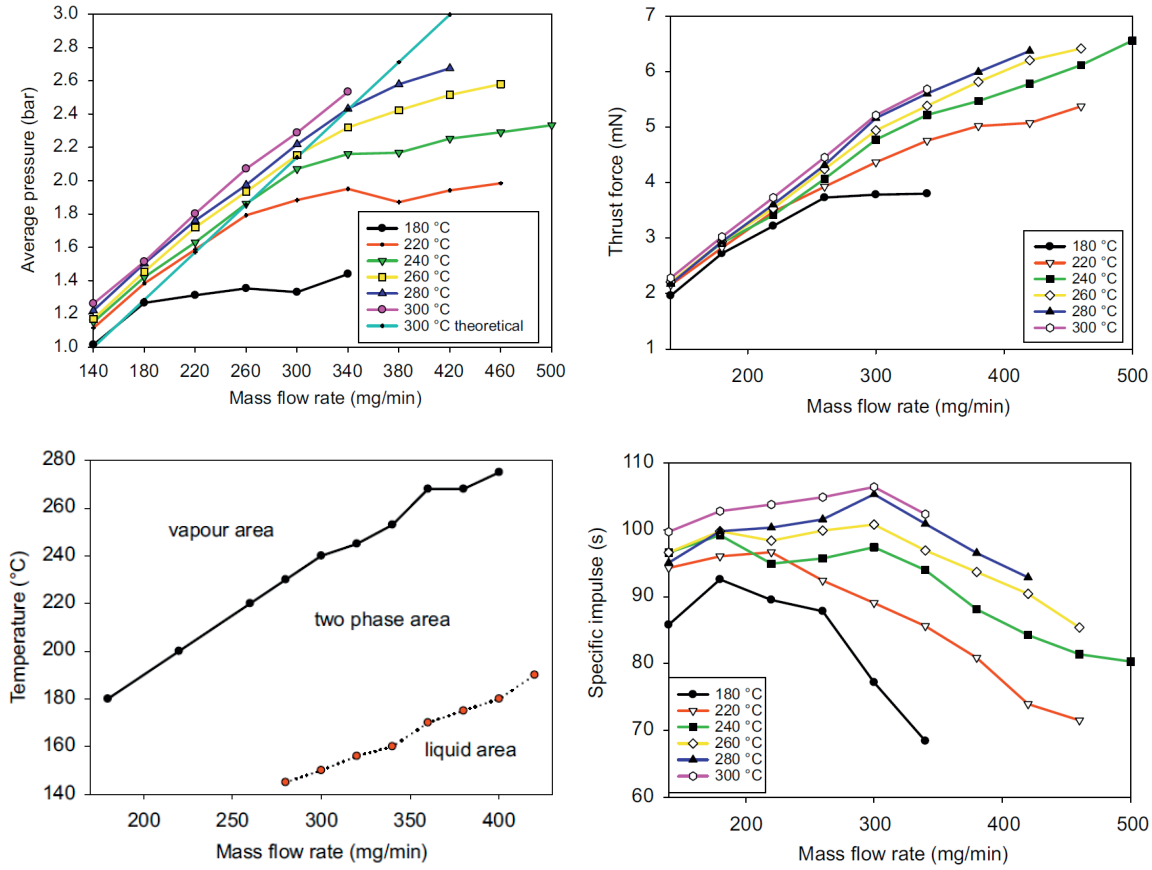

Figure E.1: Measurements from tests, reproduced from the work of Cen and Xu[13]

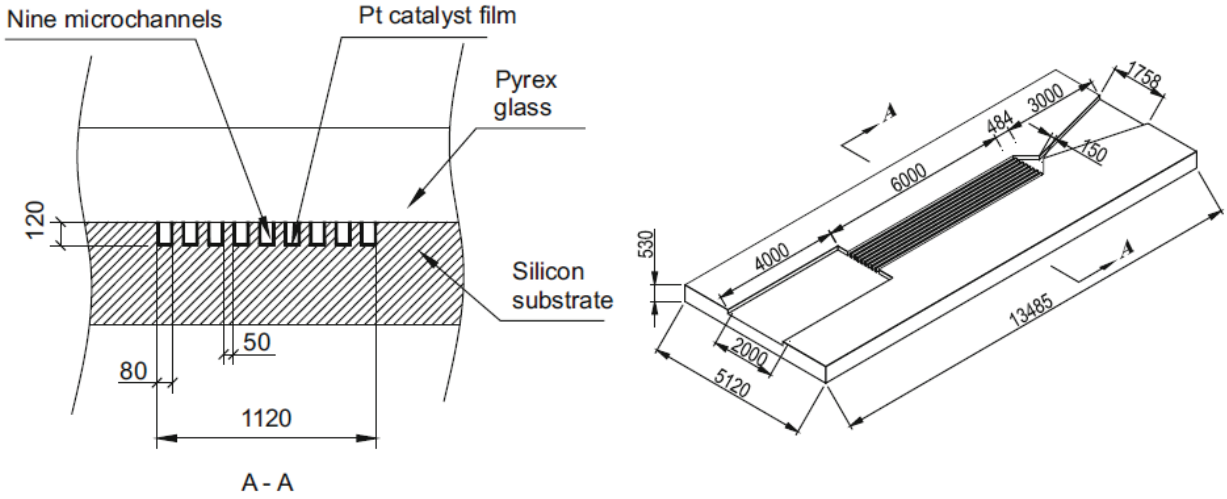

Figure E.2: Heating chamber design in micron, reproduced from the work of Cen and Xu[13]

E.2. Sensitivity analysis on nozzle divergent half-angle

As mentioned in the introduction of Chapter 5 the divergent half-angle of the nozzle was erroneously set to $\alpha_{\text{divergent}} = 22.5\,\text{deg}$ instead of the 30 degrees established in Table 2.5 of the design space. This angle was not particularly a topic of the study. It was set to 30 degrees to make the nozzle dimensions as close to what would be used in practice. The resulting geometry and the associated heat losses would therefore also be more realistic.

The effect of this mistake was expected to be so small, that it hardly justifies redoing all the work in the results chapter. Instead a sensitivity analysis was performed, to determine how the changed value would affect the heat losses. In Figure E.3 one can see that in the worst case for 5 mN the total power consumption is at most 0.47% lower. For 1 mN the total power consumption is at most 0.28% lower. This difference was caused by changes in the nozzle size, and not by changes in the heating chamber. Since it is the heating chamber that was the main topic of study, this difference is rather unimportant. The author thinks it is justified to analyse the results with the nozzle divergent half-angle $\alpha_{\text{divergent}}$ set to 22.5 degrees.

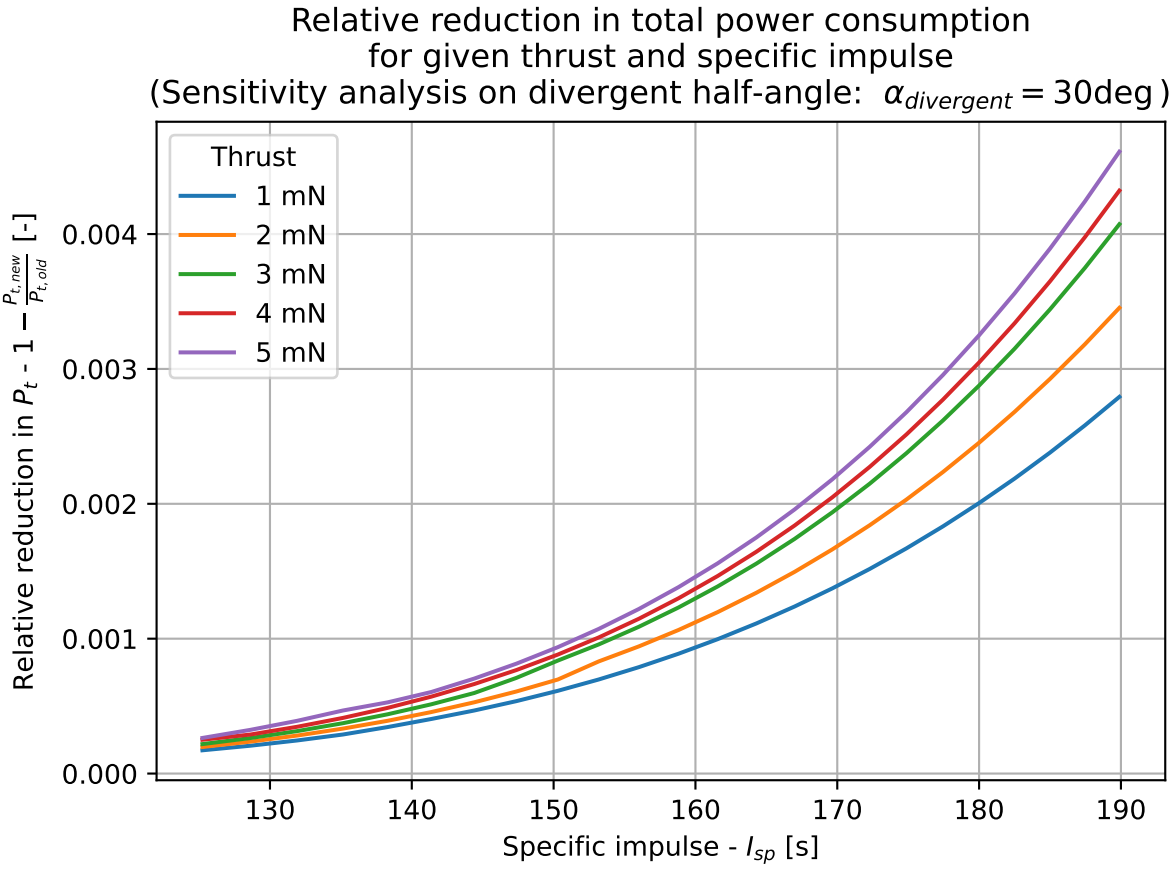

Figure E.3: Sensitivity analysis: $\alpha_{\text{divergent}} = 30\,\text{deg}$

Bibliography

[1] J. Bouwmeester and J. Guo. “Survey of worldwide pico- and nanosatellite missions, distributions and subsystem technology”. In: *Acta Astronautica* 67.7-8 (Oct. 2010), pp. 854–862. DOI: 10.1016/j.actaastro.2010.06.004.

[2] Kristina Lemmer. “Propulsion for CubeSats”. In: *Acta Astronautica* 134 (May 2017), pp. 231–243. DOI: 10.1016/j.actaastro.2017.01.048.

[3] *Suppliers - Cubesat*. June 12, 2019. URL: https://web.archive.org/web/20190612092947/https://www.cubesat.org/new-index.

[4] Alba Orbital, TU Delft & GAUSS. *The PocketQube Standard*. June 7, 2018. URL: https://dataverse.nl/api/access/datafile/11680.

[5] TU Delft. *”Delfi-PQ”*. Sept. 26, 2019. URL: http://web.archive.org/web/20190926110711/https://www.tudelft.nl/lr/subsites/delfi-space/delfi-pq/.

[6] Andrew D. Ketsdever and Michael M. Micci, eds. *Micropropulsion for Small Spacecraft*. American Institute of Aeronautics and Astronautics, Jan. 2000. DOI: 10.2514/4.866586.

[7] Marsil A.C. Silva et al. “A review of MEMS micropropulsion technologies for CubeSats and PocketQubes”. In: *Acta Astronautica* 143 (Feb. 2018), pp. 234–243. DOI: 10.1016/j.actaastro.2017.11.049.

[8] B.T.C. Zandbergen. *Thermal Rocket Propulsion (version 2.05)*. 2016.

[9] Donald J. Kessler and Burton G. Cour-Palais. “Collision frequency of artificial satellites: The creation of a debris belt”. In: *Journal of Geophysical Research* 83.A6 (1978), p. 2637. DOI: 10.1029/ja083ia06p02637.

[10] A. Cervone et al. “Green micro-resistojet research at Delft University of Technology: new options for Cubesat propulsion”. In: *CEAS Space Journal* 9.1 (July 2016), pp. 111–125. DOI: 10.1007/s12567-016-0135-3.

[11] Marsil A.C. Silva et al. “Vaporizing Liquid Microthrusters with integrated heaters and temperature measurement”. In: *Sensors and Actuators A: Physical* 265 (Oct. 2017), pp. 261–274. DOI: 10.1016/j.sna.2017.07.032.

[12] Juergen Mueller; Richard Hofer; John Ziemer. *Survey of propulsion technologies applicable to cubesats*. Tech. rep. Pasadena, CA : Jet Propulsion Laboratory, National Aeronautics and Space Administration, 2010. URL: http://hdl.handle.net/2014/41627.

[13] J.W. Cen and J.L. Xu. “Performance evaluation and flow visualization of a MEMS based vaporizing liquid micro-thruster”. In: *Acta Astronautica* 67.3-4 (Aug. 2010), pp. 468–482. DOI: 10.1016/j.actaastro.2010.04.009.

[14] K. Karthikeyan et al. “Low temperature co-fired ceramic vaporizing liquid microthruster for microspacecraft applications”. In: *Applied Energy* 97 (Sept. 2012), pp. 577–583. DOI: 10.1016/j.apenergy.2011.11.078.

[15] George Sutton. *Rocket propulsion elements*. New York: John Wiley & Sons, 2001. ISBN: 0471326429.

[16] John D. Anderson. *Fundamentals of Aerodynamics*. McGraw Hill Higher Education, 2006. ISBN: 0071254080. URL: https://www.amazon.com/Fundamentals-Aerodynamics-John-D-Anderson/dp/0071254080?SubscriptionId=AKIAIOBINVZYXZQZ2U3A&tag=chimbori05-20&linkCode=xm2&camp=2025&creative=165953&creativeASIN=0071254080.

[17] M. A. C. Silva et al. “Topology optimization of heating chamber of vaporizing liquid microthrusters”. In: 2018.

[18] Jorgis Theodoulou. “VLM Heating Chamber Design and Modelling: Literature Research”.

[19] C.A.J. Hanselaar. “Evaporative Two-Phase Micro-Flow Modelling”. MA thesis. Delft University of Technology, 2016.

[20] Rajeev Makhan. “Performance of the MEMS Vaporizing Liquid Microthruster using cold nitrogen gas as propellant: An experimental study”. MA thesis. Delft University of Technology, Dec. 13, 2018.

[21] Huib Versteeg. “Novel fabrication method for a hot gas supersonic micro-thruster”. MA thesis. TU Delft Aerospace Engineering, 2020. URL: http://resolver.tudelft.nl/uuid:ac2482ad-0f8e-4569-8bd4-fd11bd6327bd.

[22] Angelos Karagiannis. “Numerical Examination of Non-Equilibrium Condensation in Supersonic Micronozzles”. MA thesis. TU Delft Aerospace Engineering, 2020. URL: http://resolver.tudelft.nl/uuid:abe34357-627e-4df4-92eb-73e590ab79a6.

[23] William F. Louisos and Darren L. Hitt. “Viscous Effects on Performance of Two-Dimensional Supersonic Linear Micronozzles”. In: *Journal of Spacecraft and Rockets* 45.4 (July 2008), pp. 706–715. DOI: 10.2514/1.33434.

[24] W. F. Louisos and D. L. Hitt. “Viscous Effects on Performance of Three-Dimensional Supersonic Micronozzles”. In: *Journal of Spacecraft and Rockets* 49.1 (Jan. 2012), pp. 51–58. DOI: 10.2514/1.53026.

[25] Josu Barredo et al. “On the mechanical strength of monocrystalline, multicrystalline and quasi-monocrystalline silicon wafers: a four-line bending test study”. In: *Progress in Photovoltaics: Research and Applications* 22.12 (Apr. 2013), pp. 1204–1212. DOI: 10.1002/pip.2372.

[26] Lian Zhang et al. “Measurements and modeling of two-phase flow in microchannels with nearly constant heat flux boundary conditions”. In: *Journal of Microelectromechanical Systems* 11.1 (2002), pp. 12–19. DOI: 10.1109/84.982858.

[27] Satish G. Kandlikar and Prabhu Balasubramanian. “An Extension of the Flow Boiling Correlation to Transition, Laminar, and Deep Laminar Flows in Minichannels and Microchannels”. In: *Heat Transfer Engineering* 25.3 (Apr. 2004), pp. 86–93. DOI: 10.1080/01457630490280425.

[28] Richard H. Byrd et al. “A Limited Memory Algorithm for Bound Constrained Optimization”. In: *SIAM Journal on Scientific Computing* 16.5 (Sept. 1995), pp. 1190–1208. DOI: 10.1137/0916069.

[29] V. P. Carey. *Liquid-vapor phase-change phenomena : an introduction to the thermophysics of vaporization and condensation processes in heat transfer equipment*. New York: Taylor and Francis, 2008. ISBN: 9781591690351.

[30] Ian H. Bell et al. “Pure and Pseudo-pure Fluid Thermophysical Property Evaluation and the Open-Source Thermophysical Property Library CoolProp”. In: *Industrial & Engineering Chemistry Research* 53.6 (2014), pp. 2498–2508. DOI: 10.1021/ie4033999. eprint: http://pubs.acs.org/doi/pdf/10.1021/ie4033999.

[31] Satish G. Kandlikar. “History, Advances, and Challenges in Liquid Flow and Flow Boiling Heat Transfer in Microchannels: A Critical Review”. In: *Journal of Heat Transfer* 134.3 (2012), p. 034001. DOI: 10.1115/1.4005126.

[32] Adrian Bejan. *Convection Heat Transfer*. John Wiley & Sons, Mar. 28, 2013. 704 pp. URL: https://www.ebook.de/de/product/21164239/adrian_bejan_convection_heat_transfer.html.

[33] Satish Kandlikar and Prabhu Balasubramanian. “Extending the Applicability of the Flow Boiling Correlation to Low Reynolds Number Flows in Microchannels”. In: *1st International Conference on Microchannels and Minichannels*. ASMEDC, Jan. 2003. DOI: 10.1115/icmm2003-1075.

[34] William Boyce. *Elementary differential equations*. New York: Wiley, 2003. ISBN: 9780471678885.

[35] C. P. Kothandaraman. *Fundamentals of heat and mass transfer*. New Delhi: New Age International (P) Ltd., Publishers, 2006. ISBN: 9788122417722.

[36] Gherhardt Ribatski, Leszek Wojtan, and John R. Thome. “An analysis of experimental data and prediction methods for two-phase frictional pressure drop and flow boiling heat transfer in micro-scale channels”. In: *Experimental Thermal and Fluid Science* 31.1 (Oct. 2006), pp. 1–19. DOI: 10.1016/j.expthermflusci.2006.01.006.

[37] H Müller-Steinhagen and K Heck. “A simple friction pressure drop correlation for two-phase flow in pipes”. In: *Chemical Engineering and Processing: Process Intensification* 20.6 (Nov. 1986), pp. 297–308. DOI: 10.1016/0255-2701(86)80008-3.

[38] Akimaro Kawahara et al. “Characteristics of gas–liquid two-phase flows through a sudden contraction in rectangular microchannels”. In: *Experimental Thermal and Fluid Science* 66 (Sept. 2015), pp. 243–253. DOI: 10.1016/j.expthermflusci.2015.03.030.

[39] John Wesley Coleman. “An Experimentally Validated Model for Two-Phase Sudden Contraction Pressure Drop in Microchannel Tube Headers”. In: *Heat Transfer Engineering* 25.3 (Apr. 2004), pp. 69–77. DOI: 10.1080/01457630490280335.

[40] Liangbin Su et al. “Heat transfer characteristics of thermally developing flow in rectangular microchannels with constant wall temperature”. In: *International Journal of Thermal Sciences* 155 (Sept. 2020), p. 106412. DOI: 10.1016/j.ijthermalsci.2020.106412.

[41] John R. Jack Ernie W. Spisz Paul F. Brinich. *Thrust Coefficients of Low-Thrust Nozzles*. Tech. rep. NASA, Lewis Research Center, Oct. 1965.

[42] H. R. Shanks et al. “Thermal Conductivity of Silicon from 300 to 1400°K”. In: *Physical Review* 130.5 (June 1963), pp. 1743–1748. DOI: 10.1103/physrev.130.1743.

[43] C. J. Glassbrenner and Glen A. Slack. “Thermal Conductivity of Silicon and Germanium from 3°K to the Melting Point”. In: *Physical Review* 134.4A (May 1964), A1058–A1069. DOI: 10.1103/physrev.134.a1058.

[44] P. J. Timans. “Emissivity of silicon at elevated temperatures”. In: *Journal of Applied Physics* 74.10 (Nov. 1993), pp. 6353–6364. DOI: 10.1063/1.355159.